Dissertation
submitted to the
Combined Faculties of the Natural Sciences and Mathematics
of the Ruperto-Carola-University of Heidelberg. Germany
for the degree of
Doctor of Natural Sciences

Put forward by
Mykola G. Malygin
born in Cherkasy (Ukraine)
Oral examination: 03.02.2016

Gas Opacity in Planet and Star Formation

Referees: PD. Dr. Hubert Klahr
Prof. Dr. Andreas Quirrenbach

# Gas Opacity in Planet and Star Formation

A dissertation presented

by

Mykola G. Malygin

to

The Department of Physics and Astronomy

in partial fulfillment of the requirements

for the degree of

Doctor of Philosophy

in the subject of

Astrophysics

Ruperto Carola Universität

Heidelberg, Baden-Würtemberg

February 2016

# Abstract

Die Gas Opazität in der Planeten- und Sternenenstehung Die Opazität von Gas und Staub spielt eine Schlüsselrolle bei der Bestimmung von Struktur und Strahlenspektrum von Staub-Gas-Wolken um Sterne (CSM), da hier Strahlentransport den Hauptübertragungsprozess für Energie darstellt. Das Vorherrschen von Staub in Kontinuumabsorbtion und die rechnerische Komplexität bei der Verwendung von molekularen Linienspektren hat bisher verhindert das letztere in den meisten Studien zur Planeten und Sternenentstehung Berücksichtigung fand. Diese Arbeit präsentiert die Berechnung von Gasopazitäten im entscheidenden Parameterraum, eine Methode um diese in Strahlungstransportberechnungen zu nutzen und erste Resultate von Strahlungstransport- und Temperaturausgleichsberechnungen.
Die größte Satz an staubfreien CSM-Opazitäten zeigt dank verbesserter Frequenzabtastung bis zu $10^4$ mal größere mittlere Planckopazitäten im Vergleich zu früheren Arbeiten. Mittlere Zweitemperaturplanckopazitäten sind für die Bestimmung vor allem in optisch dünnen angestrahlten Gasen wichtig. Die mittlere Temperatur, mit tabellarisierter Opazitäten bestimmt, in solchen Gasen ist degeneriert und von der Vergangenheit des Mediums abhängig. Das vorgestellte Verfahren zur Bestimmung von Temperaturausgleichszeiten berücksichtigt Stoßwechselwirkung, die den Ausgleich der Temperatur in Regionen mit wenig Gas beschränken. Eine grundsätzliche untere Schranke der Temperaturausgleichszeiten ist durch LTE-Emissionen gegeben. Die Geschwindigkeit des Temperaturausgleich beeinflusst wichtige hydrodynamische Instabilitäten die für Turbulenz in magnetisch inaktiven Zonen eine Rolle spielen.

Gas opacity in planet and star formation Opacity plays a key role in determining the structure of the heterogeneous circumstellar medium (CSM) and its observable spectrum. Planet and star formation changes dust density on various spatial and time scales through gravity and turbulence, radiation field and chemistry. The following thesis presents calculations of gas opacity in the suitable parameter space, a methodology of utilising it in hybrid-type radiative transfer schemes, as well as first results on radiative transfer and thermal relaxation calculations.
The largest set of dust-free opacity in the CSM regime is presented. Improved frequency sampling yielded substantially larger (up to a factor of $10^4$ in comparison to some previous works) Planck means. The two-temperature Planck means important for determining the temperatures in the optically thin irradiated gases were tabulated. The equilibrium temperature in such media is degenerate and depends on the thermal history of the gas.
The suggested recipe to estimate the thermal relaxation time accounts for collisional coupling, which limits the relaxation in low-density regions. A fundamental lower limit to the relaxation time is set by the LTE emissivity giving $\Omega t \sim 10^{-4}$ at the T Tau phase. The locations of onset of linear and the locations of operation of subcritical hydrodynamic instabilities, reckoned as turbulence drivers in magnetically inactive zones, are constrained by the relaxation criterion.

# Contents

To my two daughters and my wife.

*The secret of getting ahead is getting started.*

Mark Twain

# 0 Introduction

## 0.1 Gas Spectroscopy

William Hyde Wollaston was the first one to publish a notice of absorption features in dispersed light from the Sun as well as from candle fire, which he revealed during his foreshadowing experiments with prisms [Wollaston, 1802, p. 378]. Shortly afterwards, Joseph Fraunhofer duly noted 574 *"stärke und schwache vertikale Linien"* he observed in a diffracted solar light [Fraunhofer, 1817, p. 279]. A complementary information from later experiments held in Heidelberg by Gustav Robert Kirchhoff and Robert Wilhelm Bunsen on candle light spectrum [Kirchhoff & Bunsen, 1860], established a new field in physics: *spectroscopy*. Balmer identified a series of spectral lines from Hydrogen [Balmer, 1885]. Hydrogen and Helium absorption lines in solar spectrum [Lockyer, 1869, pp.432-434] as well as both absorption and emission lines from other objects [Pickering et al., 1901; Pickering, 1901d,c] and other phenomena [Pickering, 1901b]. Observations of absorption lines in binary stars ["spectroscopic binaries" Pickering, 1901a] enabled mass estimate and the radial velocity measurements, now in heart of the main ground-based exoplanet search method. It was not until 1913, when Bohr made a genuine intuitive step that founded quantum mechanics [Bohr, 1913a,b,c]*. Spectroscopy became a revolutionary technique in astrophysics. Spectra turned to be 'biometric'

*The story tells that Bohr's interpretation was anticipated by three years in a 1910 work by an Austrian physicist Arthur Erich Haas, but the publication got rejected.

databases of stellar properties allowing deciphering such information as effective, kinetic and excitation temperatures, gravitational attraction in photospheres, abundances of various species, microturbulent (non-thermal) motions, rotational velocities, magnetic field strengths, and many more. Spectroscopic binaries not only allow testing fundamental physical assumptions (no overtake of light by light in vacuum), but pinned down the presence of interstellar medium [Hartmann, 1904, p.273]. Observing the ISM in different molecular lines reveals the kinematics of inherent gaseous structures, yet scanning their morphology to different depths, probing physics at different spatial scales. The Doppler effect erected a concept of red shift when the first optical spectrum of a quasar was measured [Schmidt, 1963].

Yet in the context of present day star formation and planet formation gas opacity is almost invariably neglected in favour of dust continuum opacity or at best prescribed with a stunning degree of simplicity. However, gas opacity without a dust continuum contribution have many applications: not only in atmospheric studies[Freedman et al., 2008] but for dust formation itself [e.g. Helling et al., 2000; Helling & Lucas, 2009]. It will manifest its dominance in a dust-depleted medium resulting either from a low-metallicity environment or when the equilibrium temperature gets higher than the local dust sublimation temperature.

## 0.2 Context & Motivation

Gas opacity with metals contribution has to be taken into account when describing inner regions of accretion disks [Muzerolle et al., 2004; Vaidya et al., 2009; Zhang & Tan, 2011], cooling of non-accreting hot stellar remnants [e.g. Rohrmann et al., 2012], dust formation around pulsating AGB stars [Schirrmacher et al., 2003], calculating energy balance of Type Ia supernovae [e.g. Dessart et al., 2014], i.e. in environments depleted in dust through some, usually radiative, processes. This research attacks the issue of gas opacity from two sides: the absorption of stellar irradiation and the thermal relaxation of the circumstellar gas by radiative energy transport. The first is relevant primarily in massive star formation and the radiative feedback processes. The second is important for physics of accretion discs and particularly in planet formation. Numerical modelling of both requires following dynamics of the fluid (gas and dust) along with evolution of the radiation field. The computational challenge of incorporating radiative transfer into dynamical modelling as well as the uncertainties in opacities and their secular change precluded accurate treatment of energy evolution in modelling of accretion disc, which instead has often been parametrised. The growth-time of the fastest-growing disturbances in accretion discs typically scales as $\Omega^{-1}$. Thus, it is convenient to express the thermal relaxation time in terms of a dimensionless number $\beta = \Omega t$. The estimates of the radiative cooling time from numerical modelling by Johnson & Gammie [2003]; Boley et al. [2006] show that such parametrisation is not suitable for global runs. Elaborate analytic

calculations [Nero & Bjorkman, 2009] confirm this result. A computationally efficient reliable recipe is required for global modelling.
Before doing 3D hydrodynamic simulations including full radiative transport, a reliable way to obtain realistic cooling times is required in its dependence on disk mass, temperature profile, dust-to-gas mass ratio, etc. The determination of effective thermal relaxation is needed for both the set-up of numerical experiments as well as for their physical interpretation. In this work, I present a recipe to calculate radiative relaxation rates of different Fourier modes and apply this to constrain places of inception of the gravitational and the hydrodynamic instabilities from given equilibrium structures.

### 0.2.1 Radiative Feedback from Star Formation

Gas opacity plays a crucial role in stellar physics underlying the mass-luminosity relation (the Hertzsprung-Russel diagram), but it is also relevant for processes of stellar feedback in the circumstellar medium (CSM). There is evidence that the inner gaseous parts of disks around Herbig stars are optically thick [Isella et al., 2006]; the same can be true for accretion disks around forming stars of higher masses [Zhang & Tan, 2011; Tanaka & Nakamoto, 2011; Kuiper & Yorke, 2013]. Although on molecular-cloud scales dust opacity dominates over gas opacity, the various embedded dust-free regions play a vital role in the stellar feedback processes that are essential for shaping and developing the ISM and which are important for linking stellar and cosmological scales [Pelupessy & Papadopoulos, 2009]. Last but not least, emission from molecular species in the gas phase are important probes of the gas properties and the kinematics of star-forming regions. The high angular-resolution observations with the Atacama Large Millimeter Array [Johnston et al., 2015] and SPHERE/VLT are now pushing the field of numerical modelling to resolve the circumstellar gaseous interiors and to properly treat gas opacity there.
A typical situation in a circumstellar environment is that a colder gas is irradiated by a hotter source: $T_{\rm gas} < T_{\rm rad}$. In this case, the absorption from the gas as expressed in terms of the Planck mean opacity will depend on a) the gas temperature determining its chemical state and the level populations and b) the radiation temperature defining the energy distribution of the ambient radiation field via the Planck function: $\varkappa_{\rm P} = \varkappa_{\rm P}\left(T_{\rm gas}, \varrho, T_{\rm rad}\right)$, a two-temperature Planck mean hereafter. This mean is essential for the equilibrium temperature determination in an optically thin gas (see 2). When the radiation temperatures are much higher than those of the gas (e.g., an irradiation of the cold molecular gas by a nearby O star), the abundant UV photons can rule non-equilibrium photochemistry through processes occurring on times shorter than the equilibration times. In this case, the calculations relying on simple equilibrium chemistry are unreliable. There exist opposite cases. Shocks, for example, can lead to situations when $T_{\rm gas} > T_{\rm rad}$. Such two-temperature Planck means are important in accretion discs. If $T_{\rm rad} = T_{\rm gas}$, it turns into

the common single-temperature Planck mean $\varkappa_{\mathrm{P}}\left(T_{\mathrm{gas}}, \varrho\right)$. The Rosseland mean $\varkappa_{\mathrm{R}}\left(T_{\mathrm{gas}}, \varrho\right)$ is introduced to provide radiation transport in an optically thick medium, where $T_{\mathrm{rad}} = T_{\mathrm{gas}}$. I will use the following designations: $\varkappa_{\mathrm{P}}\left(T_{\mathrm{gas}}, \varrho, T_{\mathrm{rad}}\right) = \varkappa_{\mathrm{P}}\left(T_{\mathrm{gas}}, T_{\mathrm{rad}}\right)$ for the two-temperature Planck mean, $\varkappa_{\mathrm{P}}\left(T_{\mathrm{gas}}, \varrho\right) = \varkappa_{\mathrm{P}}\left(T_{\mathrm{gas}}\right)$ for the Planck mean, and $\varkappa_{\mathrm{R}}\left(T_{\mathrm{gas}}, \varrho\right) = \varkappa_{\mathrm{R}}\left(T_{\mathrm{gas}}\right)$ for the Rosseland mean.

### 0.2.2 Accretion Discs

Accretion discs are abundant in diverse astrophysical contexts, that is at different scales. Kinematic probes with water maser emission suggest discs around active galactic nuclei [AGNs, Lodato & Bertin, 2003; Kondratko et al., 2005] and together with thermal lines – around high-mass young stellar objects [Cesaroni, 2002]. Rotational transitions of asymmetric molecules at mm wavelengths show complex kinematics of embedded Class 0/I objects [Tobin et al., 2011, 2012], still near-Keplerian rotation is captured [Simon et al., 2000; Brinch & Jørgensen, 2013]. The spectroimaging Atacama Large Millimeter Array (ALMA) observations are expanding the kinematic evidence for discs [e.g. Lindberg et al., 2014] to the domain of high-mass forming stars [Johnston et al., 2015] as predicted by theoretical [Nakano, 1989] and numerical [Bate, 1998; Kuiper et al., 2010a, 2011] works. Particularly, the unprecendent-resolution imaging in dust continuum mm emission captures axisymmetric structures in Class I objects [ALMA Partnership et al., 2015] and variety of asymmetric patterns in transitional discs [van der Marel et al., 2013; Isella et al., 2013; Pérez et al., 2014; Cieza, 2015, and references therein]. Interferometric imaging in near infrared is accessible for embedded discs around forming stars of different masses [Beltrán et al., 2004; Chini et al., 2004; Lin et al., 2006], the field is being currently pushed by SPHERE/VLT [Lagrange et al., 2015]. Low-resolution spectroscopy indicates accretion discs around brown dwarfs [Luhman et al., 2005; Joergens et al., 2013]. Further, accretion powers X-ray binaries and novae, serves a trigger for supernovae [e.g. Shapiro & Teukolsky, 1983; Callanan, 1993; Perets & Kenyon, 2013]. The major mode of planet formation takes place in circumstellar accretion discs [Beuther et al., 2014, chapters by Johansen et al., Raymond et al. and Chabrier et al.]. Despite this ample observational manifestation, accretion discs still puzzle astrophysicists. Two central open questions in physics of accretion discs – the problem of transport and the planet formation mechanism – are both related with the ability of the matter to liberate its internal energy. An importance of this thermal relaxation can be established through the characteristic relaxation time. Following sections show that the thermal relaxation time is important in angular momentum transport, disc fragmentation, planetesimal formation and migration of planets.

Radiative energy transport is the prior means of the thermal relaxation in circumstellar environments, hence opacity determines the timescale of the process. It is universally assumed that the dust is the main provider of low-temperature opacity in discs in spite of its minute mass fraction.

This general statement requires two precautions. First, which opacity is being talked about: the Rosseland opacity is indeed dominated by dust continuum under such conditions. However, the Planck means of the dust and the gas can still compare. Second, the dust amount: local dust density depletion can yield a relieve of the thermal energy on timescales shorter than the dust sublimation time. Indeed, dust evolution in a turbulent disc with an ongoing planetesimal formation changes dust density by a factor of $10 - 10^2$ [Birnstiel et al., 2012; Klahr & Lin, 2015]. Radiation from luminous young planetary cores undergoing accretion [Sallum et al., 2015] further contributes to photoevaporation of the grains. This alters thermal relaxation, which modifies the growth rates of hydrodynamic instabilities. Proper handling of relaxation in numerical modelling is ultimately required for synthesizing data compatible with the growing body of existing high-resolution observations [see Pohl et al., 2015, and references therein] as well as the future high-sensitivity infrared observations with the upcoming facilities like the James Webb Space Telescope.
In the following sections we discuss three aspects of PPD physics, in which radiative relaxation is important: (i) disc evolution and fragmentation driven by self-gravitation, (ii) particles accumulation by hydrodynamic instabilities, and (iii) planet-disc interactions and migration of protoplanetary cores.

#### 0.2.2.1 Transport in Accretion Discs

The operation of the dissipative mechanism redistributing the angular momentum and allowing accretion remains uncertain [Turner et al., 2014]. Various numerical studies on accretion discs identified possible sources of motions driving an effective, "turbulent" stress (see below). Central to all those are dynamical instabilities developing in rotating shear flows. The magneto-rotational instability [MRI, Balbus & Hawley, 1991, 1998] is driven by a weak yet well coupled magnetic field in a shearing flow and is not sensitive to thermal relaxation. Considerable part of the parameter space fitting protoplanetary discs (PPDs) inhibits the start of the MRI due to low ionization rates [Gammie, 1996]. It is where hydrodynamic or gravitational disturbances can produce the turbulent stress. Both the induced small-scale motions [Brauer et al., 2008; Zsom et al., 2010] and the gas drag in local density enhancements [Haghighipour & Boss, 2003b,a] can affect the dust grain growth and influence the orbital migration of protoplanets [Nelson & Papaloizou, 2004]. The onset and linear growth of non-magnetic perturbations depend crucially on thermal relaxation. This is quantifiable in terms of thermal relaxation time (Ch. 4).

#### 0.2.2.2 Gravitational Instability

In Planet Formation Self-fragmentation of a proto-planetary disc was historically the first suggestion for a mechanism of the solar planetary system formation, dating back to 18th century.

Lines of evidence from both observations and early theoretical work on turbulence drawn together by Kuiper [1951] established an admissible ground for this framework [Urey, 1966; Cameron, 1978]. Advance in radial velocity measurements yielded discoveries of giant extrasolar planets [Mayor & Queloz, 1995; Marcy & Butler, 1996; Butler & Marcy, 1996; Butler et al., 1997; Cochran et al., 1997] revitalising the theoretical interest in gravitational instability (GI) as a fast channel for gas giants formation Boss [1997, 1998, 2000, 2001, 2003, 2004]; Mayer et al. [2002, 2004]. High-sensitivity optical and infrared imaging [Kalas et al., 2008; Marois et al., 2008; Rameau et al., 2013] start to populate the parameter domain, shaded by radial velocity bias, with Jovian planets at large orbital separations. This parameter domain is the one favouring the GI to the core accretion. Next studies by Haghighipour & Boss [2003b,a]; Rice et al. [2004]; Pickett & Lim [2004]; Durisen et al. [2005, 2007] found that the GI can aid planetesimal formation through concentrating solids by the gas drag.

GI & Transport In magnetically inactive regions of accretion discs [Gammie, 1996; Armitage et al., 2001], non-axisymmetric gravitational disturbances can be predominant source of angular momentum and mass transport as pointed out by many [Lynden-Bell & Kalnajs, 1972; Larson, 1984; Boss, 1984; Durisen et al., 1986; Lin & Pringle, 1987; Papaloizou & Savonije, 1991; Laughlin & Bodenheimer, 1994]. This gravitoturbulence is especially expected at early stages of disc assemble, when the disc-to-stellar mass ratio is larger [see Lodato & Rice, 2004, 2005]; or at the quasi-static first core phase during a molecular cloud collapse [Bate, 1998], provided sufficiently fast rotation.

Thermal Relaxation in GI Analytic studies by Goldreich & Lynden-Bell [1965]; Cassen & Woolum [1996]; Rafikov [2005, 2009], though restricted to estimating spatially averaged radiative losses, emphasized the decisive role of thermal dynamics for both the inception and the non-linear phase of the GI. Still, reliable treatment of radiative relaxation in simulations is currently not implemented. Pioneering numerical works assumed infinitely fast relaxation, $t_{\rm relax} = 0$, to some predefined thermal states [Larson, 1969; Tohline et al., 1985; Ruden & Pollack, 1991; Adams & Benz, 1992; Nakamoto & Nakagawa, 1994; Pickett et al., 1996, 1998]. Later studies included the energy evolution but with simplistic opacities and/or a simplistic cooling law [Nelson et al., 2000; Pickett et al., 2000, 2003; Rice et al., 2003; Mejía et al., 2003, 2005; Boley et al., 2006]. In N-body simulations for stellar discs, Tomley et al. [1991, 1994] introduced the now widely used cooling formalism: a specified fraction of the thermal energy escapes per orbital period:

$$t_{\rm cool} = \beta \Omega^{-1} \tag{1}$$

By a local shear analytic argument, Gammie [2001] showed that a steady, saturated state of the GI is equivalent to having a local cooling time

$$\Omega t = [\alpha\,(9/4)\,\gamma\,(\gamma-1)]^{-1} = \beta = \text{const} \tag{2}$$

Here, $\alpha$ is a dimensionless measure of an effective local stress [Shakura & Sunyaev, 1973], $\gamma$ the ratio of specific heats, and $\Omega$ the local angular frequency. Equation (2) promotes interpreting the critical cooling time as the maximum local gravitational stress sustainable by the disc [Rice et al., 2005]. In this way, the cooling time is one of the parameters globally managing the evolution of gravitoturbulent accretion discs [Rafikov, 2015]. The locality of the GI has been numerically confirmed for low-mass, $q = \mathcal{M}_\mathrm{d}/\mathcal{M}_* \leqslant 0.25$, compact (aspect ratio $\leq 1$) discs with cooling being parametrised by Eq. 1 [Lodato & Rice, 2004; Cossins et al., 2009]. In Lodato & Rice [2005], intermediate mass discs with $q = 0.5$ endured fast (one outer rotational period) episode of accretion due to a transient, large-scale spiral structure disappearing before the disc's settling into an equilibrium state [Forgan et al., 2011]. Massive discs with $q \geqslant 1$ have been observed to undergo recurrent bursts of accretion driven by low azimuthal wavenumber (global wave transport) without settling into a steady-state [Lodato & Rice, 2005; Forgan et al., 2011] in line with Balbus & Papaloizou [1999].

Critical Cooling Time Problem Local, shearing-sheet numerical experiments on fragmentation of a turbulent PPD by Gammie [2001]; Johnson & Gammie [2003] revealed a critical lower value for the relaxation time parametrised with 2 as a complementary fragmentation requisite to the Toomre $Q$-criterion [Toomre, 1964] for a column density $\Sigma$ with the in-plane velocity dispersion $c_\mathrm{s}$

$$Q \leqslant Q_\mathrm{c} = \frac{c_\mathrm{s}\kappa}{\pi G\Sigma} \approx 1.5 \tag{3}$$

Here the epicyclic frequency $\kappa = \Omega + \mathcal{O}\,(d\ln\Omega/d\ln R + 3/2)$ is the frequency of linear radial oscillations. Two consequences follow from this result. First: a Toomre-unstable disc endures runaway fragmentation if the relaxation time is shorter than several dynamical times. Second: given sufficiently long relaxation time $\Omega t \geqslant \beta_\mathrm{crit} = 3$, the represented local patch of the disc is able to maintain a steady-state $Q \geqslant 1$ at least for the time the simulation was run (up to $10^3 \times \Omega^{-1}$ with $\beta = 10$). The first statement is robust: global 3D modelling with smoothed particle hydrodynamics (SPH) by Rice et al. [2003] captured the local instability for $\Omega t_\mathrm{cool} = 3$. The second statement has been refined in subsequent studies by widening the parameter space (disc masses, higher resolutions, longer runs) and using different numerical schemes (grid-based, SPH) in both local and global modelling [Rice et al., 2005; Meru & Bate, 2011b,a, 2012; Paardekooper et al., 2011]. The global runs with higher disc masses (with stronger non-local effects, see above) prompted an increase of the

critical relaxation time still furnished by local prescription (2). Additionally to this consistency issue, the role of artificial viscosity was not entirely settled. Meru & Bate [2012] reported evidence of convergence of the critical cooling time with increasing resolution in SPH and FARGO (fast rotating gaseous objects) viscosity schemes. However, a recent high-resolution numerical study by Baehr & Klahr [2015] with high-order finite difference scheme† shows no such evidence. The apparent non-convergence of the "critical cooling time" can be a ramification of stochastic nature of turbulence [Paardekooper, 2012; Hopkins & Christiansen, 2013, see Sect. 3.6.3 for more details]. Progressively smaller spatial scales resolved (yet being far from the Kolmogorov scale) pick up more of the turbulent cascade increasing the probability of the "in-phase" random fluctuation yielding bound condensation. Still, it is justified to speak of the critical relaxation time in the context of finite duration of gravitoturbulence.

#### 0.2.2.3 Core accretion

A chief paradigm in current planet formation theory is core accretion [CA, Perri & Cameron, 1974; Mizuno, 1980; Lissauer, 1993; Papaloizou & Terquem, 2006]. For a comprehensive review, we refer the reader to the books by Klahr & Brandner [2006] and Beuther et al. [2014] (see chapter by Johansen et al.). The CA implies persistent dust particles growth in PPDs after an initial sedimentation-driven coagulation [Safronov, 1969; Beckwith et al., 2000]. Follow-up accretion of solids and gas onto sufficiently massive cores [Mizuno et al., 1978; Pollack et al., 1996; Inaba et al., 2003] can yield gaseous giants. The physical picture faced three main challenges making a planetesimal formation highly unlikely a process operating on time scales longer than the lifetime of the disc. The bouncing and the shattering barriers [Blum & Münch, 1993; Zsom et al., 2010] as well as the radial drift barrier [Weidenschilling, 1977] all hinder the particle growth into planetesimals (held by self-gravity). An advance over the past decade in both numerical [Johansen et al., 2008] and laboratory [Wurm et al., 2005; Güttler et al., 2010] experiments on grain collisions along with numerical studies on the impact of porosity [Wada et al., 2008, 2009; Seizinger & Kley, 2013; Meru et al., 2013] has paved a track to circumventing these barriers in grain growth astrophysics [see, however, Krijt et al., 2015]. The solution to the problem can lie in the turbulent dynamics of the hosting environment – the gas. Retainment of the dust grains with suitable for growth relative velocities can be facilitated by turbulent eddies [Cuzzi et al., 1993; Klahr & Henning, 1997], streaming instabilities [Goodman & Pindor, 2000; Youdin & Goodman, 2005; Johansen et al., 2011], or pressure bumps stemming, e.g., from anticyclonic vortices [Barge & Sommeria, 1995; Johansen et al., 2004; Klahr, 2003; Klahr & Bodenheimer, 2006; Lyra et al., 2008, 2009], or zonal flows [the magnetorotational turbulence, Johansen et al., 2006, 2009; Dittrich et al., 2013]. There are three

†PENCIL, `http://pencil-code.nordita.org/`

identified sources of turbulent motions of purely hydrodynamic nature that can operate in magnetically inactive regions of a disc: the convective overstability [COV, Klahr & Hubbard, 2014; Lyra, 2014], the vertical shear instability[‡] [VSI Urpin & Brandenburg, 1998; Urpin, 2003; Nelson et al., 2013; Barker & Latter, 2015; Lin & Youdin, 2015] and the zombie vortex instability [ZVI, Marcus et al., 2013, 2015]. Each of those has the fastest growth rate for a specific relaxation regime: the VSI develops in isothermal environments (instant relaxation), the ZVI – in adiabatic (very slow relaxation) yet stably stratified discs, while the growth rate of the COV peaks at intermediate relaxation rates [Klahr & Hubbard, 2014]. The finite-amplitude noise seeded by the COV can trigger the subcritical baroclinic instability [SBI, Klahr & Bodenheimer, 2003; Lyra & Klahr, 2011; Lyra, 2014]. The evolution time scale of the resulting vortex is a non-monotonic function of thermal relaxation rate [Raettig et al., 2013, 2015; Lobo Gomes & Klahr, 2013; Lobo Gomes et al., 2015]. Thermal relaxation time constrains the onset locations of different modes of these instabilities (see Ch. 4).

#### 0.2.2.4 Core migration

Migration of protoplanetary cores – a secular change of their semi-major axis as due to the torques exerted from the ambient disc material – is another important process in planet formation. As an ingredient of the planet population synthesis [Mordasini et al., 2015], migration is important for linking the planet formation theory to the observables. The migration process is crucially dependent on the ability of the ambient disc material to liberate the excess thermal energy [Lyra et al., 2010; Dittkrist et al., 2014]. The so-called type I migration of low-mass embedded cores in locally isothermal discs leads to their fast [on a time scale shorter than the disc lifetime, Korycansky & Pollack, 1993] depletion, but finite relaxation rates can lead to reversal of the net torque [Paardekooper & Mellema, 2006; Kley & Crida, 2008; Kley et al., 2009] by enhancing the corotation torque [Baruteau & Masset, 2008]. The relaxation rate (fast or slow) in this context is a comparison between the radiative relaxation time and the libration time of the gas being on the horseshoe orbit, the gas exerting the corotation torque.

## 0.3 Radiative energy transfer

### 0.3.1 Radiative transfer and energy evolution equations

Radiative transfer equation reads:

$$\left[c^{-1}\partial_t + \vec{n}\cdot\vec{\nabla}\right] I_\nu(\vec{\xi}) = j_\nu(\vec{\xi}) - \varkappa_\nu(\vec{\Psi}(\vec{\xi}))\varrho(\vec{\xi})I_\nu(\vec{\xi}), \tag{4}$$

[‡]also known as the Goldreich-Schubert-Fricke (GSF) instability in the context of differentially rotating stars

where $I_\nu$ is the intensity of the radiation field, $j_\nu$ is the emissivity of the medium, $\vec{\xi} = \{\vec{n}, \vec{r}, t\}$, $\vec{\psi} = \{\varrho, P, T\}$, $\varkappa_\nu(\vec{\psi}(\vec{\xi}))$ is the cross-section per unit mass of the matter and is usually called opacity. Thus, in general, specific intensity has 7 degrees of freedom: $\vec{\xi} = \{\vec{n}, \vec{r}, t\}$. It is clear, however, that the symmetries of a problem can make the radiation field well described by less-dimensional quantities. That's why it is useful to consider the angular moments of (4), not least of all because they enlighten the underlying physics. In the focus of our interest is the zero-order moment integrated over frequencies:

$$\partial_t E_{\rm rad} + \vec{\nabla}\cdot\vec{F}_{\rm rad} = \int d\nu \oint d\Omega\, (j_\nu - \varkappa_\nu \varrho I_\nu), \tag{5}$$

where

$$E_{\rm rad} = \frac{4\pi}{c}\int d\nu J_\nu = \frac{1}{c}\int d\nu \oint d\Omega\, I_\nu(\vec{\xi}) \tag{6}$$

is the radiation energy density,

$$\vec{F}_{\rm rad} = \int d\nu \oint d\Omega\, I_\nu(\vec{\xi})\vec{n} \tag{7}$$

is the flux of radiative energy. Equation (5) taken with minus sign gives a radiative heating-cooling source term in the fluid's energy equation:

$$\partial_t E_{int} + \vec{\nabla}\cdot(E_{int}\cdot\vec{u}\,) = -P\vec{\nabla}\cdot\vec{u} - d_t E_{\rm rad} \tag{8}$$

Non-MC numerical schemes for radiative transfer, which are coupled with hydrodynamic simulations, often split the radiation field into two parts [e.g. Kuiper et al., 2010b]. Namely, the one coming from a local irradiation source (e.g. a star, usually inside an unresolved cell or a sink particle) and the thermal diffusive radiation field emerging from the warmed-up fluid itself. Such a splitting is justified numerically because the first part can be evaluated with more accurate ray tracing technique and the second one can be readily approximated with flux-limited diffusion [Levermore & Pomraning, 1981]. Thus, we write $E_{\rm rad} = E_* + E_{\rm diff}$, $\vec{F}_{\rm rad} = \vec{F}_* + \vec{F}_{\rm diff}$ and assume:

$$\partial_t E_* + \vec{\nabla}\cdot\vec{F}_* = \int d\nu \int_{\partial\Omega} [-\varkappa_\nu \varrho I^*_\nu] \tag{9}$$

$$\partial_t E_{\rm diff} + \vec{\nabla}\cdot\vec{F}_{\rm diff} = \int d\nu \oint d\Omega \left[j_\nu - \varkappa_\nu \varrho I^{\rm diff}_\nu\right] \tag{10}$$

The first term accounts for the irradiation from an 'outer' with respect to the point under consideration source, the second one - for the thermal diffusive radiation field at this point. $\partial\Omega$ is a solid angle, subtended by the irradiation source. If we add (9) and (10) up, we get (5). It is clear that in the optically thin regions in the vicinity of the irradiation source $E_*$ dominates over $E_{\rm diff}$ and vice

versa. The flux-limited diffusion imposes

$$\vec{\nabla}\cdot\vec{F}_{\rm diff} = -\frac{\Lambda c}{\varkappa_{\rm R}\varrho}\vec{\nabla}E_{\rm diff}, \tag{11}$$

where $\Lambda$ is a flux limiter Levermore & Pomraning [1981],

$$\varkappa_{\rm R} = \frac{acT^3/\pi}{\int \varkappa_\nu^{-1}\partial_T B_\nu d\nu} \tag{12}$$

is called Rosseland mean opacity.

### 0.3.2 LTE

In case of gas, $j_\nu$ is defined by the levels populations, which, in general, have to be found from solving the statistical equilibrium with radiative transfer alone. In case of local thermodynamic equilibrium (LTE), any process (being it f-f, b-f or f-b transitions, or chemical reaction, etc.)

$$\mathcal{A}+\mathcal{B}+\mathcal{C}+\cdots = 1+2+3+\cdots$$

is in detailed balance:

$$n_{\mathcal{A}}n_{\mathcal{B}}n_{\mathcal{C}}\cdots R(\mathcal{ABC}\cdots\to 123\cdots) = n_1n_2n_3\cdots R(123\cdots\to\mathcal{ABC}\cdots). \tag{13}$$

Here $n$ designates number densities and $R$ – the reaction rates. Then the energy-level populations are related by the Saha equation

$$\frac{n_1n_2n_3\cdots}{n_{\mathcal{A}}n_{\mathcal{B}}n_{\mathcal{C}}\cdots} = \frac{U_1\mathfrak{L}_1^{-3}U_2\mathfrak{L}_2^{-3}U_3\mathfrak{L}_3^{-3}\cdots e^{-(E_1+E_2+E_3\cdots)/kT}}{U_{\mathcal{A}}\mathfrak{L}_{\mathcal{A}}^{-3}U_{\mathcal{B}}\mathfrak{L}_{\mathcal{B}}^{-3}U_{\mathcal{C}}\mathfrak{L}_{\mathcal{C}}^{-3}\cdots e^{-(E_{\mathcal{A}}+E_{\mathcal{B}}+E_{\mathcal{C}}\cdots)/kT}} \tag{14}$$

with the local gas temperature $T = T_{\rm gas}$, partition functions $U = \sum g_j e^{-E_j/kT}$ and thermal de Broglie wavelengths $\mathfrak{L} = h/\sqrt{2\pi mkT}$. For a gas of density $\varrho$ in such an equilibrium Kirchhoff's law is valid:

$$j_\nu(\vec{\xi}) = \varrho(\vec{\xi})B_\nu(T). \tag{15}$$

It is important to mention here that LTE assumption alone does not put similar constrain on the intensity of the radiation field, which can still differ from its local equilibrium value $B_\nu(T)$ and has to be determined from (4).

As soon as we would like to conclude on basic properties of radiative source term (8) introduced by gas opacity, let us consider the clearest case. Namely, let us assume LTE approximation is valid.

Further, according to our splitting of the radiation field, let us approximate the irradiation flux with that from a black-body source in an optically-thin medium, and assume the diffusive part to be isotropic. Integrating the rhs of (6) over solid angles and frequencies while making use of (9) and (10), we get for $d_t E_{\text{rad}}$ at point $\vec{x}$

$$\begin{aligned} d_t E_{\text{rad}}(\vec{x}) = &-\kappa_{\text{P}}\left(T_{\text{gas}}, T_{\text{rad}}\right) \varrho F_*(\vec{x}) - \kappa_{\text{P}}\left(T_{\text{gas}}\right) \varrho c\, E_{\text{diff}}(\vec{x}) + \\ &+ \kappa_{\text{P}}\left(T_{\text{gas}}\right) \varrho c\, a T^4, \end{aligned} \tag{16}$$

where $T = T(\vec{x})$ is a local temperature, $T_*$ characterizes the flux of the irradiation source,

$$\kappa_{\text{P}}\left(T_{\text{gas}}, T_{\text{rad}}\right) = \frac{\int \kappa_\nu(T) B_\nu(T_*) d\nu}{\sigma T_*^4/\pi} \tag{17}$$

is a two-temperature (2-T) Planck averaged opacity,

$$\kappa_{\text{P}}\left(T_{\text{gas}}\right) = \kappa_{\text{P}}(T_* = T, T) \tag{18}$$

is a single-temperature (1-T) Planck mean opacity or, simply, Planck average.

$$F_*(\vec{x}) = \sigma T_*^4 \left(\frac{R_*}{r}\right)^2 e^{-\tau_{\text{P}}(\vec{r})} \tag{19}$$

is the irradiation flux at point $\vec{x}$, which is at distance $r = |\vec{r}|$ from the source,
$\tau_p(\vec{r}) = \int \varrho \kappa_{\text{P}}\left(T_{\text{gas}}, T_{\text{rad}}\right) dr$ is the Planck mean optical depth along that direction.
If the gas is in the hydrostatic equilibrium ($\vec{u} = 0$), equation 8 turns:

$$\begin{aligned} d_t E_{int} = -d_t E_{\text{rad}} = &\kappa_{\text{P}}\left(T_{\text{gas}}\right) \varrho c \left[E_{\text{diff}} - a T^4\right] + \\ &+ \kappa_{\text{P}}\left(T_{\text{gas}}, T_{\text{rad}}\right) \varrho F_* \end{aligned} \tag{20}$$

Plugging in Joule's law for the internal energy of a perfect gas $E_{int} = \varrho C_{\text{v}} T$ and considering 'instant' equilibrium chemistry ($\partial_t C_{\text{v}}(t, T) = 0$), we get:

$$\begin{aligned} \left(T \partial_T C_{\text{v}} + C_{\text{v}}(T)\right) d_t T = &\kappa_{\text{P}}\left(T_{\text{gas}}\right) c \left[E_{\text{diff}} - a T^4\right] + \\ &+ \kappa_{\text{P}}\left(T_{\text{gas}}, T_{\text{rad}}\right) F_* \end{aligned} \tag{21}$$

### 0.3.3 Optically Thin Limit

If in addition the volume under consideration remains optically thin at all frequencies, equation 20 simplifies further to:

$$d_t T = \frac{\varkappa_{\mathrm{P}}\left(T_{\mathrm{gas}}, T_{\mathrm{rad}}\right) caT_*^4 \left(R_*/2r\right)^2 - \varkappa_{\mathrm{P}}\left(T_{\mathrm{gas}}\right) caT^4}{\left(T\partial_T C_{\mathrm{v}} + C_{\mathrm{v}}\right)} \tag{22}$$

The equilibrium temperature is defined to satisfy $d_t T_{eq} = 0$. This equation lets us compute the equilibrium temperature directly without solving the radiative transfer as soon as the ratio of 2-T to 1-T Planck average opacity is known as a function of temperature and density:

$$T_{\mathrm{eq}} - T_* \left(\frac{R_*}{2r}\right)^{1/2} \left(\frac{\varkappa_{\mathrm{P}}\left(T_{\mathrm{gas}}, T_{\mathrm{rad}}\right)}{\varkappa_{\mathrm{P}}\left(T_{\mathrm{gas}}\right)}\right)^{1/4} = 0 \tag{23}$$

Equations (22) and (23) are of a prime focus of the present study. From (23) one can immediately see that non-monotonic behaviour of the ratio $\varkappa_{\mathrm{P}}\left(T_{\mathrm{gas}}, T_{\mathrm{rad}}\right)/\varkappa_{\mathrm{P}}\left(T_{\mathrm{gas}}\right)$ with the gas temperature can introduce multiple solutions to the equilibrium gas temperature.

## 0.4 Dissertation outline

In Chapter 2 we describe our calculations of the mean opacity of molecular gas. Results presented in Chapters 2 and 3 were published in Malygin et al. [2014]. Chapter 4 presents our calculations of thermal relaxation time for T Tau and Toomre $Q = 1$ discs. The results obtained for this chapter are submitted to publication in Astronomy & Astrophysics. Chapter 5 contains preliminary results on frequency-binned gas opacity calculations – a new technique that allows accurate yet computationally affordable treatment of frequency dependent gas opacity in hydrodynamic and radiative transfer numerical modelling (in preparation). A short summary and outline of future work is in the closing Chapter 6.

*If you don't know the answer, assume zero*

humans' wisdom

# 1 Mean Gas Opacity

Results presented in this chapter have gone through a peer review process and were published in Malygin et al. [2014].

## 1.1 Motivation & disclaimer

There are two motivations for calculating a new gas opacity. First, the gas opacity tables available [Seaton et al., 1994; Bell & Lin, 1994; Helling et al., 2000; Semenov et al., 2003; Ferguson et al., 2005; Freedman et al., 2008; Helling & Lucas, 2009] do not include two-temperature Planck means, which we argue to be essential for our application cases. Second, Ferguson et al. [2005] compared single-temperature Planck means obtained by different groups and found a disagreement at gas temperatures $\log T_{\rm gas} \geqslant 3.12$: only data from Ferguson et al. [2005] and Seaton et al. [1994] agree at atomic temperatures $\log T_{\rm gas} \geqslant 3.48$ [see Fig. 12 in Ferguson et al., 2005]. The discrepancy at lower gas temperatures originates from insufficient frequency sampling in earlier studies, although some contributions might have come from utilising different molecular line lists and/or equations of state. The two factors suggest that an independent computation of gas opacity is justified. My calculations of mean gas opacities are based on three major simplifying assumptions: equilibrium chemistry, local

thermodynamic equilibrium, and an ideal gas equation of state. The data presented in this chapter is for zero value of the microturbulence parameter. Not all of these conditions may be fulfilled in a circumstellar environment. Regions that are optically thin to stellar radiation could be affected by the change in abundances due to photochemistry. Whereas turbulent broadening can be easily taken into account via its parametrisation, giving up any of the three simplifications mentioned above could have entailed a noticeable increase in computational time. Equilibrium chemistry assumption should also be viewed as a first-order approximation from the perspective of utilising the advanced gas opacities in massive numerical hydrodynamic (HD) + radiative transfer (RT) simulations. Moreover, current studies disagree in Planck mean gas opacities even though they employ a similar simplified approach. Thus, the framework outlined above is suitable for an initial step further enabling direct comparison with Ferguson et al. [2005]. Connection to low-temperature atmospheric opacity from Freedman et al. [2008] revealed unexpected correspondence, which we will utilise in Chapter 4. Our Planck means disagree with Helling et al. [2000] because of their insufficient frequency sampling (see Sect. 1.5.5).

## 1.2 Calculations

For the calculations I adopted the open-source code DFSYNTHE* by Kurucz and Castelli [described in Castelli, 2005]. Originally, the code was intended to calculate opacity probability distribution functions [Kurucz, 1970; Kurucz et al., 1974], which means the opacity spectrum $\kappa_\nu$ is determined during the computation. So, I implemented the calculation of the Rosseland, the Planck and two-temperature Planck means. A detailed description of all the computational methods and opacity sources can be found in Kurucz & Avrett [1981] and I will not repeat it here. Except for some major points of line opacity calculations and minor modifications in opacity sources.
There is a list of input parameters the user should supply: atomic abundances, abundance scaling factors (metallicities), gas pressures, gas temperatures, and radiation temperatures. I created the input files for a range of gas densities ($10^{-20} - 10^{-2}$ g cm$^3$), gas temperatures ($700 - 10^6$ K), and for three different metallicities ($-0.3$, 0.0, 0.3 dex). For the two-temperature Planck means I considered $3\,000\ \mathrm{K} < T_{\mathrm{rad}} < 30\,000$ K. If needed, a wider parameter range can be considered. The code at first calculates equilibrium abundances of compounds and equilibrium level populations. Using those, it works through the line lists to calculate the line absorption, which is added to the continuum absorption to get the total opacity spectrum. Finally, the requested forms of frequency averages are calculated for each set of input parameters. All the calculations were done assuming equilibrium chemistry governed by local thermodynamic equilibrium (LTE), and an ideal gas equation of state and the reference values for solar metallicity atomic abundances from Grevesse & Sauval [1998].

*Available from http://wwwuser.oat.ts.astro.it/castelli/sources/dfsynthe.html

## 1.3 Line absorption

The line and continuum opacity data are taken from Kurucz's CD-ROMs Ns 1, 15, and 20-24[†] [Kurucz, 1993a,b]. Among the compounds included are: $H_2O$, TiO, CO, $CO_2$, $H_2S$, $H_2$, NH, HF, MgH, AlH, SiH, HS, HCl, $C_2$, CN, AlC, SiC, CS, $N_2$, NO, MgN, AlN, $NH_2$, NS, $O_2$, MgO, AlO, SiO, SO, CaO, FeO, MgS, AlS, SiS, $S_2$, CaS, FeS, $C_2H$, CNH, COH, NOH, OOH, $CH_2$. These have prominent absorption bands at temperatures $500 - 1000$ K as well as in the UV, which is important for the two-temperature Planck mean. For all molecules but water I rely on the Kurucz's data. For the water I compiled a line list based on BT2 data [Barber et al., 2006] and used a partition function from Vidler & Tennyson [2000]. BT2 is one of the most complete line lists for main water isotopologue $^1H_2^{16}O$ comprising over 500 million transitions in the range from 0.35 $\mu$m to 60 $\mu$m. All the line lists were re-sampled at a resolving power of $R = \lambda/\partial\lambda = 500\,000$. At this resolution ($\geqslant 3.5 \times 10^6$ wavelength points) the opacity spectrum is calculated over the wavelength range of 8.9 nm–10 $\mu$m. The Rosseland mean can be equally well calculated with even a factor of $\sim 100$ lower resolution, because it is dominated by line wings (broad regions), but the Planck mean is dominated by line cores (narrow regions), which demands the Voigt profiles to be properly resolved and sampled (see Sect. 1.5.5).

For all species of the line data, the line absorption coefficient is calculated on a given frequency grid according to the formula [see Castelli, 2005]

$$l_\nu = \frac{1}{\varrho}\frac{\sqrt{\pi}e^2}{m_e c} f_{ij} \frac{g_i N_j}{U_j} \exp\left(\chi_i/kT\right) \times \frac{1}{\Delta\nu_D} \times H\left(\frac{\Gamma}{4\pi\Delta\nu_D}, \frac{\Delta\nu}{\Delta\nu_D}\right) \times \left(1 - \exp\left(-h\nu/kT\right)\right), \tag{1.1}$$

where $\varrho$ is the gas mass density, e is the charge of an electron, $m_e$ is the electron mass, $c$ is the speed of light; $f_{ij}$ corresponds to the Ladenburg $f$ or oscillator strength, $g_i$ is statistical weight of the lower level $i$, $N_j$ is number density of the absorbing species in the $j$ ionisation stage, $U_j$ is partition function of the absorbing species in the $j$ ionisation stage, $\chi_i$ is ionisation potential from the lower $i$ level; $\Delta\nu_D = \nu_o/c\sqrt{2kT/\mu + \xi_t^2}$ is the total Doppler broadening of the transition at the $\nu_o$ frequency, with $k$ being the Boltzmann constant and $\mu$ the mean molecular weight, $\xi_t$ the additional non-thermal broadening parameter, e.g. due to turbulent motions, usually called microturbulence parameter. The Voigt function is given by

$$H(a, v) = \frac{a}{\pi}\int_{-\infty}^{+\infty} \frac{\exp\left(-y^2\right) dy}{\left(v - y\right)^2 + a^2} \tag{1.2}$$

[†] http://kurucz.harvard.edu/cdroms.html

with $a = \Gamma/(4\pi\Delta\nu_D)$ and $v = \Delta\nu/\Delta\nu_D$; $\Gamma = \Gamma_L + \Gamma_S + \Gamma_W$ is a sum of Lorentz (natural), Stark (collisions with electrons), and van der Waals (collisions with neutrals) damping factors. If not specified in the line list, the damping factors are as follows. The radiative damping factor is set to the classical (Lorentz) damping [Peytremann, 1972; Kurucz & Avrett, 1981]

$$\Gamma_L = \frac{2.223 \times 10^{13}}{(\lambda[\mathrm{nm}])^2}[\mathrm{sec}^{-1}]. \tag{1.3}$$

For the Stark damping, the collisions with electrons are taken into account in the impact approximation: $\Gamma_S/n_e = \beta_S = \text{const}$. The following fits are adopted following Kurucz & Avrett [1981]

$$\beta_S[\mathrm{cgs}] = \begin{cases} 10^{-5} & \text{for molecules;} \\ 10^{-8} n_{\mathrm{eff}}^5 & \text{for atoms.} \end{cases}$$

with $n_{\mathrm{eff}}$ being the effective quantum number of the upper state,

$$n_{\mathrm{eff}}^2 = \frac{\mathrm{Ry} Z_{\mathrm{eff}}^2}{\chi - E_u}, \tag{1.4}$$

where Ry = 13.6 eV is the Rydberg energy, $Z_{\mathrm{eff}}$ is the effective charge[‡], $\chi$ is the ionisation potential from level $E_u$. If the upper level is above the ionisation potential (ionisation to an excited level of the parent), $n_{\mathrm{eff}} = 5$. The code approximates the van der Waals broadening taking into account the polarization of atomic and molecular hydrogen and neutral helium [Kurucz & Avrett, 1981] in the following manner:

$$\Gamma_W = \begin{cases} 10^{-7} \frac{n_H}{Z_{\mathrm{eff}}} \text{ for molecules} \\ 4.5 \times 10^{-9} \langle r^2 \rangle^{0.4} \left(n_H + 0.42 n_{He} + 0.85 n_{H_2}\right) \left(\frac{T}{10^4}\right)^{0.3} \text{ for atoms} \end{cases}$$

If the coefficient in front of the parentheses in the lower equation in 1.3 is not specified, the mean-square-radius of the upper level is calculated as described in Kurucz & Avrett [1981].
We set $\xi_t = 0$, facilitating comparison to other data (see Sect. 1.5.5).

[‡] = 1 for Fe I, 2 for Fe II, etc.

## 1.4 Frequency averages

Total absorption is a sum of line and continuum absorptions from all the species: $\varkappa_\nu = l_\nu + \sigma_\nu$. From the frequency-dependent opacities $\varkappa_\nu$ we calculate the Rosseland mean

$$\varkappa_{\mathrm{R}}^{-1}\left(T_{\mathrm{gas}}\right) = \frac{\int \varkappa_\nu^{-1}\left(T_{\mathrm{gas}}\right) \times \partial_T B_\nu\left(T_{\mathrm{gas}}\right) d\nu}{\int \partial_T B_\nu\left(T_{\mathrm{gas}}\right) d\nu}, \tag{1.5}$$

the two-temperature Planck mean

$$\varkappa_{\mathrm{P}}\left(T_{\mathrm{gas}}, T_{\mathrm{rad}}\right) = \frac{\int \varkappa_\nu(T_{\mathrm{gas}}) \times B_\nu(T_{\mathrm{rad}}) d\nu}{\int B_\nu(T_{\mathrm{rad}}) d\nu}, \tag{1.6}$$

and the single-temperature Planck mean

$$\varkappa_{\mathrm{P}}\left(T_{\mathrm{gas}}\right) = \varkappa_{\mathrm{P}}\left(T_{\mathrm{gas}}, T_{\mathrm{rad}} = T_{\mathrm{gas}}\right) = \frac{\int \varkappa_\nu(T_{\mathrm{gas}}) \times B_\nu(T_{\mathrm{gas}}) d\nu}{\int B_\nu(T_{\mathrm{gas}}) d\nu}. \tag{1.7}$$

In the following section we present the results of the calculations.

## 1.5 Results

In this section, all the values of gas opacity are given for solar atmospheric atomic abundances [Grevesse & Sauval, 1998] and zero turbulent broadening unless otherwise stated. However, different authors used different references for solar abundances. We will focus on the single-temperature and the two-temperature Planck mean because these are the points of major improvement in comparison to previous studies.

### 1.5.1 Single-temperature Planck mean

The surface plot in Fig. 1.1 shows the single-temperature Planck mean gas opacity as a function of gas temperature and density. The iso-contours reveal regions with steep and shallow gradients of $\varkappa_{\mathrm{P}}$ with respect to these parameters. These are caused by changes in equilibrium abundance of the species, level populations in atoms and molecules and by the shift of the maximum of the weighting Planck function. We briefly highlight the processes that shape the surface. At gas temperatures $\leqslant 1\,000$ K, a ubiquity of numerous molecular lines from different species make different parts of an opacity spectrum within the correspondent wavelength region of $1 - 50$ $\mu$m look alike, so that the frequency-averaged values vary moderately with temperature and density. This is responsible for the flattish region in the top-left corner of the surface. In the temperature range from 1 000 K to 3 000 K there is a gap in opacity because none of the species that comprise the gas mixture has prominent

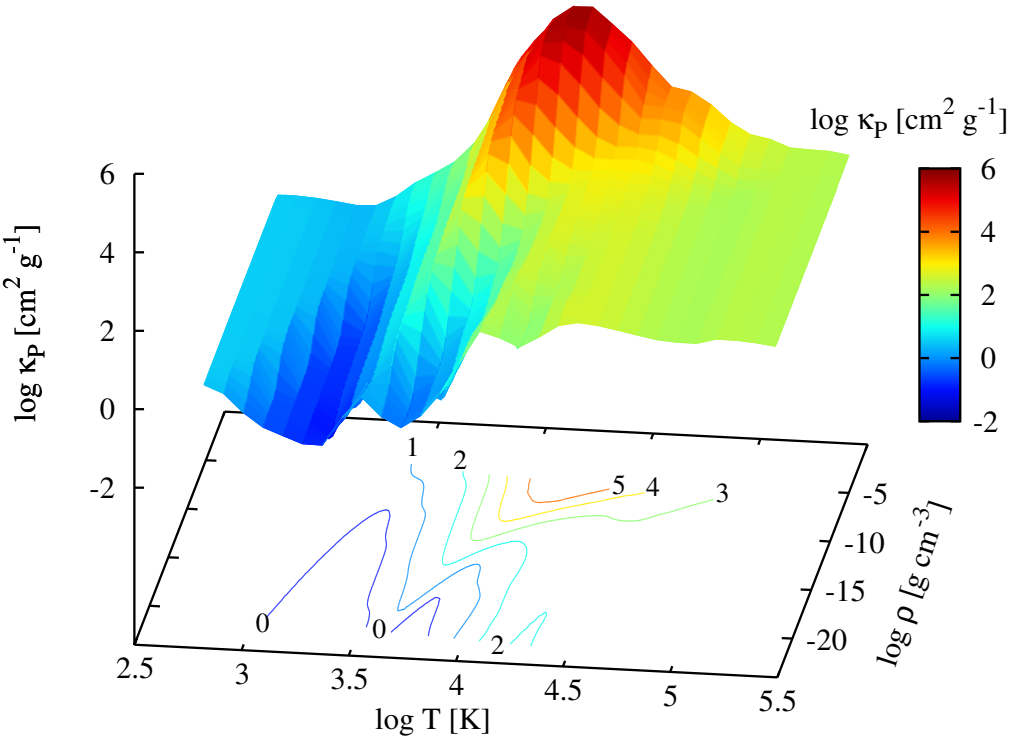


**Figure 1.1:** Surface of the Planck mean gas opacity in logarithmic parameter space. The contours on the xy-plane are iso-contours $\log \varkappa_P = \text{const}$, the labels giving the values. The colour scale is the same as the height-scale.

bands in the corresponding wavelength region. The gap is pronounced at low densities, but is filled at the highest densities because of enormous pressure-broadening of the lines, in particular those from alkali atoms [see Sect. 1.5.4, as well as Freedman et al., 2008].

The rising opacity from $H^-$, H, and metals results in the high bump, which peaks at $\sim 10^4$ K. The mean opacity on the top of the "mountain" is governed by H bound-bound (b-b), bound-free, and free-free absorption. The contribution from atomic metals at these temperatures comes at higher frequencies and therefore is exponentially suppressed by the Wien cut. At higher temperatures the ionisation of hydrogen eliminates its b-b source of opacity and the mean opacity starts to decline. To the right of the larger hydrogen hump there is a smaller helium hump. Free-free and metal line absorption dominate the mean at higher temperatures up to $10^6$ K. At these temperatures the Planck mean drops moderately with density, but is sensitive to metallicity. Finally, it settles at the wavelength-independent Thomson scattering cross-section, which results in a plateau at temperatures $\geqslant 10^6$ K (not shown in the plot).

### 1.5.2 Two-temperature Planck mean

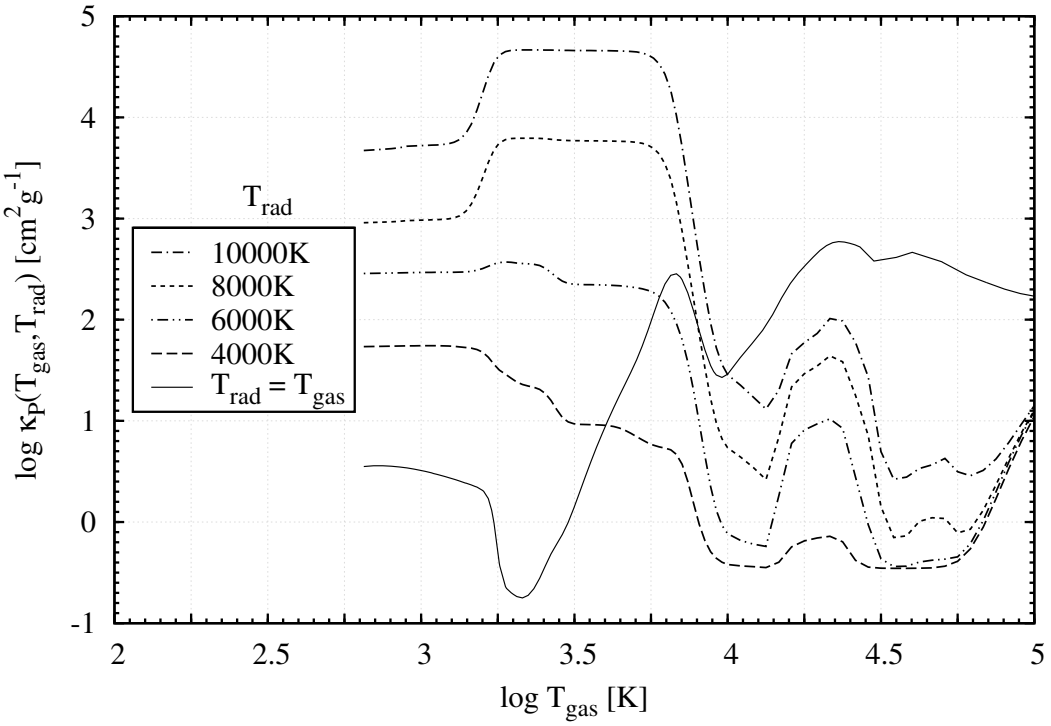


**Figure 1.2:** Two-temperature Planck mean opacity as a function of gas temperature. The plot is for a constant density of $10^{-13}$ g cm$^{-3}$ and for different radiation temperatures $T_{\rm rad}$, as indicated in the legend. The single-temperature Planck mean $\left(T_{\rm rad} = T_{\rm gas}\right)$ at the same density is shown in solid.

Figure 1.2 shows the two-temperature Planck mean as a function of gas temperature for several radiation temperatures and at a constant density of $10^{-13}$ g cm$^{-3}$. It is clearly seen from the plot that $\kappa_{\rm P}(T_{\rm gas}, T_{\rm rad} > T_{\rm gas}) > \kappa_{\rm P}(T_{\rm gas} = T_{\rm rad})$. This is because the parts of the opacity spectrum, which get exponentially cut by the Wien factor in the single-temperature Planck mean ($T_{\rm gas} = T_{\rm rad}$), are becoming pronounced by the Planck function with higher temperature in the two-temperature Planck mean. Consequently, at a constant gas temperature, $T_{\rm gas}$, $\kappa_{\rm P}\left(T_{\rm gas}, T_{\rm rad}\right)$ is higher for higher radiation temperatures. The ratio $\kappa_{\rm P}\left(T_{\rm gas}\right)/\kappa_{\rm P}\left(T_{\rm gas}, T_{\rm rad}\right)$ differs from $\kappa_{\rm P}\left(T_{\rm gas}\right)/\kappa_{\rm P}\left(T_{\rm rad}\right)$, especially at $T_{\rm rad} \geqslant 5\,700$ K. The qualitative look of the plot remains the same for other densities.

### 1.5.3 Metallicity

Figure 1.3 presents the Rosseland and the single-temperature Planck means at a constant gas density of $10^{-8}$ g cm$^{-3}$ as functions of gas temperature for three different metallicities: [Me/H] = −0.3, 0.0,

and 0.3. Other metallicities may be readily added on demand.

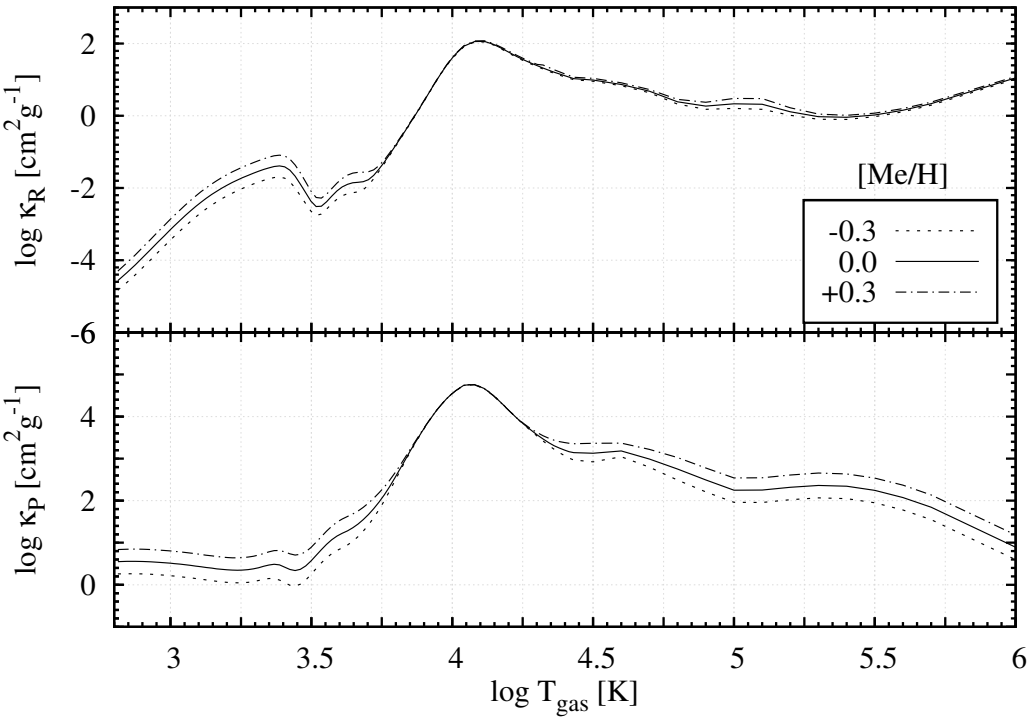


**Figure 1.3:** Rosseland (top panel) and single-temperature Planck (bottom panel) means versus gas temperature. Logarithms of the values are plotted for $\varrho = 10^{-8}$ g cm$^{-3}$ at three different metallicities, indicated in the legend.

Varying metallicity affects the means at high temperatures via atomic metal absorption and at low temperatures via change in the contents of the compounds. In between, the opacity is dominated by hydrogen bound-bound, bound-free and free-free absorption (see Sect. 1.5.1) and is insensitive to the amount of metals. The hydrogen temperatures $5\,700 - 17\,700$ K are clearly distinguished in each panel. At molecular temperatures $\leqslant 5\,700$ K both means show the dependence on metallicity, but at metallic temperatures $\geqslant 17\,700$ K the Planck mean depends more strongly on the metal abundance than the Rosseland mean does. This is because the Planck mean is being dominated by line cores from metals in this temperature regime.

### 1.5.4 Connection to low temperature atmospheric opacity

Freedman et al. [2008] calculated the gas opacity relevant for high gravity environments, where formation and settling of condensates into clouds occur and considered a mixture of only 11 molecules and 5 alkali elements: $H_2O$, TiO, CO, $CO_2$, $H_2S$, $CH_4$, $NH_3$, $PH_3$, VO, FeH, CrH, and

Li, Na, K, Cs, Rb, respectively. In contrast, our calculations apply for low gravity equilibrium gas chemistry with no settling. We include more than 40 compounds, five of which overlap with the first five listed above, as well as such alkali atoms as Li, Na, and K, but not Cs and Rb. We extend the parameter space up to $10^{-2}$ g cm$^{-3}$ to compare the two studies.

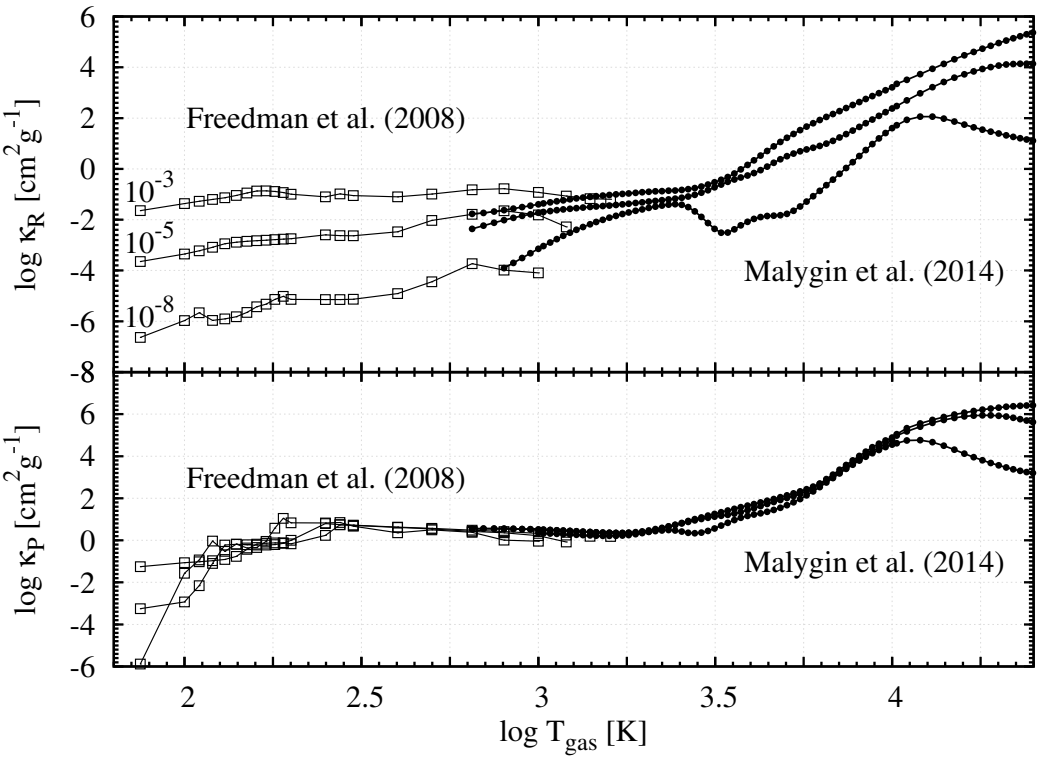


**Figure 1.4:** Comparison with low-temperature atmospheric opacity: Rosseland means (*top panel*) and Planck means (*bottom panel*). The open squares are data from Freedman et al. [2008], the filled circles are from this work. Each curve corresponds to a constant gas density $\varrho[\,\mathrm{g\,cm^{-3}}] = 10^{-3}, 10^{-5}, 10^{-8}$, but the Planck means are not sensitive to this.

Figure 1.4 shows a connection between Freedman et al. [2008] and this work. The iso-density contours of the Rosseland mean opacity from the two works cross each other. This indicates that there is an overlap region, where both determine similar opacity values, despite the fact that the included species differ significantly. The intersection temperatures of the Rosseland means increase with density: 650 K (the lowest temperature in our calculations) for $10^{-8}$ g cm$^{-3}$, 1 400 K for $10^{-3}$ g cm$^{-3}$, and 4 000 K (the upper boundary of Freedman's calculations) for $10^{-2}$ g cm$^{-3}$. The Planck mean is to a high degree density-independent in the region of overlap: the iso-density contours pile up at about one value ($\log \varkappa_P \approx 0.5$). The intersection temperatures for densities $\leqslant 10^{-4}$ g cm$^{-3}$ correspond to the lower boundary of our calculations (650 K), and get higher at the highest densities (1 500 K and 10 000 K at $10^{-3}$ and $10^{-2}$ g cm$^{-3}$, respectively).

To explain this we have to consider the difference in the species included in the two calculations and establish the temperature ranges of importance for each group of those species. The species $CH_4$, $NH_3$, $PH_3$, CrH, FeH, and VO, which are not included in our calculations although they are in Freedman et al. [2008], have prominent bands within $\sim 5 - 1\,000\ \mu$m [see Fig. 4 in Freedman et al., 2008, and references therein]. Accordingly, they contribute to the mean opacity at temperatures $\leqslant 1\,000$ K. The species included in each calculation, $H_2O$, TiO, CO, $CO_2$, and $H_2S$, are relevant absorbers at temperatures $\geqslant 1\,000$ K because they have prominent bands within $\sim 0.1 - 5\ \mu$m. In the intermediate region ($1 - 5\ \mu$m) the opacity from alkali atoms Li, Na, K, Cs, and Rb is prominent, especially at high pressures. Freedman et al. [2008] included more alkali species (Cs, Rb) and applied a more sophisticated collisional broadening prescription, suited for pressures as high as $10^7 - 10^8$ dyn cm$^{-2}$ [Burrows et al., 2000; Burrows & Volobuyev, 2003]. As inferred from those works, the pressure-enhanced far-wings from alkali atoms make a significant contribution to the Rosseland mean at temperatures about $1\,000 - 1\,500$ K. That is why the Rosseland means intersect within this region and the value of the intersection temperature increases with density. The Planck mean is dominated by line cores, and is less sensitive to pressure: a contribution from the alkali atoms appears only at densities as high as $\geqslant 10^3$ g cm$^{-3}$.

The above reasoning is a qualitative analysis of the connection between the two data sets. A quantitative consideration would have involved a comparison between the prescriptions of collisional broadening and accounted for the effects of relative abundances. We simply remark that the intersection temperatures would be somewhat higher should we decrease in our calculations the abundance of the common species bearing the same atoms as those composing the remaining species in Freedman et al. [2008].

### 1.5.5 Comparison to other studies

Figure 1.5 shows a comparison of mean opacities as obtained by different groups. The top panel shows the Rosseland mean, and the bottom panel the Planck mean. Each panel corresponds to the same density of $10^{-10}$ g cm$^{-3}$. Data from Ferguson et al. [2005] include opacity from dust grains. Data from both Helling et al. [2000] and this work are pure gas opacity. Nonetheless, our Planck means compare to dust opacity at temperatures below 1 500 K: high absorption in line cores is able to provide the Planck average, comparable to that from continuum opacity of typical ISM dust. The Rosseland mean opacity of the dust, however, dominates over Rosseland mean gas opacity at low temperatures.

We note a good agreement with Ferguson et al. [2005] in both means. However, our calculations cover a wider parameter space in terms of temperature and density. To the best of our knowledge, this is the largest set of mean gas opacities obtained within one framework, using a single computer code.

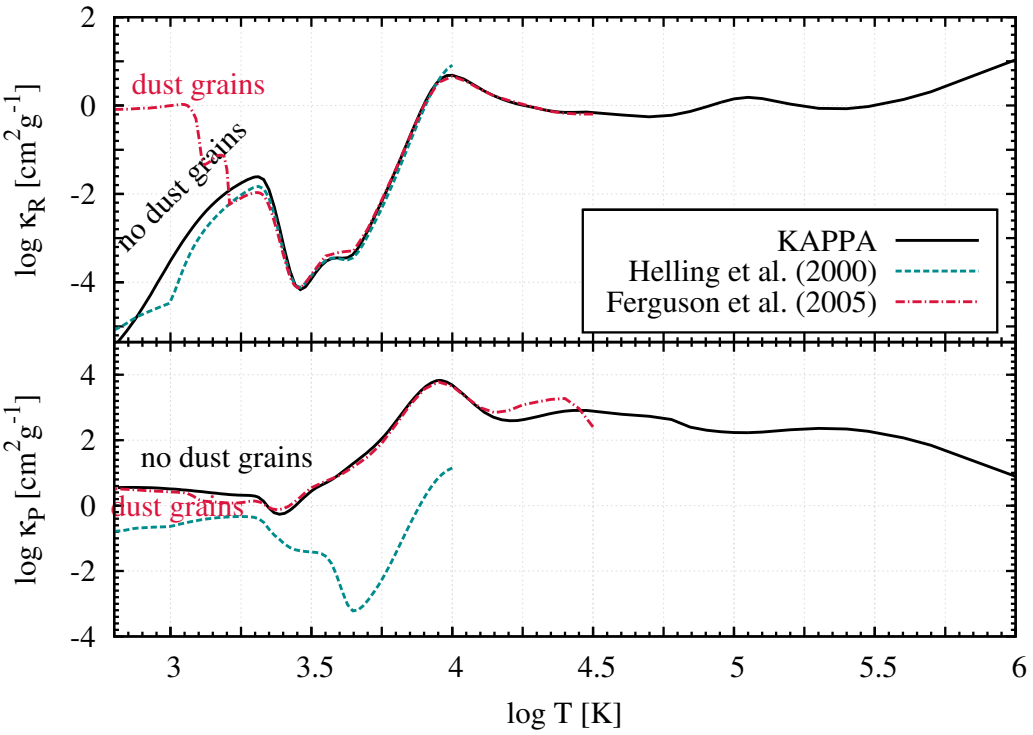


**Figure 1.5:** Rosseland (*top panel*) and Planck (*bottom panel*) means at a constant gas density of $10^{-10}$ g cm$^{-3}$: comparison with other studies. This work – solid black line, Helling et al. [2000] – marine dashed, and Ferguson et al. [2005] – red dot-dashed. Data from Ferguson et al. [2005] contain opacity from dust grains. At lower temperatures, the Rosseland average is dominated by the dust continuum opacity, but the Planck means of the dust and the gas are comparable.

Because of the improper frequency sampling, Planck means from Helling et al. [2000] are significantly lower than ours or those from Ferguson et al. [2005]. Whereas the number of randomly picked frequencies was sufficient to produce a good approximation for the Rosseland mean values, this number is not sufficient for Planck mean averages, because Rosseland means are harmonic averages while Planck means are direct averages. There are not enough random frequency points to sample all absorption features sufficiently. This error is smaller for the Rosseland mean, but is substantial for the Planck mean. Because of the random[§] frequency sampling, the uncertainties introduced into the Planck opacities by under-sampling are not systematic, but are instead of a stochastic nature. To verify this statement, we choose the temperature of the biggest disagreement in single-temperature Planck means between Helling et al. [2000] and this work at the density of $10^{-10}$ g cm$^{-3}$ ($\approx$ 4 466 K; see Fig. 1.5) and perform $10^4$ calculations of Planck and Rosseland means each with $5 \times 10^3$ random frequencies. The resulting distributions of $10^4$ individually calculated

[§]actually, pseudo-random with respect to positions of the absorption features

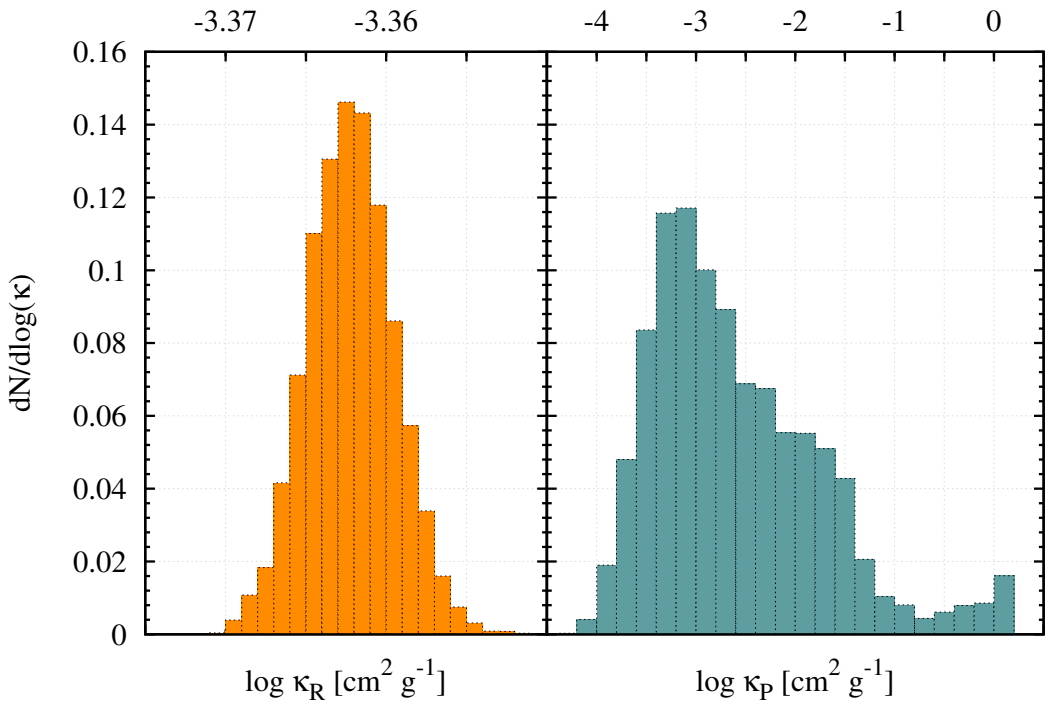


**Figure 1.6:** Normalised distributions of logarithms of Rosseland (left) and Planck (right) means. The values were determined at 4 466 K and $10^{-10}$ g cm$^{-3}$ and calculated from $5 \times 10^3$ sampling points randomly spread over the spectrum (8.9 nm $-$ 10 $\mu$m). Total number of trials is $10^4$. The fiducial values (those calculated from $\sim 3.5 \times 10^6$ sampling points) $\log \varkappa_R = -3.36317$ and $\log \varkappa_P = 1.296$ are marked with thick vertical lines. We note the different scales on the $x$-axes.

Rosseland and Planck means are shown in Fig. 1.6.

The distribution of the Rosseland mean is Gaussian-like, narrow, and peaks at the fiducial value of $\log \varkappa_R = -3.36317$. Instead, the distribution for the Planck mean is asymmetric, broad (encompassing four orders of magnitude), and lies below the fiducial value of $\log \varkappa_P \approx 1.296$. This behaviour is exclusively due to the difference in the averaging process: the Rosseland mean is attracted by low-opacity regions between the lines, whereas the Planck mean is attracted by the line cores. The regions between the lines are much wider than the line cores, yielding a higher chance to sample from these regions. The most probable values of the two distributions are almost equal ($\approx -3.3$) because as long as the lines are neglected, the continuum opacity is essentially flat around the Planck function maximum at the considered temperature. The Planck mean obtained in Helling et al. [2000] for the given temperature and density, $\log \varkappa_P \approx -3.2$, is close to this value.

*These our actors, as I foretold you, were all spirits, and are melted into air, into thin air*

William Shakespeare, The Tempest, Act IV, Scene 1

# 2

# Equilibrium Temperature Degeneracy in Optically Thin Gas

Equilibrium gas temperature degeneracy stems from radiative instability caused by, e.g., molecule formation [Schirrmacher et al., 2003]. The radiative cooling rate of an optically thin gas increases with its temperature if there is no phase transitions or radiative instability. If the gas temperature is around the point where at least one of its constituents experiences a transition from atomic to molecular phase, the gas can start to cool more efficiently because the excited molecules will radiate the thermal energy away (heating from the binding energy release competes with this process). After passing the transition, the derivative of the cooling rate with respect to gas temperature regains a positive value. This kind of a turnover in heating/cooling rate, being put into the framework of time evolution, leads to limit cycle instabilities that occur in cataclysmic variable events [where it is due to hydrogen ionisation; see Meyer, 1982]. Equilibrium temperature degeneracy facilitates spatial coexistence of cool and warm phases [Schirrmacher et al., 2003], which is consequently reflected in the observable structure of the medium [as is likely the case in TT Cyg; see Olofsson et al., 2000].

In this section we calculate radiative equilibrium in an optically thin gas and explain the equilibrium

temperature degeneracy.

## 2.1 Radiative Instability In Optically Thin Limit

For the sake of convenience lets rewrite (22) as $d_t T = f(r, T)$ with

$$f(r, T) = \frac{\varkappa_P\left(T_{gas}, T_{rad}\right) caT_*^4 \left(R_*/2r\right)^2 - \varkappa_P\left(T_{gas}\right) caT^4}{\left(T\partial_T C_v + C_v\right)} \tag{2.1}$$

The equilibrium temperature is then defined from $f(r, T_{eq}) = 0$. As already mentioned, there can be several equilibrium temperatures at given $r$. Some of them will be stable, some not. The criteria for the stability is readily obtained from the Liapunov's analysis. In the vicinity of $T_{eq}$ we can perform a Taylor expansion of $f(r, T)$. If the first derivative is non-zero, its sign will define whether the root is stable or not to small perturbations:

$$\frac{d(T - T_{eq})}{T - T_{eq}} = \partial_T f(r, T_{eq}) dt \tag{2.2}$$

$$\lambda_L(T_{eq}) = \partial_T^{-1} f(r, T_{eq}). \tag{2.3}$$

Here $\lambda_L$ is the Liapunov's exponent. If $\lambda_L < 0$, the small perturbation will decay exponentially at time-scale $|\lambda_L|^{-1}$. If $\lambda_L > 0$, it will grow exponentially at time-scale $\lambda_L^{-1}$ until entering non-linear regime. If $\partial_T f(r, T_{eq}) = 0$, the linear analysis is not enough.

The complicated nature of the heating-cooling mechanisms in the optically thin gas introduces thermal instability within certain temperature ranges [Weymann, 1960; Williams, 1967]. If in some point in the volume the temperature becomes equal to its local equilibrium value $T_{eq}$ such that $\lambda_L(T_{eq}) > 0$, a small deposit of energy (e.g., from hydrodynamical compression or change in the ambient radiation field) will kick the system out of this stage and make it evolve to the closest equilibrium temperature (in the direction defined by $d_t T \lessgtr 0$). The time it takes to evolve from a given $T$ to the nearest equilibrium point $T_0$:

$$\tau = \int_T^{T_0} \frac{dt}{f(t)} \tag{2.4}$$

As soon as such optically thin regions become a part of a hydrodynamic + radiative transfer simulation, one needs a proper treatment of the described above degeneracy in equilibrium temperature. The methods based on the iterative search for the solution of (23), like the one used in Kuiper et al. [2010b], apparently, can not resolve the issue. They are likely to jump between two equilibrium point precluding the scheme from converging. We suggest to follow the temporal

evolution of the thermal energy of the gas with a proper time-step. The actual value of this time-step can be found via comparison between the local time-scale (2.4) and the current time-step of the hydro scheme. If the second is longer than the first one, one can treat the gas as being always at the equilibrium temeprature: by either forcing a new value or by running a sub-loop iterations to gently bring all the connected variables (dust density) to this equilibrium. If the hydro-step resolves the gas temperature evolution time, the gas is at non-equilibrium temperature, which can not be determined by solving (23).

## 2.2 Illustrative example

The condition of radiative equilibrium in an optically thin gas, where local net flux of radiation is $\left|\vec{F}_{\rm rad}\right| = \int d\nu \oint d\vec{\Omega}\vec{F}_\nu$, reads

$$\kappa_{\rm P}\left(T_{\rm gas}\right) \times aT_{\rm gas}^4 = \kappa_{\rm F} \times \frac{\left|\vec{F}_{\rm rad}\right|}{c}, \tag{2.5}$$

where $a$ is the radiation constant and $\kappa_{\rm F} = \left|\vec{F}_{\rm rad}\right|^{-1} \int \kappa_\nu |\vec{F}_\nu| d\nu$ is the flux averaged opacity. If the source of radiation is a black body with temperature $T_{\rm rad}$ and the gas is in LTE with $T_{\rm gas}$, $\kappa_{\rm F}$ becomes the two-temperature Planck mean:

$$\kappa_{\rm P}\left(T_{\rm gas}\right) \times aT_{\rm gas}^4 = \kappa_{\rm P}\left(T_{\rm gas}, T_{\rm rad}\right) \times \frac{\left|\vec{F}_{\rm rad}\right|}{c}. \tag{2.6}$$

The equilibrium gas temperature, therefore, depends on $\left|\vec{F}_{\rm rad}\right|$ and $T_{\rm rad}$.
If the radiation source is a star with effective temperature $T_*$ and radius $R_*$, located at distance $r \gg R_*$ from the point under consideration, the flux drops with distance as

$$\left|\vec{F}_{\rm rad}\right| = \frac{ac}{4} T_*^4 \times \left(\frac{R_*}{r}\right)^2, \tag{2.7}$$

if extinction is neglected. Then, the equilibrium gas temperature satisfies

$$T_{\rm eq} \times \left(\frac{\kappa_{\rm P}\left(T_{\rm eq}\right)}{\kappa_{\rm P}\left(T_{\rm eq}, T_*\right)}\right)^{1/4} = T_* \times \left(\frac{R_*}{2r}\right)^{1/2}. \tag{2.8}$$

For fixed $T_*$, $R_*$, and $r$, the right-hand side is a constant and the equilibrium temperature is defined by the ratio $\kappa_{\rm P}\left(T_{\rm gas}\right)/\kappa_{\rm P}\left(T_{\rm gas}, T_{\rm rad}\right)$. For a given density this ratio can vary with $T_{\rm gas}$ such that multiple solutions to Eq. (2.8) are possible. Figure 2.1 illustrates this sort of degeneracy. We consider

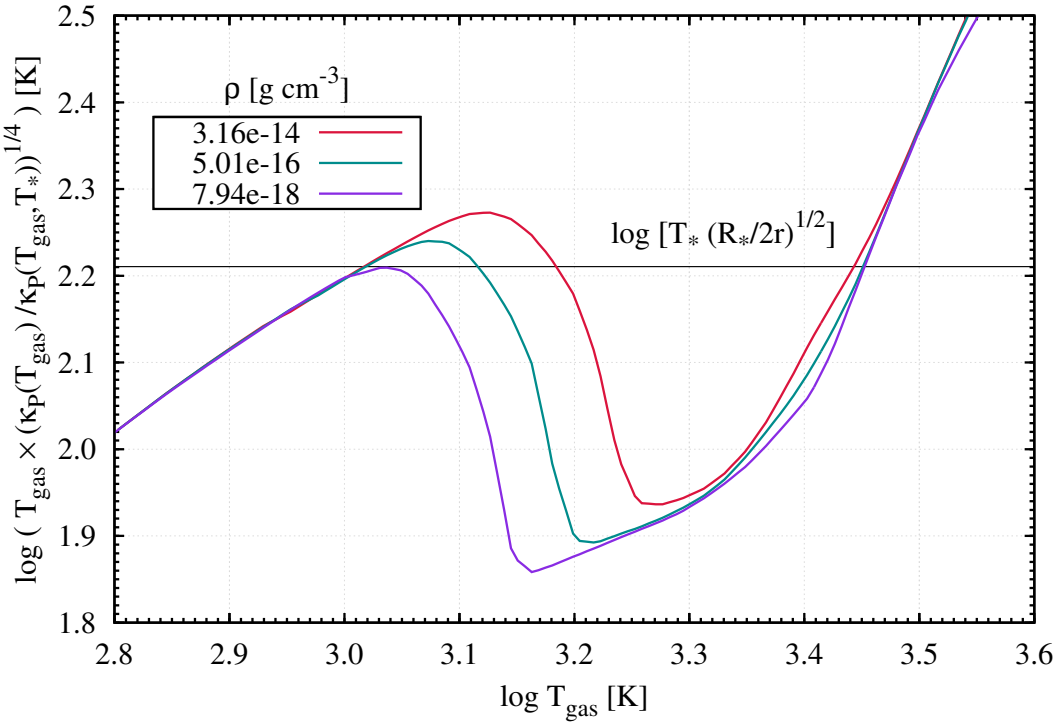


**Figure 2.1:** Equilibrium temperature degeneracy in an optically thin gas. The radiation source is a star with $T_* = 10^4$ K, $R_* = 1.7\,R_\odot$ at $r = 15$ AU. The temperatures at which the curves cross the dashed horizontal line are equilibrium temperatures. See text for more details.

a star with $T_* = 10^4$ K, $R_* = 1.7\,R_\odot$, choose three different densities at $r = 15$ AU ($3 \times 10^{-14}, 5 \times 10^{-16}, 8 \times 10^{-18}$ g cm$^{-3}$), and plot the left-hand side of Eq. (2.8) as a function of gas temperature. Temperatures at which the curves cross the dashed horizontal line, e.g. the right-hand side of Eq. (2.8), are equilibrium temperatures. As is seen in the plot, there are multiple solutions for densities above $\approx 8 \times 10^{-18}$ g cm$^{-3}$ and only a unique solution for lower densities. Getting closer to the star (shifting the dashed horizontal line upwards) would increase the value of this density threshold*.

In case of degeneracy, the first and the third solutions are stable, the second one is unstable. Stability is given for positive gradients: $\partial_{T_{gas}} \left( T_{\rm gas} \times \left( \varkappa_{\rm P} \left( T_{\rm gas} \right) / \varkappa_{\rm P} \left( T_{\rm gas}, T_{\rm rad} \right) \right)^{1/4} \right) > 0$. Near a stable equilibrium point, gas with temperature $T_{\rm gas} < T_{\rm eq}$ will be effectively heated up to the equilibrium temperature and vice versa: gas with temperature $T_{\rm gas} > T_{\rm eq}$ will be effectively cooled down to the

*At very low densities non-equilibrium chemistry may change the abundances of some species affecting the mean opacity as well. The degeneracy will only occur provided there is an inverse in the slope of the cooling (or heating) rate with respect to temperature.

equilibrium temperature. The opposite happens around an unstable equilibrium point: runaway heating or cooling brings the temperature apart from that value to the corresponding stable solution. This process is known as radiative instability.

## 2.3 Equilibrium gas temperature as a function of radiation temperature

We can illustrate the degeneracy in another complementary way. Namely, if we keep constant both the gas density and the geometric attenuation factor $(R_{\rm rad}/2r)^{1/2} = \mathcal{A}$, we get $T_{\rm eq}$ in dependence of $T_{\rm rad}$:

$$T_{\rm eq} = \mathcal{A} \times T_{\rm rad} \times \left( \frac{\kappa_{\rm P}\left(T_{\rm gas}, T_{\rm rad}\right)}{\kappa_{\rm P}\left(T_{\rm gas}\right)} \right)^{1/4} . \tag{2.9}$$

This equation has to be solved implicitly because $\kappa_{\rm P}\left(T_{\rm gas}, T_{\rm rad}\right)$ and $\kappa_{\rm P}$ are functions of $T_{\rm eq}$. We

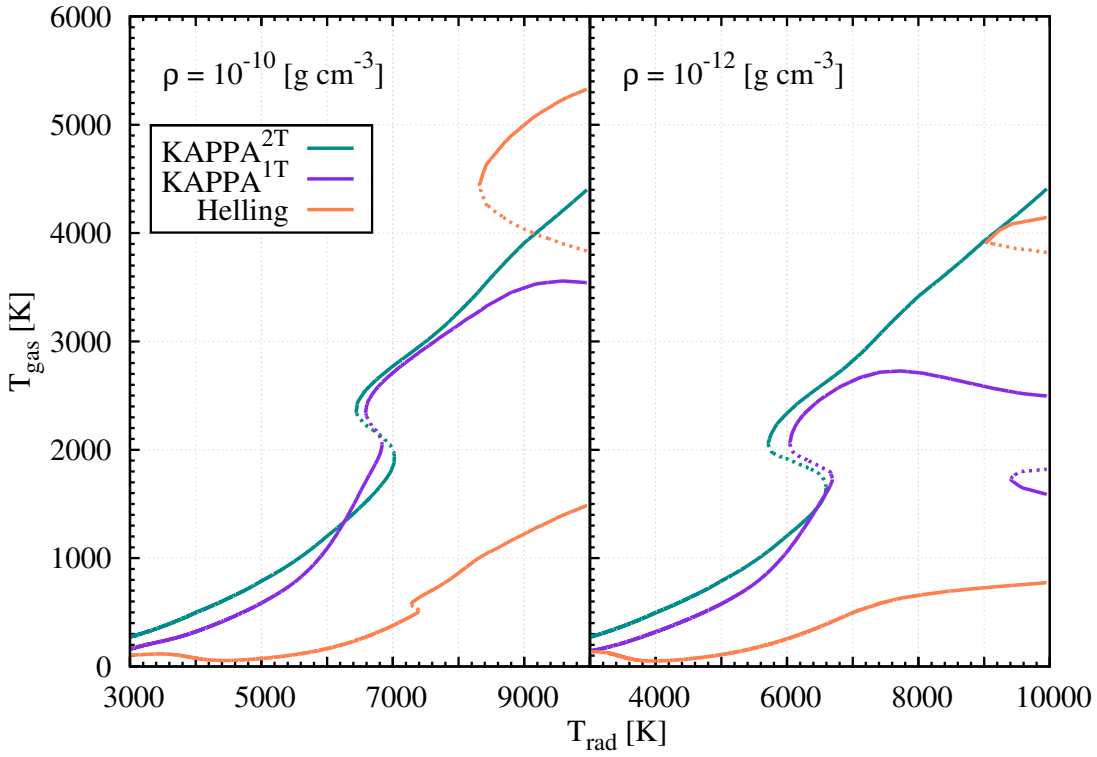


**Figure 2.2:** Equilibrium temperature degeneracy: optically thin gas temperature as a function of radiative temperature. The attenuation factor $6.3 \times 10^{-2}$ corresponds to $r/R_* \approx 127$. The *in situ* density is $10^{-10}$ g cm$^{-3}$ (*left panel*), and $10^{-12}$ g cm$^{-3}$ (*right panel*). Each curve corresponds to a different opacity data source: the thickest line – this work, using $\kappa_{\rm P}\left(T_{\rm gas}, T_{\rm rad}\right)$; the intermediate-thick line – this work, using $\kappa_{\rm P}\left(T_{\rm rad}\right)$ instead of $\kappa_{\rm P}\left(T_{\rm gas}, T_{\rm rad}\right)$; the thinnest line – Helling et al. [2000], using $\kappa_{\rm P}\left(T_{\rm rad}\right)$. The dashed parts of the lines mark unstable solutions (see text).

plot in Fig. 2.2 equilibrium gas temperature versus radiation temperature for different opacity data.

The attenuation factor $\mathcal{A} = 6.3 \times 10^{-2}$ corresponds to $r \approx 127 R_*$ ($r = 1$ AU for $R_* = 1.7$ R$_\odot$). Each panel corresponds to a different density. As can be seen, the degeneracy is not an exclusive feature of the new opacity data: it also appears when using opacity from Helling et al. [2000]. As soon as the unstable solutions appear between the stable ones, limit cycles in the temperature profile are possible if one considers time-dependent radiative transport.

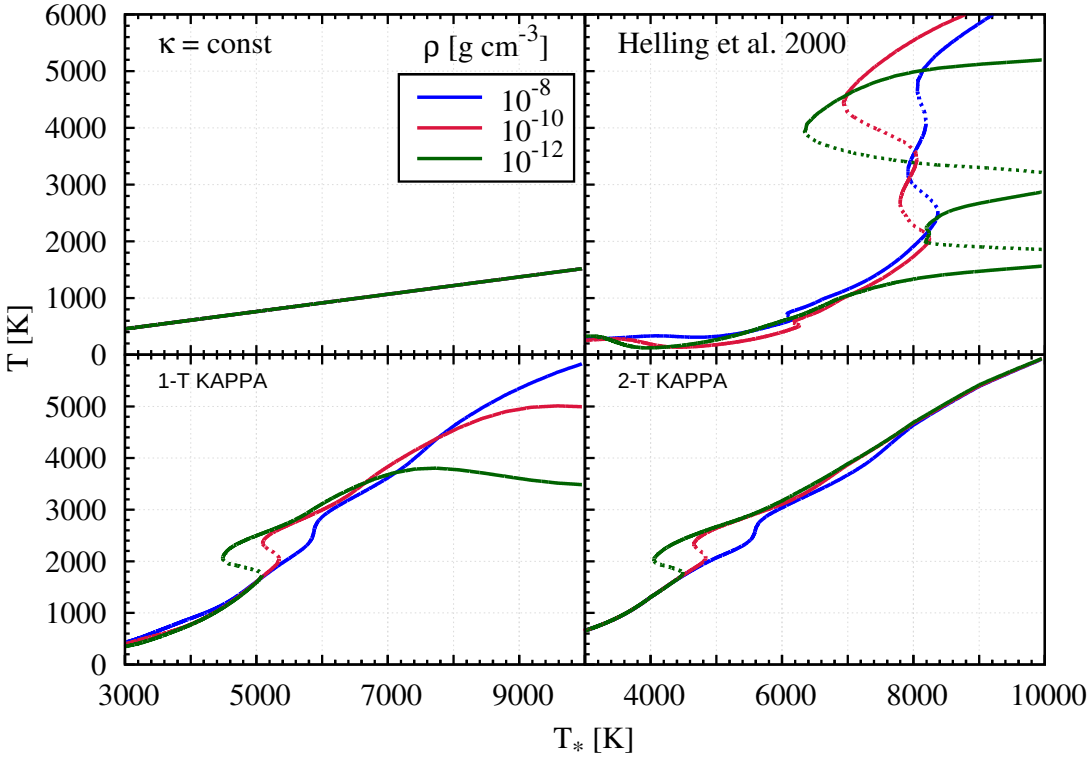


**Figure 2.3:** Same as Fig. 2.2 but with three *in situ* densities in one panel, each corresponding to different opacity model.

## 2.4 Discussion

Equilibrium atomic-gas temperature determinations employing elaborate statistical equilibrium calculations were performed for simplified cases: Weymann [1960] considered a compressible atomic gas under fixed heating rate in application to stellar chromospheres; Williams [1967] considered an incompressible atomic gas excited by ultraviolet synchrotron photons. Both studies revealed steep gradients in the equilibrium temperature profiles.

A detailed discussion of all the heating and cooling mechanisms in a gas mixture is beyond the scope and intention of this paper. We therefore refer the reader to the excellent work by Kamp & van

Zadelhoff [2001], where the authors considered dusty gas and additional gas heating from the photoelectrons extracted out of the dust particles.
To couple a calculation of a detailed ionisation and chemical equilibrium to a radiative hydrodynamics numerical modelling within a framework of global collapse would demand a great deal of computational time even with modern computational facilities, which is why we consider radiative equilibrium in terms of mean opacity. The frequency averaging is further justified by uncertainties and incompleteness of the present atomic and molecular data [e.g. Kurucz, 2002].
We highlight the impact this degeneracy has for the radiative transfer module described in Kuiper et al. [2010b]. The module includes an iterative temperature update scheme based on equation Eq. (16) in Kuiper et al. [2010b],

$$aT^4 = E_{\rm R} + \frac{\varkappa_{\rm P}(T_{\rm rad})}{\varkappa_{\rm P}(T_{\rm gas})}\frac{\left|\vec{F}_{\rm rad}\right|}{c}, \tag{2.10}$$

where $E_{\rm R}$ is the diffusive part of the radiation energy density, a term that dominates at high optical depths; the net radiation flux, $\left|\vec{F}_{\rm rad}\right|$, is evaluated at the point under consideration; and $c$ is the speed of light. In the case of gas, $\varkappa_{\rm P}\left(T_{\rm gas}, T_{\rm rad}\right)$ should be used instead of $\varkappa_{\rm P}(T_{\rm rad})$. In an optically thick medium, the local flux of radiation is dominated by its diffusive thermal part. The effective opaqueness to this radiation is expressed in terms of the Rosseland average (Eq. 1.5) and the radiative transfer equation for the net flux is treated in a flux-limited diffusion approach [Levermore & Pomraning, 1981]. Contrarily, in an optically thin region, the second irradiation term on the right-hand-side of Eq. (2.10) dominates over the $E_{\rm R}$. Then, $\left|\vec{F}_{\rm rad}\right|$ can be substituted by the flux from the outer source (a star), $\left|\vec{F}_{\rm rad}\right| = L_*/(4\pi r^2) = (R_*/2r)^2\sigma T_*^4$, which turns Eq. (2.10) into Eq. (2.8).
In the case of degeneracy, the iterative scheme is unsuited to finding a unique solution. To properly determine the gas temperature in optically thin parts, we propose taking into account its time-dependent evolution.

*Relaxation time is the time to let the steam off.*

Unknown author

# 3 Thermal Relaxation Time

Results of this chapter are being prepared for publication in Astronomy & Astrophysics.

## 3.1 Definition

Motion of the material in PPDs can be described by the equations of fluid dynamics. Even without considering magnetic effects, the equations allow for development of various instabilities, which have been shown to be of key importance in planet and star formation. Those instabilities induce perturbations in temperature of the gas and, thus, in the local radiation field. Linear development of the instabilities depend on the decay time of these perturbations.
To isolate the required time scale, we consider evolution of only the temperature (thermal and radiation energy densities, Appendix A.3) leaving off the changes in pressure and velocity field. [see Lyra, 2014, for an analytic justification in a particular case of vertically unstratified disc].
Linearisation of the energy evolution equation yields a dispersion relation, from which the characteristic decay time of a Fourier mode $\delta T_k = (T - T_\circ)_k$ can be found:

$$t_{\mathrm{relax},k} = \frac{|\delta T_k|}{|\delta \dot{T}_k|}. \tag{3.1}$$

Here $T$ is the perturbed temperature, $T_0$ the equilibrium temperature ($\dot{T}_0 = 0$) and $\delta\dot{T}$ designates the time derivative of the perturbation. In PPDs, of prime interest are those cases when the time evolution is supplied by means of radiative transport. Conduction operates at much longer (viscous) time scales, and convective heat transport needs an unstable disc as a prerequisite.
To estimate the radiative relaxation time, we resolve the underlying processes and calculate their characteristic times. The relevant processes differ depending on the optical thickness of the mode (optical thickness of matter encompassed within the spatial Fourier wavelength). We distinguish between optically thick and optically thin relaxation regimes with characteristic times $t_{\text{thick}}$ and $t_{\text{thin}}$, respectively. The whole relaxation process can not operate at times shorter than the longest amongst these two:

$$t_{\text{relax}} = \max\left(t_{\text{thick}}, t_{\text{thin}}\right). \tag{3.2}$$

Below we introduce the constituent times.

## 3.2 Optically thin relaxation regime

The radiative material in PPDs is a dust-gas mixture. The bulk of the thermal energy is stored in the gas due to its dominating mass fraction:

$$\frac{\varrho_{\text{gas}}}{\varrho_{\text{dust}}} = \eta^{-1} \sim 10^2. \tag{3.3}$$

However, the dust emissivity, as measured by the Planck mean in LTE, is comparable or exceeds that of the gas at low temperatures. The radiative efficiency is expressible in terms of a time scale (see Appendix B.1)

$$t_{\text{emit}}^{\text{d/g}} = \frac{C_{\text{V}}}{16\kappa_{\text{P}}^{\text{d/g}}\sigma T^3} \tag{3.4}$$

with $\sigma$ being the Stefan-Boltzmann constant, $\kappa_{\text{P}}^{\text{d/g}}$ the Planck mean of the dust (per unit gas mass) or the gas, respectively. Time scales (3.4) do not depend on the perturbation wavelength, because evaluate the in situ emission rates. The dependence on density is only through the Planck mean and therefore is weak. Important scaling relation in terms of local angular frequency $\Omega$ is

$$\Omega t_{\text{emit}} \propto \Omega T^{-3}\kappa_{\text{P}}^{-1}. \tag{3.5}$$

The optically thin emission time as given by Eq. (3.4) is the shortest achievable relaxation time for the given material because implies the maximum (LTE) emissivity.
Though at low temperatures one has $\kappa_{\text{P}}^{\text{d}} > \kappa_{\text{P}}^{\text{g}}$, at higher temperatures in the range $650 < T < 1\,300$ K, the two means compare [Malygin et al., 2014; Semenov et al., 2003] meaning

that the gas is equally important in the relaxation by thermal emission. This holds valid under assumption of no severe depletion of gas-phase emitters due to freeze out. In such regions, the bulk of thermal energy of the gas is stored in the kinetic energy of the most abundant, 'non-radiating'* $H_2$ molecules. Prior to releasing the thermal energy in form of radiation, the thermal carriers transfer it via collisions to the species that can efficiently emit. Collision time $t_{\rm coll} = (n\sigma v)^{-1}$ limits the net relaxation if it is longer than the corresponding emission time (see Appendix B.2)

$$t_{\rm relax}^{\rm d/g} = \max\left(t_{\rm emit}^{\rm d/g}, t_{\rm coll}^{\rm d/g}\right). \tag{3.6}$$

There are two 'channels' of emission: the more efficient emitter with slower coupling (dust), and the less efficient emitter with faster coupling (gas). Gas equilibrates on much shorter times than the dust due to significantly larger number density $n$. However, the radiative time (3.4) for gas can be longer than the thermal equilibration time $t_{\rm coll}^{d}$ for dust, in which case the dust will thermalise and emit the perturbation excess. Because in linear approximation (small perturbations) thermal capacity of neither emitting material is exhausted, the one with the most efficient one determines the relaxation:

$$t_{\rm thin} = \min\left(t_{\rm relax}^{\rm d}, t_{\rm relax}^{g}\right). \tag{3.7}$$

In the so-called molecular layer above the midplane one has to take into account such dust-gas interactions as photoelectric heating, mutual irradiation, photochemistry, etc [Kamp & van Zadelhoff, 2001]. The collision time rather draws a border of validity to the assumptions made (LTE, equilibrium chemistry) than it estimates the relaxation time itself.

## 3.3 Optically thick relaxation regime

A perturbation with wavelength exceeding diffusion length scale

$$l_{\rm diff} = \frac{1}{\varkappa_{\rm R}\varrho} \tag{3.8}$$

can not relax as fast as on the local thermal emission time because the thermal photons get absorbed and re-emitted before escaping the perturbed medium. The excess thermal radiation effectively propagates in a diffusive manner over $\lambda = 2\pi k^{-1}$ with an effective opacity $\varkappa_{\rm R}$. Relaxation time of the mode becomes the corresponding diffusion time (see Appendix A)

$$t_{\rm thick} = \frac{1}{\tilde{D}k^2} \propto \tau_{\rm R}\lambda\varrho T^{-3}. \tag{3.9}$$

*meaning relative to other emitters under disc conditions. A permanent dipole moment of less abundant HD isotopologue, though, permits detection [Bergin et al., 2013]

Here $\tilde{D}$ is the effective diffusion coefficient (A.15) and

$$\tau_{\mathrm{R}} = \int_{-\lambda/2}^{+\lambda/2} \varkappa_{\mathrm{R}} \varrho \, dx. \tag{3.10}$$

the Rosseland thickness of the perturbation. One expects the optically thick time to measure the relaxation time (3.2) given the medium encompassed within the perturbation wavelength is optically thick, $\tau_{\mathrm{R}} > 1$ (see Fig. 3.3).
For modes $\lambda = \mathrm{H}$, it follows

$$\Omega t_{\mathrm{thick}} \approx \frac{3}{(2\pi)^2} f^{-1} \frac{c_{\mathrm{s}}}{c} \tau_{\mathrm{R}} \tag{3.11}$$

with factor $f^{-1} = (1 + \varrho C_{\mathrm{v}}/4aT^3) \approx \varrho C_{\mathrm{v}}/(4aT^3)$ being approximately the ratio of thermal to radiation energy densities.

## 3.4 Set-up

### 3.4.1 Density model

We adopt an axisymmetrical density structure from Dzyurkevich et al. [2013] to allow comparison with the studies considering the location of the magnetically dead zone. The central source is a solar-like star with $\mathcal{M}_* = 1\mathcal{M}_\odot$. The disc has a surface density profile

$$\Sigma = \Sigma_{\mathrm{c}} \left(\frac{R}{R_{\mathrm{c}}}\right)^{-p} \exp\left[-\left(\frac{R}{R_{\mathrm{c}}}\right)^{2-p}\right] \tag{3.12}$$

with $\Sigma_{\mathrm{c}}$ being the surface density at the cutoff radius $R_{\mathrm{c}}$:

$$\Sigma_{\mathrm{c}} = (2-p)\frac{\mathcal{M}_{\mathrm{disc}}}{2\pi R_{\mathrm{c}}^2}. \tag{3.13}$$

The surface density is normalized to $\Sigma = 1700$ g cm$^{-2}$ at 1 AU. Index $p$ of 0.9 and the cut-off radius of 40 AU is chosen following Andrews et al. [2009] to match the minimum-mass solar nebula at 1 and 100 AU. $\mathcal{M}_{\mathrm{disc}}$ is the total mass of the disc. The volumetric density is readily unfolded for a vertically isothermal case

$$\varrho = \frac{\Sigma}{\sqrt{2\pi}H} \exp\left(\frac{-z^2}{2H^2}\right), \tag{3.14}$$

where $H$ is the local pressure scale height.

### 3.4.2 Temperature model

We adopt a vertically isothermal radially stratified temperature profile following Dzyurkevich et al. [2013]

$$T = T_0 \left( \frac{R_{\rm in}}{R} \right)^{1/2}, \tag{3.15}$$

with $T_0 = 280$ K at $R_{\rm in} = 1$ AU. A lower limit of 10 K stops the power law decrease at $\sim 250$ AU. The profiles of surface density, volumetric density, and the midplane temperature are given in Fig. 3.1. The highest value of $\mathcal{M}_{\rm disc} = 0.1\mathcal{M}_\odot$ considered for this model assures the configuration is stable against self-fragmentation, according to the Toomre $Q$-criterion.

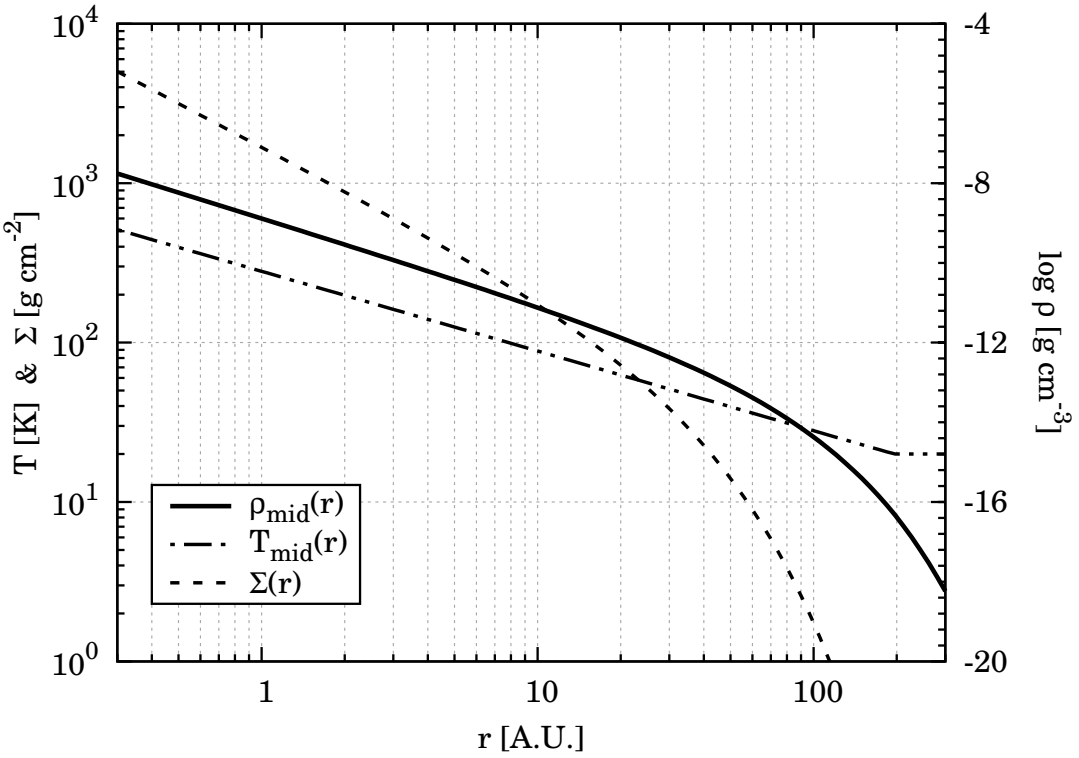


**Figure 3.1:** Disc structure as adopted from Dzyurkevich et al. [2013]. Surface density profile (dashed): power law with exponential roll-off; temperature profile: power law bounded from below (dot-dot-dashed). The corresponding volumetric density in the midplane is plotted with solid line (the values at the right ordinate).

### 3.4.3 Opacities

We utilise tabulated dust and gas mean opacities (Fig. 3.2). Rosseland and Planck means of iron-poor homogeneous spheres from Semenov et al. [2003] we complement with corresponding gas means from Malygin et al. [2014, see Figs. 3.2a,c]. Gas chemistry and opacity in outer disc regions is poorly

constrained observationally and experimentally [see Dutrey et al., 2014, and references therein]. For our dust-depleted models we consider two cases of pure gas opacity: (i) data from Malygin et al. [2014] with a low-temperature cut of 650 K, and (ii) data complemented with scaled-down (in density) atmospheric opacities from Freedman et al. [2008] with the lowest temperature of 75 K (see Figs. 3.2b,d). For yet lower temperatures the last value is always used. Data from Freedman et al. [2008] accounts for the settling of condensates in a gravitational field (e.g. in a cool dwarf) but not for the freeze out on grain surfaces – they are not applicable for circumstellar discs, if only by a coincidence. Thus, we will consider two gas opacity models: the one with higher opacity around $2.5 \times 10^2$ K, but a substantial decrease below $\approx 120$ K (we will refer to this as the small gas opacity case); and the one with constant high opacity ($\varkappa_P \approx 3.5 \mathrm{cm}^2\mathrm{g}^{-1}$) below 650 K (the large gas opacity case). The two models can be treated as a rough scan of the poorly-constrained parameter space. In

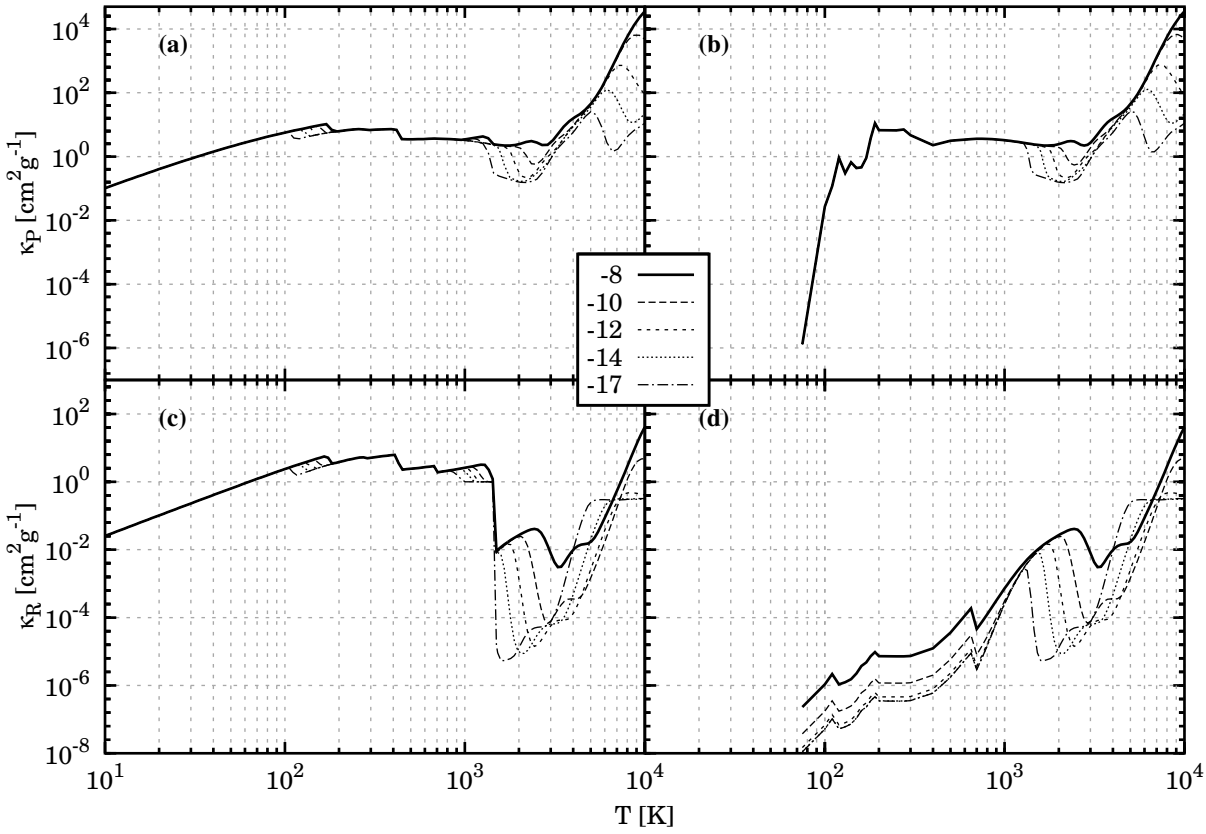


**Figure 3.2:** Planck (*top row*) and Rosseland (*bottom row*) mean opacities. Joint dust [Semenov et al., 2003, homogenous IPS] and gas [Malygin et al., 2014] opacities are on panels (a) and (c). Panels (b) and (d) present pure gas opacity (see text). The numbers on the legend indicate the logarithm base ten of the density in cgs units.

calculations of the optically thick relaxation time, we join the Rosseland opacities by direct

summation of the corresponding means. In case of reduction the dust-to-gas mass ratio (Sect. 3.5.5), we modify the dust opacity by

$$\varkappa^{\mathrm{d}} = \frac{\eta'}{\eta}\varkappa^{\mathrm{d}}, \tag{3.16}$$

where $\eta'$ is the desired dust-to-gas mass ratio and $\eta = 0.014$ the nominal dust-to-gas mass ratio for which the dust opacity tables were calculated [see Table 1 in Semenov et al., 2003, case of IPS]. The gas opacity stays unchanged.

## 3.5 Results

In this section the values for the relaxation rate are dimensionless numbers $\Omega t$, with $\Omega$ being the local angular (Keplerian) frequency. The radiative diffusion time is calculated for vertical direction, $\lambda = \lambda_z$ when not explicitly stated, and $\lambda$ is measured in local pressure scale heights H. The underlying disc model is the isothermal with radial stratification as described in Sect. 3.4 except for Sect. 4.2. The default gas opacity model is the one complemented with the low-temperature data from Freedman et al. [2008] (the small gas opacity model). Our method does not quantitatively constrain the relaxation time in the collisionally decoupled regions, but one would naively expect the relaxation there to be slower than that provided by LTE emission.

### 3.5.1 Relaxation regimes: recipe verification

Figure 3.3 represents a verification of the introduced in Sect. 3.1 maximum-time criterion. In opaque inner disc even the high-frequency modes are optically thick and relax on radiative diffusion times (cf. the light-grey areas in Figs. 3.3a-d). Farther out and close to the midplane, there are the regions of the optically thin relaxation via thermal emission (the white areas in Figs. 3.3a-d). Low-frequency modes $\lambda/\mathrm{H} \approx 1$ become optically thin in upper layers when the relaxation is limited by collision time between dust and gas particles, so the regions of the relaxation via thermal emission are absent up to 40 AU for such modes. As the perturbation frequency increases, the zone of the fastest optically thin relaxation gets larger and wraps around the region of the optically thick relaxation. The cross-hatched pattern depicts the zone of the dust collisional decoupling, $t^{\mathrm{d}}_{\mathrm{coll}} > t^{\mathrm{d}}_{\mathrm{emit}}$, and the dark-grey area – of the gas collisional decoupling, $t^{g}_{\mathrm{coll}} > t^{g}_{\mathrm{emit}}$. A proper estimate of thermal relaxation time there would demand inclusion of the photoelectric heating and other non-thermal processes [e.g. Kamp & van Zadelhoff, 2001]. In calculations of the stellar light absorption in case of the large gas opacity model, the two-temperature Planck mean was used: $\tilde{\tau}^{*}_{\mathrm{P}} = \int \varkappa^{g}_{\mathrm{P}}\left(T_{*}, T_{\mathrm{g}}\right)\varrho dR$ (the integration is along the ray of constant polar angle in spherical coordinates).
The transition between the two relaxation regimes happens closer to the star and the midplane with increase in the wavenumber. A relevant measure for distinguishing between the two regimes of

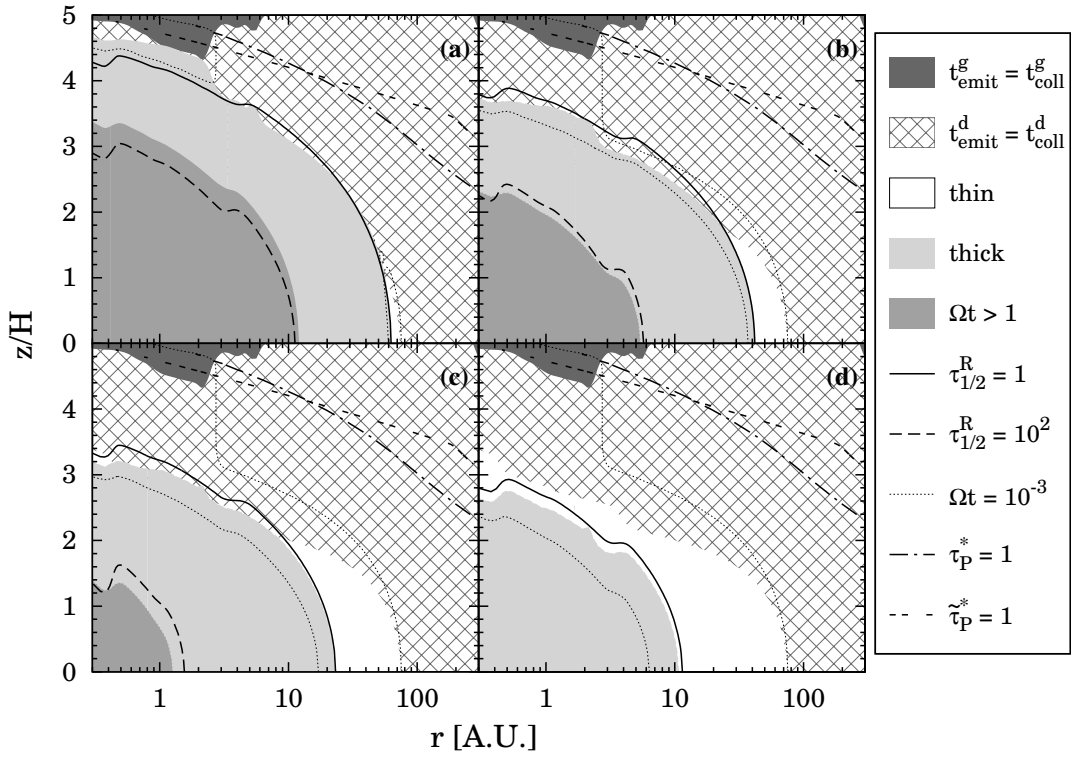


**Figure 3.3:** Recipe verification. The four panels are different perturbation wavelengths $\lambda/H$: (a) 2, (b) 0.5, (c) 0.1, and (d) 0.02. The cross-hatched pattern identifies regions of dust collisional decoupling; the white areas – of the optically thin LTE relaxation; the light-grey – of the optically thick relaxation. The dark-grey additionally highlights the dynamically slow optically thick relaxation ($\Omega t > 1$). Rosseland depth $\tau_{R,1/2} = 1$ (solid line) traces the transition to the optically thick regime, which gets dynamically slow only at $\tau_{R,1/2} \approx 10^2$ (long-dashed line). The contour line of $\Omega t = 10^{-3}$ is plotted with dotted line, the absorption of stellar light – with dot-dashed line (the small gas opacity) and double-dashed line (the large gas opacity).

relaxation is the Rosseland thickness over the region of the same sign of the perturbation amplitude (i.e., from peak to noughts)

$$\tau_{R,1/2} = \int_{-\lambda/4}^{+\lambda/4} \varkappa_R \varrho \, dx. \tag{3.17}$$

Figure 3.3 demonstrates the two regimes of relaxation transiting into each other at optical depths $\tau_{R,1/2} \approx 1$ (the solid line in Fig. 3.3a). The maximum time criterion (3.2) decides about the transition without explicitly demanding a certain optical depth or a diffusion length. By equating (3.9) and (3.7) while letting $\lambda = l_{\rm diff}$, one can show the optical depths at the transition indeed

$$\tau_R = \frac{(2\pi)^2}{3} \frac{\langle \varkappa_R \rangle}{\varkappa_P}. \tag{3.18}$$

This is of order unity for dust opacity, though smaller for pure gas, where the transition, thus, trace

lower Rosseland depths. Dynamically slow relaxation ($\Omega t \geq 1$, the dark-grey areas in Fig/ 3.3) stars at around $\tau_R = 10^2$ (the long-dashed line). For midplane perturbations with $\lambda/H = 2$ this corresponds to $\approx 10$ AU. The optically thick relaxation, hence, is not a synonym for the dynamically slow relaxation: optically thick modes can be either adiabatic or almost isothermal. In contrast, the optically thin relaxation in LTE yields $\Omega t \sim 10^{-4} - 10^{-3}$ regardless of the perturbation wavelength but only dependent on the location in the disc. The midplane perturbation wavelengths up to $\lambda/H = 2$ are isothermal at $60 - 80$ AU, but smaller ones can be isothermal in much larger volumes of the disc (see white areas in different panels of Fig. 3.3).

### 3.5.2 Constituent times

A comparison between the constituent times through the midplane is plotted in Fig. 3.4 for the two opacity models. Figure 3.4a corresponds to the fiducial case of small gas opacity at low temperature [data from Freedman et al., 2008]. Figure 3.4b shows the case of large gas opacity at low temperature [last point extrapolation from Malygin et al., 2014]. The optically thick relaxation is dominated by dust and is not sensitive to the gas model. The three solid lines on both panels show the optically thick time depending on the perturbation wavelength (see Sect. 3.5.3). The thermal emission time and the collision time are both evaluated locally, at the peak of the perturbation, and do not depend on the perturbation wavelength. The optically thin relaxation (the long-dashed line in Fig. 3.4) is sensitive to the gas emissivity: due to fast collisional coupling (the grey dotted lines in Fig. 3.4), gas becomes the dominant coolant in high emissivity model (Fig. 3.4b), but not in the low emissivity model (Fig. 3.4a). Beyond $\approx 60$ AU, the dust does not thermalise within it's own radiation time (3.4), so the dust relaxation gets collisionally limited (the black dotted lines cross the black dash-dotted lines in Fig. 3.4). This also restricts the net relaxation in the outer disc in the small gas opacity scenario (Fig. 3.4a). In this case, the optically thin gas relaxation being constrained by the weak emissivity of the gas (see the grey dot-dashed line in Fig. 3.4a), never gets into play due to much more efficient dust radiation (recall Eq. 3.7). In the large gas opacity case, the relaxation gets restrained by gas-to-gas collisions beyond $\approx 120$ AU (see the grey dotted line crossing the grey dot-dashed line in Fig. 3.4b).

High-frequency midplane modes with $\lambda/H = 10^{-2}$ (and smaller) all relax dynamically fast regardless of their optical depth (see the light-grey solid lines in Fig. 3.4). Low-frequency midplane modes $\lambda/H = 1$ (the black solid lines in Fig. 3.4) relax dynamically slow within first $\approx$ AU, next the relaxation rate drops down to $\approx 10^{-3}$ at $\approx 50$ AU while the optical depth still exceeding unity. The diffusion time drops below the thermal emission time because the flux-limited diffusion formalism used in calculations of the optically thick relaxation does not account for the finite time of the intrinsic radiative processes but only for the propagation of the energy density over the perturbation wavelength (see Sect. 3.6.2).

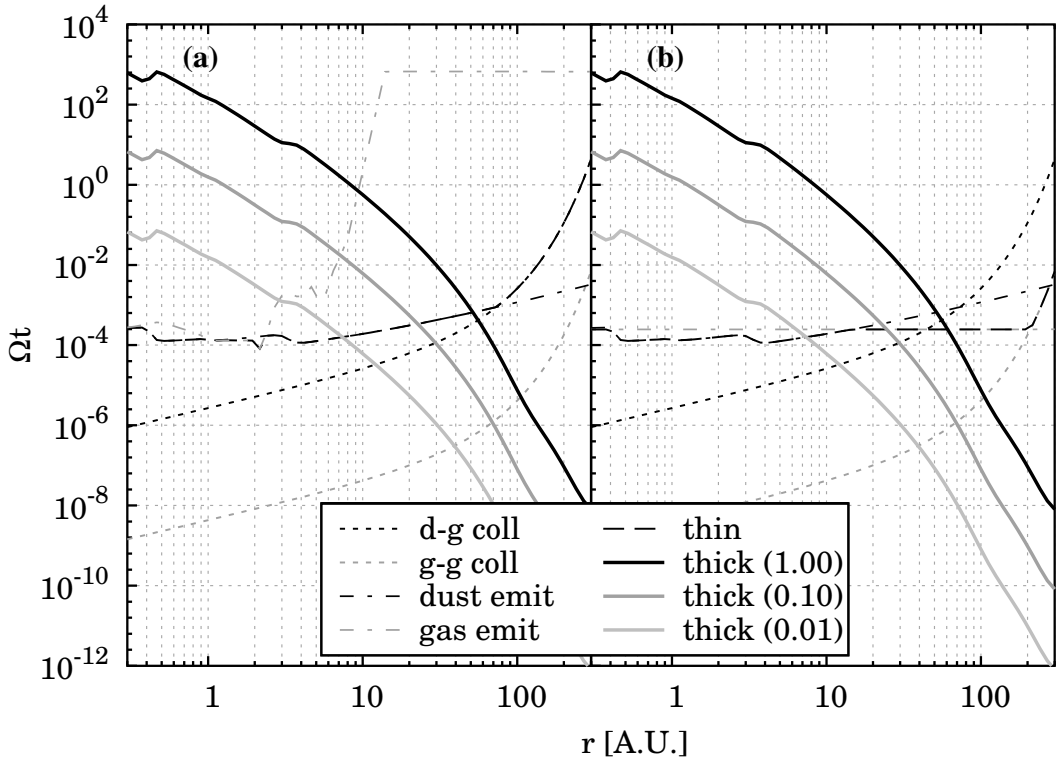


**Figure 3.4:** Comparison between the three constituents of the relaxation time. Vertical modes in the disc midplane. The optically thick (solid lines), the optically thin (long dashed), and the coupling times (short dashed and dot-dashed). The values in the brackets in the legend indicate $\lambda_z/\mathrm{H}$ – the ratio of the perturbation wavelength to the *local* pressure scale height. Panel (a): the small gas opacity model, panel (b): the large gas opacity model.

Figure 3.5 displays the maps of the ingredient times for $\lambda/\mathrm{H} = 2$. The optically thick relaxation time (Fig. 3.5a) increases towards the star and the midplane as the perturbation gets optically thicker. On the map of the optically thin relaxation time (Fig. 3.5b) the bending lines are occasionally interrupted by vertical contours. These are stemming from collision (B.6) and emission (3.4) times. Figure 3.5c shows the dust thermalisation rate via collisions, and Fig. 3.5d maps the dust emission rate. The assumed vertically uniform radially stratified temperature structure is distinctly captured in the latter. A wedge-like dark grey structure at around 3 AU is due to changes in the Planck mean opacity near the water ice line. The size distribution of the grains (see Appendix B.2) as well as the dust-to-gas mass ratio are uniform over the disc interiors, so Fig. 3.5c is up to a scaling an evaluation of $\Omega n_{\mathrm{d}}^{-1} T^{-1/2}$.

### 3.5.3 Perturbation wavelength

At a given moment of time, the density, temperature and opacities are defined at any point in the disc. Then the regime of radiative relaxation – optically thick or thin – is decided by the

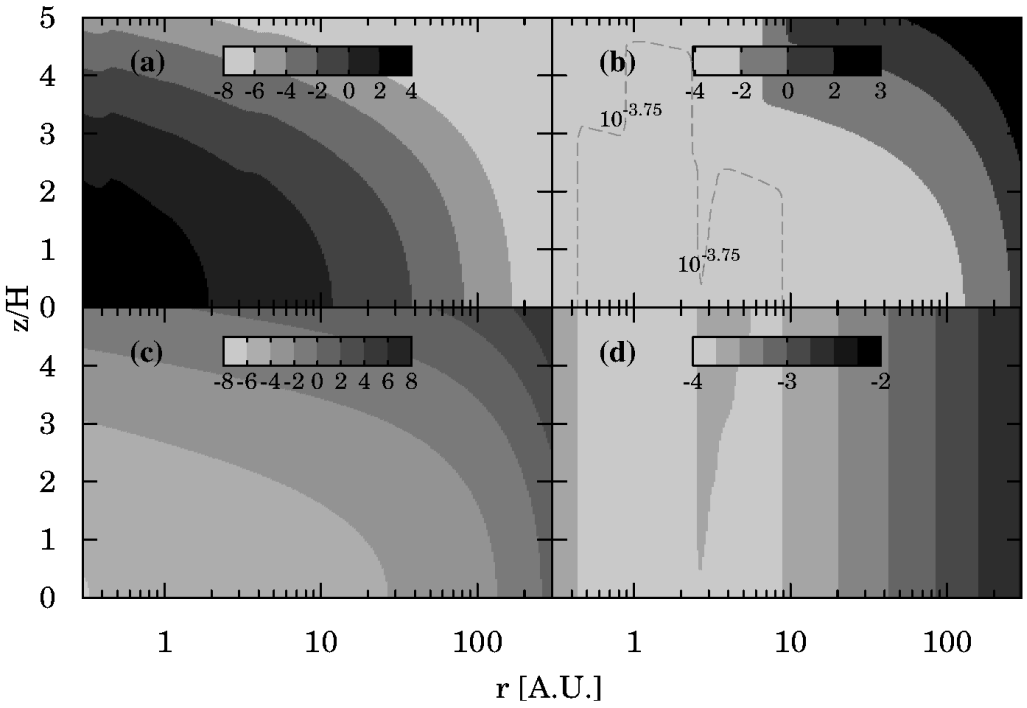


**Figure 3.5:** Maps of ingredient relaxation times for vertical perturbations with $\lambda = 2H$. Plotted in colour are the values of $\log(\Omega t)$ fo (a) the thick relaxation, (b) the thin relaxation, (c) the dust collision time, and (d) the dust emission time.

perturbation wavelength. Figure 3.6 shows relaxation rates as a function of $\lambda$ at different radial locations. Thermal emission relaxation puts a bottom wavelength-independent limit on relaxation time (short-dashed lines). In the optically thick regime, the dependence itself changes with $\lambda$. For modes $\lambda/H \leqslant 1$, relaxation time $t_{\rm thick} \propto \tau_R \lambda \propto \lambda^2$ (if the perturbation does not encompass the ice line). For longer wavelengths, $\lambda/H > 1$, the Rosseland depth of the mode saturates (see the dotted lines in Fig. 3.6) because of the exponential decline of density in vertical direction. In this limit $t_{\rm thick} \propto \lambda$. Long-wavelength modes $\lambda > 3H$ relax inhomogeneously: in the atmospheric layers due to collisional decoupling, the relaxation can become as slow as the radiative diffusion from the midplane.

The optically thin modes all relax dynamically fast (i.e., $\Omega t \ll 1$, see Figs. 3.6b-d), but the optically thick modes can relax both quasi-isothermally and adiabatically. Indeed, high-frequency modes $\lambda/H \ll 10^{-1}$ always relax isothermally even if they are optically thick (Fig. 3.6a). A transition between the thick and the thin regimes happens at successively growing $\lambda/H$ such that the total depth of the mode $\tau_R \sim 2$ at the transition (see Sect. 3.5.1).

Figure 3.7 shows relaxation time maps for different perturbation wavelengths: longer to shorter from left top to bottom right. As discussed above, a change in the wavelength alters only the optically

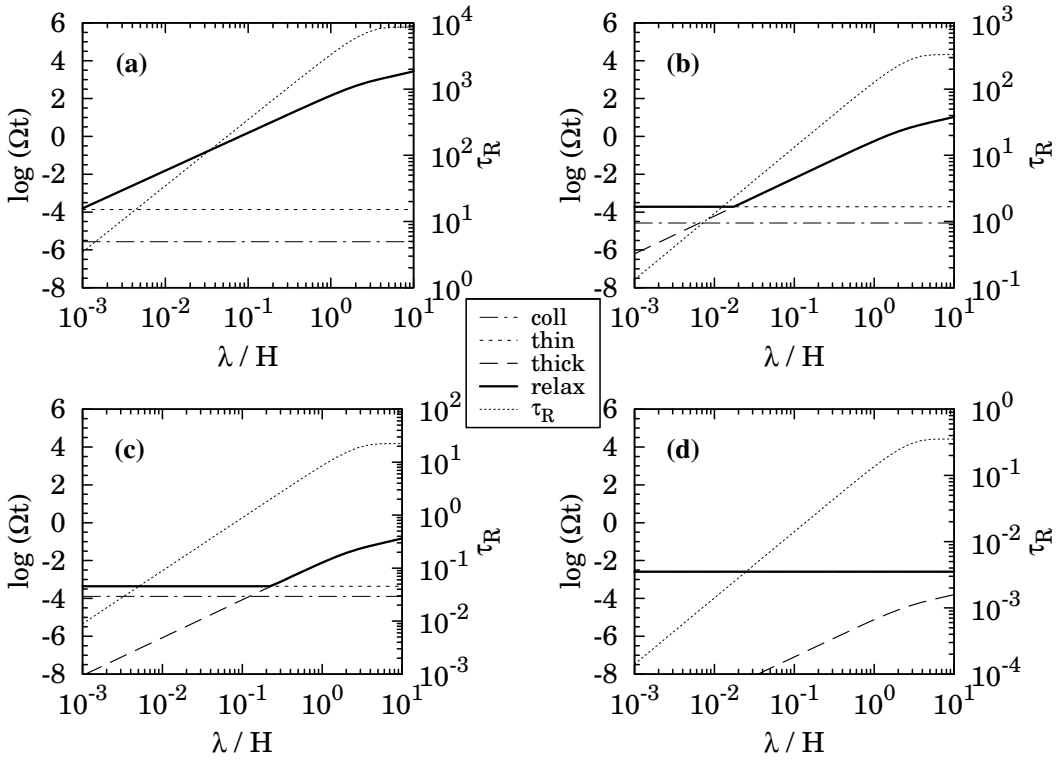


**Figure 3.6:** Relaxation time versus wavelength $\lambda = \lambda_z$ of vertical midplane modes at different radial separations from the star: 1 AU **(a)**, 10 AU **(b)**, 30 AU **(c)**, and 100 AU **(d)**. In each panel, the relaxation time itself is in thick solid. The short dashed line marks the optically thin, the long dashed – the optically thick relaxation time. Dust collision time is drawn with dot-dashed. The dotted line shows Rosseland thickness of the mode (the values being on the right ordinate).

thick modes. The pattern in left bottom area in Fig. 3.7a-d shrinks with decreasing $\lambda$. The rest of the pattern being underlain by the optically thin relaxation regime stays unaltered. The line contours of the optically thick relaxation time follow approximately the iso-contours of the Rosseland depth (see Sect. 3.5.1) capturing the jumps in opacity near the water ice line ($\approx$ 3 AU) and volatile organics evaporation line ($\approx$ 0.5 AU). In the optically thin relaxation regime, the opacity features show up in the thermal emission component (see Fig. 3.5d).

Dynamically fast relaxation (the light grey areas in Fig. 3.7) operates in a certain disc domain, which is sandwiched between the regions of slower relaxation and is wider for higher-frequency modes. This quasi isothermal relaxation is attainable for different modes in both midplane and superficial layers of the disc. The values of the relaxation rate themselves in the collisionally decoupled regions are uncertain due to the model limitations. Still, the qualitative increase of the relaxation time with the drop of density is robust: the fastest radiative relaxation rates are achievable only in LTE, which can not be established on times shorter than the thermal emission time in low-density regions. The radiative relaxation alone suggests existence of long-lasting perturbations in gas and dust

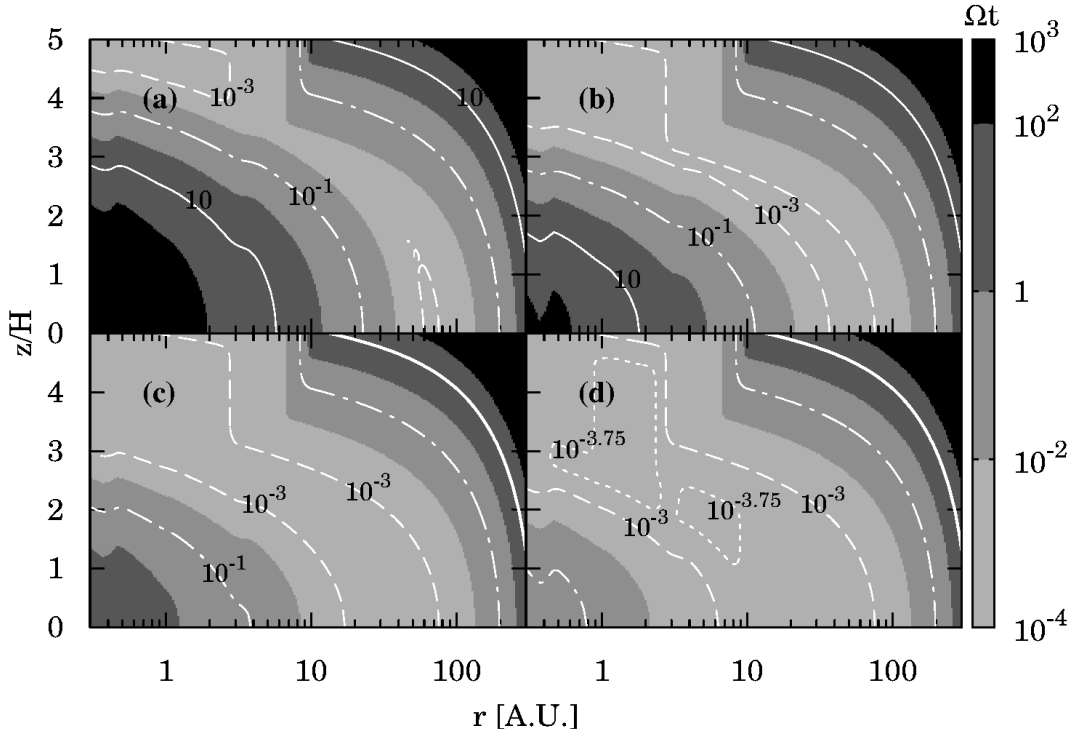


**Figure 3.7:** Thermal relaxation time map for different perturbation wavelengths: 2H **(a)**, 0.5H **(b)**, 0.1H **(c)**, and 0.02H **(d)**.

temperatures in atmospheric layers of the disc. The dynamics – not considered here – can influence their evolution on such long dynamic times.

### 3.5.4 Radial and vertical modes

The optically thin relaxation time is calculated locally, but the optically thick regime is essentially non-local as the photons diffuse through the perturbed medium (see Sect. 3.6.4). The times to diffuse in different directions are, in general, different. In Fig. 3.8, the relaxation times of radial and vertical perturbations of the same wavelengths $\lambda_r = \lambda_z$ is shown as a function of vertical coordinate $z$ at different radial locations. Above the midplane, the diffusion time over the same spatial extend is shorter in radial direction, but in the midplane the vertical and radial diffusion times are comparable. Close to the midplane, the vertical diffusion time over the pressure scale height gets shorter than the corresponding radial diffusion time (see the black dot-dashed lines crossing the black solid lines at $0 < z/\mathrm{H} < 1$ in Fig. 3.8). The difference vanishes for short wavelengths because the perturbations become more local (see also Fig.3.9). At larger radial separations, a transition to the optically thin relaxation regime occurs closer to the midplane, and at 100 AU, all the considered wavelengths are

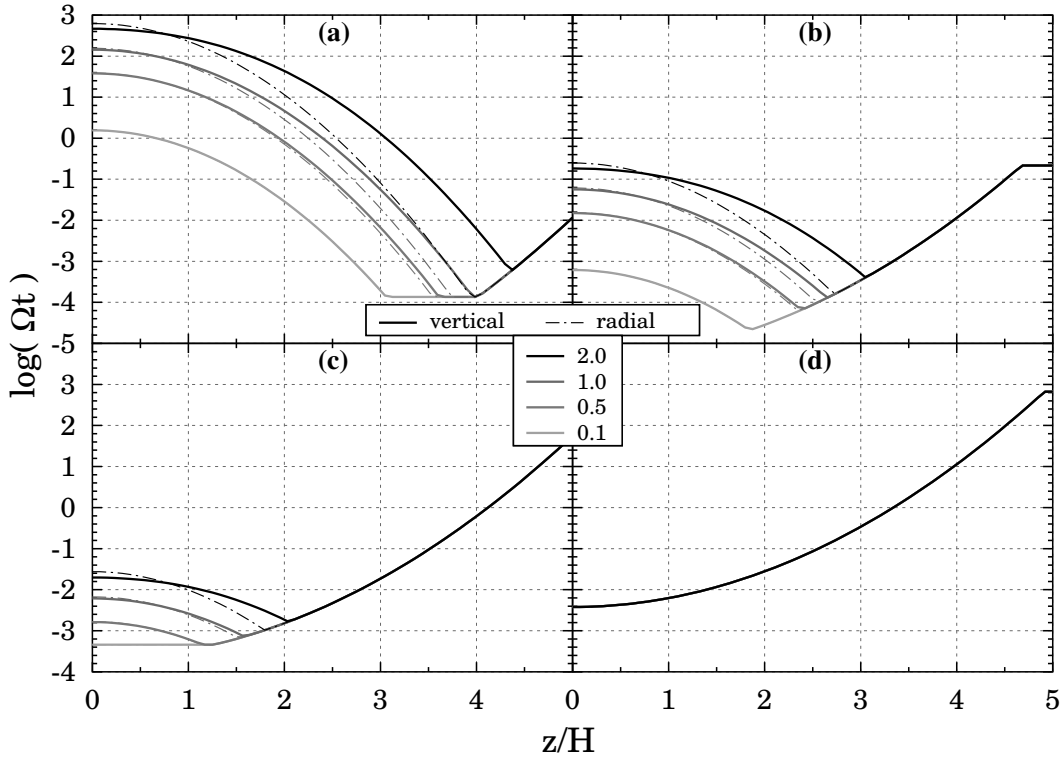


**Figure 3.8:** Vertical and radial relaxation time ($y$-axis) versus height above the midplane ($x$-axis). Each panel corresponds to a given radial separation: (a) 1 AU, (b) 10 AU, (c) 33 AU, and (d) 100 AU. The grey to black colours mark different perturbation wavelengths $\lambda/H$.

optically thin.

A relative difference between vertical and radial relaxation times is mapped in Fig. 3.9. As pointed out above, this is larger for long-wavelength modes. The relative difference is the largest when both $\lambda_z$ and $\lambda_r$ are optically thick but have different optical depths. A difference in vertical and radial density stratification (a Gaussian wing versus a power-law) is what mainly makes this up. For $\lambda/H = 2$, the maximum difference of $\approx 100\%$ is at around 3.7H at radial separations closer than 30 AU (cf. Figs. 3.8a,3.9a). At radial locations beyond $\sim$ 40 AU, both vertical and radial modes become optically thin at all heights, $t_z - t_r = 0$ (the grey background in Figs. 3.9a,b). Close to the midplane, the difference in the optical depths makes the 'vertical' relaxation up to 60% faster. The overall pattern is similar for smaller wavelengths but the absolute scale drops. The maximum difference is $\approx 1\%$ for $\lambda/H = 0.1$ and $\approx 0.5\%$ for $\lambda/H = 0.02$. This means that the relaxation time calculated with the vertical diffusion can be successfully applied in an analysis of the high-frequency modes of the vertical shear instability (see Fig. 4.1).

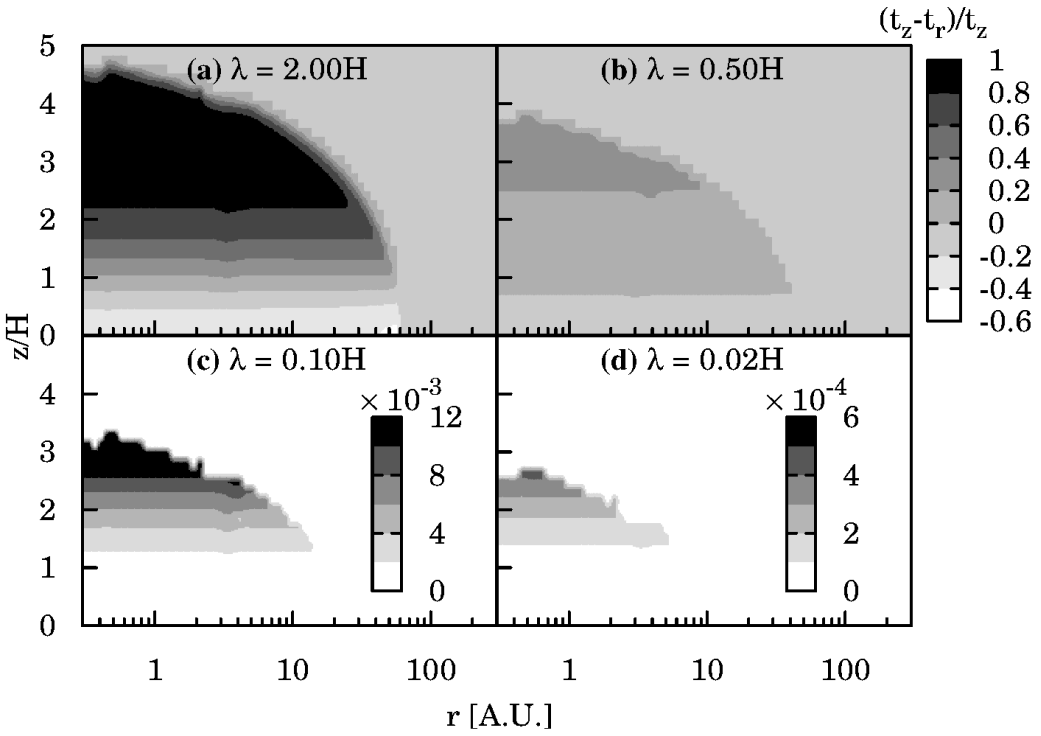


**Figure 3.9:** Relative difference between vertical and radial relaxation times, $(t_z - t_r)/t_z$. Each panel corresponds to a single wavelength $\lambda_z = \lambda_r$ as labelled. The box on the top right sets the colour scale for the two top panels, for the two bottom panels the colour scale is inside each.

### 3.5.5 Dust-to-gas mass ratio

Klahr & Lin [2015] argue that the dust growth during planet formation leads dust opacity decrease by a factor of $10 - 10^2$. Luminous accretion shocks around young planets [Sallum et al., 2015] can contribute via photoevaporation. In this section we scan the parameter space by homogeneously reducing the dust amount while leaving the effective collision cross section (the distribution) unchanged.

The optically thick relaxation (3.9) is dominated by dust because of its large Rosseland opacity. In the optically thin regime, gas can contribute in the large opacity (emissivity) case because gas-to-gas collision rate is invariably faster than the dust-to-gas coupling. Thermal radiation time (3.4) is inversely proportional to the Planck mean opacity, which makes it grow longer in case of dust depletion (3.16). Yet the collision time increases with dust depletion as the total grain surface shrinks. This will inevitably make the gas preferable relaxant at some point.

Under typical PPD conditions, the Rosseland mean is dominated by the dust continuum below some 1 500 K, but the Planck means of the gas and the dust compare down to at least 650 K owing to

molecular rho-vibrational bands [Malygin et al., 2014]. Thus, the gas and the dust are comparable LTE emitters at those temperatures. In the parameter space of lower temperatures, gas chemistry and opacity in discs are poorly constrained. We use large and small gas opacity models (Sect. 3.4.3) as shown in Fig. 3.10a,b, respectively. The diffusive relaxation in Fig. 3.10 is calculated for $k_r \mathrm{H} = 10$, but the qualitative trend holds valid for other wavelengths.

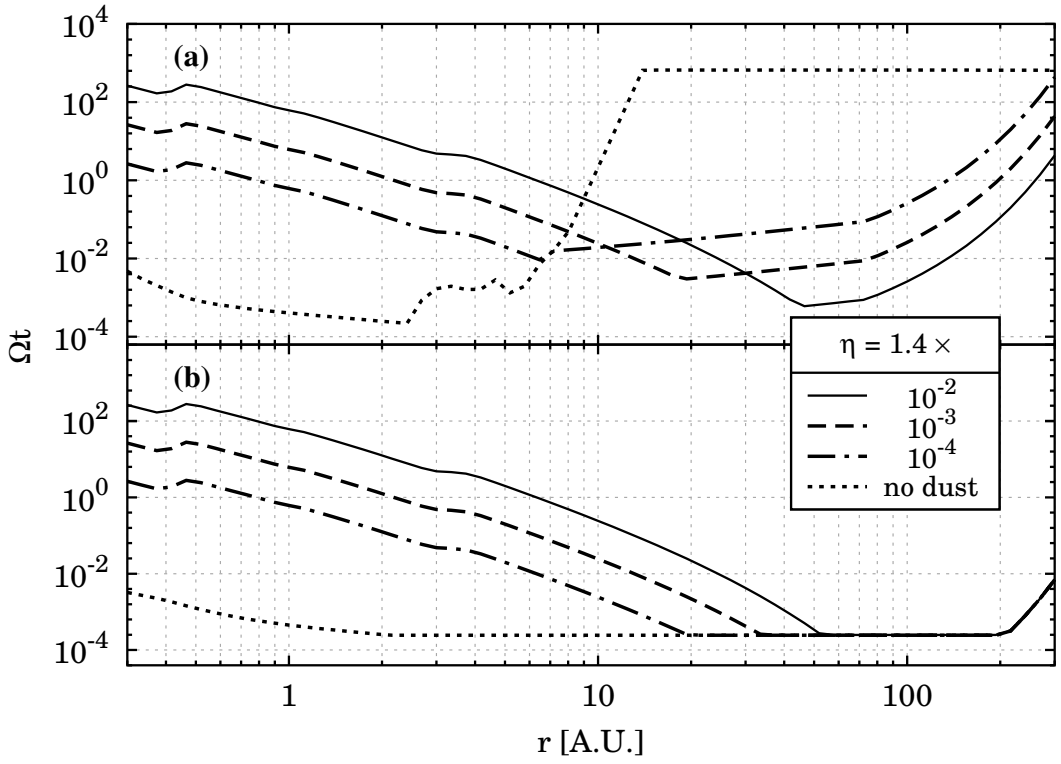


**Figure 3.10:** Effect of reducing dust-to-gas mass ratio $\eta$. The relaxation time of midplane modes with $k_r \mathrm{H} = 10$ versus radial location for (a) the small gas opacity, and (b) the large gas opacity.

Dust amount reduction (fewer absorbers) yields faster relaxation of the thick modes of the same wavelength because $t_{\mathrm{thick}} \propto \tau_{\mathrm{R}}$. The thin relaxation slows down in the small gas opacity case (Fig. 3.10a) as the dust amount decreases, $t_{\mathrm{thin}} \propto \varkappa_{\mathrm{P}}^{-1}$. In this case, disc regions $> 60$ AU are collisionally decoupled, and those closer yet optically thin regions relax on the dust radiation time. When the dust is totally depleted (the dotted line in Fig. 3.10a), almost the whole disc is optically thin in vertical direction with the relaxation being restrained by the gas emissivity. The disc gets into a bimodal relaxation regime (see also Fig. 3.11d): fast relaxation within $\approx 8$ AU before the drastic opacity drop at $\approx 120$ K; and slow relaxation beyond 10 AU with a small constant opacity of $\varkappa_{\mathrm{P}} \approx 10^{-6} \mathrm{cm}^2 \mathrm{g}^{-1}$. In the large gas opacity case (Fig. 3.10b), the optically thin regime does not "feel" the dust depletion because the gas furnishes the relaxation as a comparable emitter with yet faster collisional coupling. This has applications for the vertical shear instability (VSI, see Sect. 4.1.3).

Lin & Youdin [2015] suggested that dust depletion caused, e.g., by the core accretion would impede the development of the VSI. The authors, however, assumed zero gas opacity. Figures 3.11 and 3.12 show the relaxation maps of $k_r \mathrm{H} = 10$ modes under different dust depletion degrees for the small and the large gas opacity cases, respectively. The fast relaxation domain hospitable to the linear growth of such modes crosses the midplane beyond $\approx 20$ AU and extends up to $120 - 220$ AU for a typical dust-to-gas mass ratio of $\eta = 1.4 \times 10^{-2}$ (Figs. 3.11a,3.12a). Above the midplane, it moves closer to the star. Gas opacity bump at around $2.5 \times 10^2$ K in the small gas opacity model is responsible for the expansion of the fast relaxation region within $\approx 7$ AU into layers above 3H, Fig. 3.11a. Because the dust is collisionally decoupled there, the gas determines the relaxation, $t_{\mathrm{relax}} = t^g_{\mathrm{relax}}$, being constrained by the gas emissivity $t^g_{\mathrm{relas}} = t^g_{\mathrm{emit}}$ until up to $z \geqslant 4.5\mathrm{H}$, where the gas itself is collisionally decoupled: $t_{\mathrm{relax}} = t^g_{\mathrm{coll}}$. In the small gas opacity case, finite dust depletion (Figs. 3.11a-c,) makes the arc-like part of the VSI-friendly domain shrink beyond $\approx 10$ AU, but simultaneously draws its lower border closer to the midplane inside $\approx 7$ AU. The first effect is due to the reduction of the total dust emission and collision surface in the optically thin regime, the second – due to the reduction of the dust opacity (per unit gas mass) in the optically thick regime. Total dust depletion (Fig. 3.11d) ultimately yields a bimodal relaxation structure in the optically thin gaseous disc: dynamically long relaxation time beyond 10 AU owing to the small gas emissivity at low temperatures, and dynamically fast relaxation within 7 AU due to the larger gas emission power at higher temperatures. The spatial gradient $d \ln (\Omega t) / d \ln r$ in the transition region is steep, $\approx 13$, and is caused by the rapid opacity change.

The case of the large gas opacity at small temperatures is shown in Fig. 3.12. Because of more efficient collisional coupling and high emissivity, the gas sets the relaxation in the optically thin outer layers $> 50$ AU, even for the fiducial dust-to-gas mass ratio (cf. Fig. 3.10): dust reduction affects only the optically thick parts. Depletion of the dust is likely to be a non-homogeneous and dynamical process, but the maps 3.11 and 3.12 convey the idea that an account for a finite gas opacity is important for the thermal relaxation and can affect the linear phase of the hydrodynamic instabilities (see also Sect. 4).

### 3.5.6 Disc mass

The effect of varying the disc mass is shown in Fig. 3.13. The optically thick relaxation is affected by this in a similar way as by varying the perturbation wavelength (Sect. 3.5.3). But varying the disc mass alters the volumetric density, which changes the collision time. Both the pattern in the upper right (the collision time) and the bottom left (the radiative diffusion time) in each panel of Fig. 3.13 move coherently with the mass change. Massive discs have layers of fast relaxation narrower and located farther out than the lighter discs.

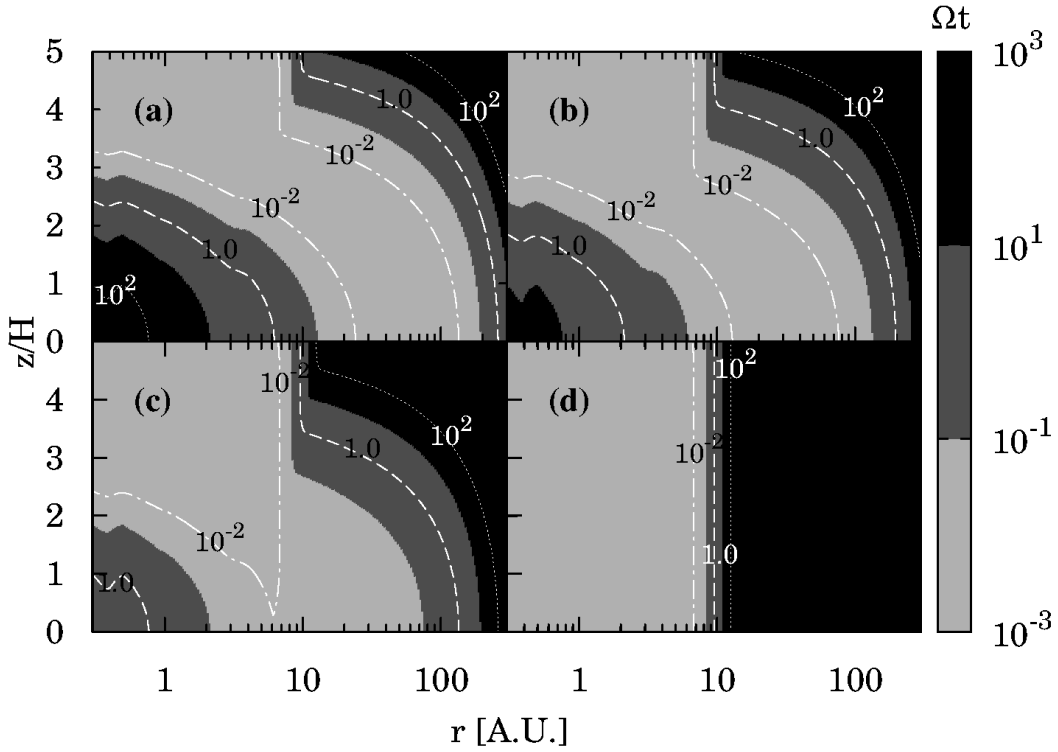


**Figure 3.11:** Relaxation time maps of $k_r\mathrm{H} = 10$ perturbations for different dust depletion factors. The fiducial dust-to-gas mass ratio $\eta = 1.4 \times 10^{-2}$ (a), is then reduced by $10^{-1}$ (b), and $10^{-2}$ (c). Panel (d) shows the case of zero dust.

## 3.6 Discussion

### 3.6.1 Temperature relaxation, not disc cooling

Relaxation time is essentially different a concept than the cooling time of the entire annulus. The latter is estimated as the thermal energy budget per unit surface area of the disc divided by the escaping radiative flux. Approximating the relaxation time by such value, one assigns it to relaxation times of all perturbation wavelengths at that radial location. However, if a perturbation wavelength $\lambda$ is smaller than the distance between $\tau_\mathrm{R} = 2/3$ borders of the atmosphere, the diffusion time over $\lambda$ is shorter than the cooling time of the hosting annulus. Modes with wavelengths smaller than the diffusion length scale can relax yet faster when the relaxation is limited by the thermal emission time. Thus, we distinguish between two different regimes of relaxation a mode of the same wavelength can experience: the optically thick and the optically thin (see Fig. 3.4). A decisive characteristic in this light is the Rosseland depth over the spatial wavelength (see Eq. 3.10 and Fig. 3.3). Optically thick perturbations relax via radiative diffusion ($t_\mathrm{thick} \propto \tau_\mathrm{R}\lambda$), optically thin ones – via thermal emission if collision time is sufficiently short. In the first case, the time of relaxation depends quadratically on

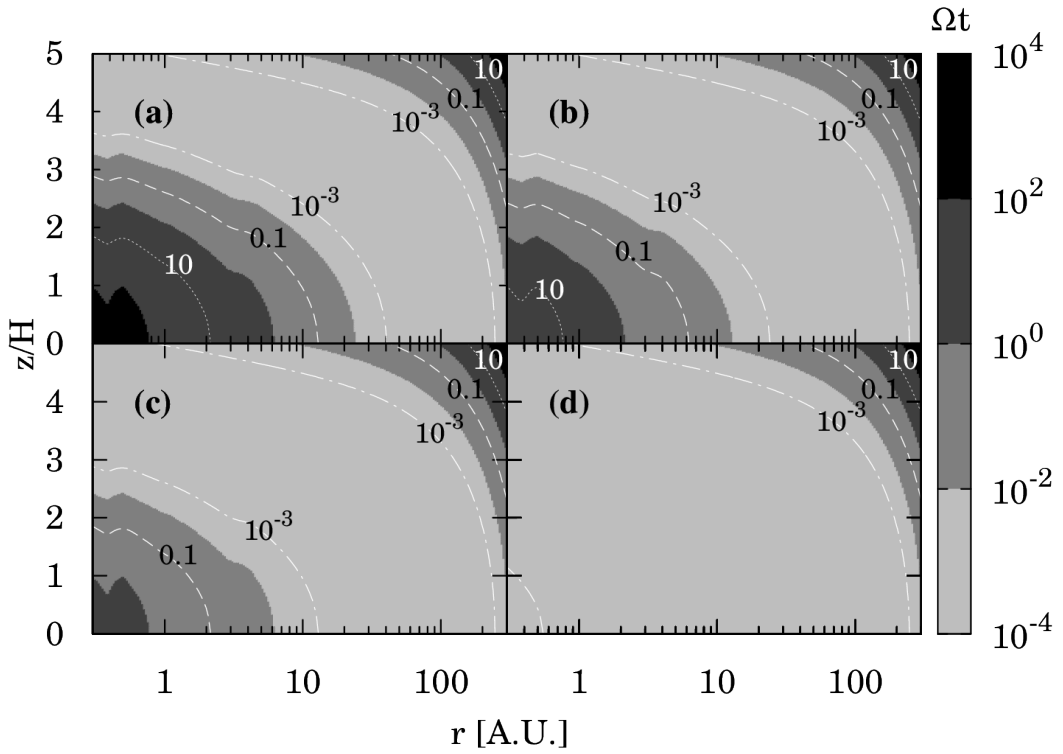


**Figure 3.12:** Same as Fig. 3.11 but for the large gas opacity case.

the perturbation wavelength $\lambda$, in the second one it is independent of it. The thermal radiation time is governed by the emissivity of the material ($t_{\rm thin} \propto \varkappa_{\rm P}^{-1}$). The antipodal relation to opacity in the two regimes results in the opposite response to the reduction of dust amount [see Sect. 3.5.5 in this study as well as Cai et al., 2006]. Increasing the number of dust particles, or the total number of absorbers, increases the diffusion time (higher opacity: $t_{\rm diff} \propto \varkappa_{\rm R}$), but decreases the optically thin relaxation time (more emitters – faster relaxation: $t_{\rm thin} \propto \varkappa_{\rm P}^{-1}$). In latter case, only to some lower limit, stemming either from the finite coupling time (dust-to-gas collision time) or the gas radiation time. On the contrary, lowering the number of dust particles decreases the optically thick and increases the optically thin relaxation time with an upper limit on the latter being the optically thin relaxation time of the dust-free gas (may be set both by the collision or emission time, see Sect. 3.5.5). We do not consider here any time evolution of the dust, which is required to accurately determine the relaxation times in the hot inner disc as pointed out in Nelson et al. [2000]. Our midplane temperatures never exceed those of severe dust depletion (still the ice lines are captured in dust opacity tables).

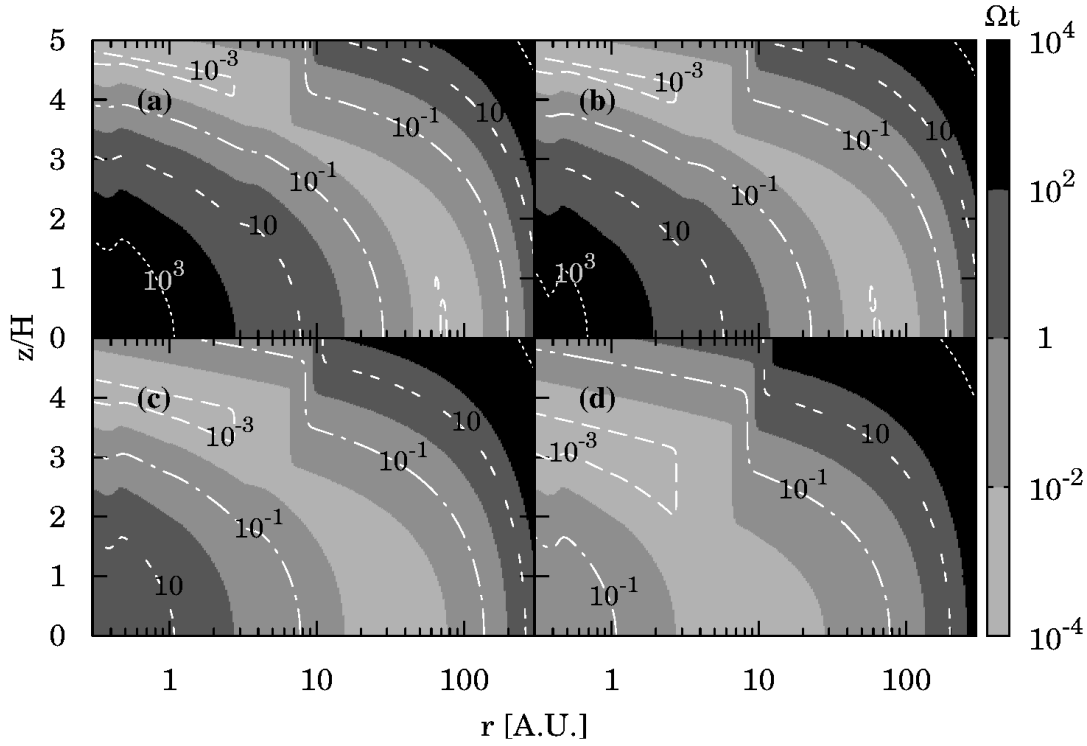


**Figure 3.13:** Thermal relaxation time of 2H perturbations for different disc masses: $\mathcal{M}_{\rm disc} = 0.1 M_\odot$ **(a)**, $0.064 M_\odot$ **(b)**, $0.01 M_\odot$ **(c)**, $0.001 M_\odot$ **(d)**.

### 3.6.2 On flux limiter

The flux limiter as introduced by Levermore & Pomraning [1981] reads

$$\kappa = \frac{2+R}{6+3R+R^2} \tag{3.19}$$

with

$$R = \frac{|\nabla E_{\rm R}|}{\varkappa_{\rm R}\varrho E_{\rm R}} \tag{3.20}$$

being the relation of the diffusion length $(\varkappa_{\rm R}\varrho)^{-1}$ to the characteristic length of the radiation energy density change $E_{\rm R}/|\nabla E_{\rm R}|$. Such defined, the flux limiter provides satisfying causality: in the optically thin (free-streaming) limit, $R \gg 1$, the radiative flux becomes $\vec{F} = -cE_{\rm R}\nabla E_{\rm R}\,|\nabla E_{\rm R}|$. This does not limit, though, the production ability of the radiative energy by the material. Relaxation time (3.9) with the flux limiter being in the free-streaming limit is the propagation time of light over the perturbation wavelength, $\lambda/c$, up to a factor of $3\lambda/l_{\rm diff} < 1$. This can become very short in the optically thin regions [see Stoll & Kley, 2014, Fig.18]. A characteristic thermal emission time (3.4) is longer than the diffusion time (3.9) in this regime (Fig. 3.4). Equation (A.14) can not be, generally,

applied in the optically thin case even if the diffusion coefficient is bounded by the flux limiter. This is because the flux limiter does not contain the information on the emissivity and the collision time. Radiation energy production rate of any material at equilibrium temperature $T$ is given by Kirchhoff's law

$$\varepsilon = \frac{dE}{dt\, dm\, d\Omega} = c\varkappa_{\mathrm{P}} \frac{aT^4}{4\pi}. \tag{3.21}$$

Estimating the thermal radiation time as a ratio of the specific thermal energy $c_{\mathrm{v}} T$ to emissivity (3.21) properly integrated over the solid angle, gives (3.4). This time is finite because of non-zero heat capacity of the gas and finite emissivity (3.21) of the matter. The corresponding collision time must be shorter than emission time (3.4) for relaxation to be set by the latter.

### 3.6.3 Stochastic nature of density perturbations

Critical cooling time is a constrain on the onset of gravitational instability in Toomre-unstable discs [Gammie, 2001]. However, the value of this time has so far evaded an approved determination in numerical experiments on self-gravitating turbulent discs. Different codes, physical prescriptions (e.g., equations of state), and numerical viscosity handling within one code all produced different results. The concept of a simple parametrisation of cooling is only justified for accretion discs in thermal equilibrium [Pringle, 1981] under the assumption of uniform viscosity [Shakura & Sunyaev, 1973].

The classical Toomre criterion, originally derived for a stellar disc [Toomre, 1964], was first questioned to be a relevant necessary condition in application to *turbulent* accretion discs by Paardekooper [2012]. A thorough analytic study by Hopkins & Christiansen [2013] confirms the Toomre $Q$ criterion is a necessary, but not a sufficient one in the presence of stochastic density fluctuations. Thus, a turbulent disc can be considered stable only in a statistical sense, over some finite period of time. The scatter of the numerically determined critical cooling time is in excellent quantitative agreement with analytic predictions by Hopkins & Christiansen [2013], suggesting this issue can be explained by stochastic nature of turbulence.

The widely accepted approaches of dynamically constant [ $\Omega t = \mathrm{const}$, Gammie, 2001; Johnson & Gammie, 2003; Rice et al., 2003] or globally constant [$t = \mathrm{const}$, Mejía et al., 2003; Boley et al., 2006, see also Mejía et al. 2005, where they compare the two approaches] relaxation rates disagree with the radial profile of the relaxation rate for the most unstable to self-gravity mode $\lambda_z = 2\mathrm{H}$ (see Fig. 4.4). In numerical modelling, the cooling rate of a particle/grid cell can be estimated via (3.2) with the direction of the least Rosseland thickness used in diffusion time (3.9). Because the relaxation rates can only be calculated for a given perturbation mode, the spectrum of perturbations determines the "average" classical cooling condition analogous to the classical $Q$ criterion. Adding information about the phases yields a "statistical" critical cooling alike the statistical $Q$ criterion by

Hopkins & Christiansen [2013].

### 3.6.4 The method: thin and thick

In this section we discuss the borders of the current method and argue on the robustness of the main results. We highlight the prior points of improvement.

The optically thin relaxation time is a local quantity, we evaluate it at a given point – the extremum (minimum or maximum) of the perturbation amplitude $|\delta T_0|$. In linear analysis, relaxation time (3.2) is independent of the value of $\delta T_0$, and is solely defined by the location in the disc. If we consider a spatial distribution (Fourier mode) $\delta T(\vec{x})$, each point can be assigned a value of the relaxation time. We make a simplification by taking the relaxation time at the point of extremal $\delta T = \delta T_{\min/\max} = \delta T_m$ for the relaxation time of the optically thin mode. This is justified for smooth Planck opacity.

The optically thick relaxation time demands non-local calculations: the photons born at the point of $\delta T_0$ subsequently diffuse through the medium with $0 < |\delta T/\delta T_m| < 1$. Variations of the diffusion length at those points alter the relaxation time. Therefore, we first harmonically average the diffusion coefficient over $\lambda$ (see Appendix A.2). Such averaging makes the relaxation time dependent not only on location and wavelength, but also on the direction. For an arbitrary optically thick perturbation $(k_z, k_r, m)$, the bulk of the excess thermal energy escapes through the direction of the least Rosseland depth [cf. the flashlight effect, Nakano, 1989]. For midplane perturbations with $k_z \sim k_r$, this is the vertical direction (Fig. 3.8,3.9a).

The radiative diffusion and thermal emission times both imply fast – on times shorter than the relaxation time itself – thermal coupling between the radiating species (dust and gas) and the thermal carriers (gas). Fast coupling is plausible at high densities, but is not always valid in optically thin regions. If the time to set LTE is longer than thermal radiation time (3.4), we limit the relaxation by the former time. We approximate the time to establish LTE by a collision time with no account for non-LTE cooling and non-equilibrium thermal feedback processes between the dust, the gas and the radiation field (external irradiation) in the low-dense regions. This can be done as next refinement.

In this paper, we consider radiative transfer as the only mean of thermal relaxation. Whilst thermal conduction in PPDs is highly inefficient, the role of convection is not entirely settled. Boss [2001, 2002, 2004] argued that convective motions driven in the inner part of a disc can provide fast cooling of the midplane. This result was later questioned in Cai et al. [2010]. A recent study by Hirose [2015] constrains the thermal conditions required for the onset of the convective energy transport near the midplane. The onset of convection requires an unstable stratification *a priori*.

The optical depths and emission rates are calculated using the joint dust and gas mean opacity tables. At low temperatures ($\leqslant 1\,500$ K), Rosseland opacity of ISM dust exceeds that of solar-mixture gas by several orders of magnitude. Hence, adding the two means does not introduce a considerable error

far from the dust sublimation temperature: the opacity is either dominated by the dust or by the gas. At the transition temperatures as well as in case of considerable (by a factor of $\approx 10^2$ or more) dust depletion, this approach does not hold valid because Rosseland averaging is not additive.

Not only a change in the dust chemistry but also in size distribution alters the resulting dust opacity spectrum [Pollack et al., 1994; Henning & Stognienko, 1996]. As pointed out in Nelson et al. [2000], the grain size evolution proceeds on short (relative to the local orbital period) times in the inner disc, and therefore, calculating the radiative relaxation there necessitates advanced calculations with time-dependent size and composition of the grains. In the atmospheric layers imposed to external radiation, the photochemistry alters both dust and gas opacities, and the assumptions of equilibrium chemistry and LTE under which the opacities were calculated break. Collisional decoupling at low densities serves to delineate the border of validity.

Gas chemistry in dusty environments of discs is poorly constrained yet many important reaction rates and transitions have not been measured in laboratories [Dutrey et al., 2014]. Our two gas opacity models are contrived to probe the parameter space. The analysis would benefit from the yet missing consistent dust and gas opacity calculations.

An ideal gas equation of state with $\gamma = 5/3$ was employed.

*…our object is to constrain the enemy, to accomplish our will.*

George Waschington, paraphrased

# 4

# Constraining Hydrodynamic & Gravitational Instabilities

## 4.1 Birthplaces of hydrodynamic instabilities

Pure hydrodynamic instabilities (as opposed to MRI) are amendable in the context of accretion discs because can operate in magnetically inactive regions. The onset of hydrodynamic instabilities in PPDs is granted under certain thermal relaxation conditions. With relaxation rates being parametrised as

$$t_{\text{relax}} = \beta\Omega^{-1}, \tag{4.1}$$

the growth rates of the modes peak at certain values of $\beta$. The corresponding contour lines on a relaxation map delineate the regions of inception of the respective instability modes (see Fig. 4.1). The bulk of the disc volume is prone to the convective overstability (white), with an embedded layer, where the vertically elongated motions can be driven by the vertical shear (hatched). The replication of vortices can operate in the dense inner regions of the disc (grey) provided finite-amplitude noise has been seeded there.

### 4.1.1 Zombie vortices instability (ZVI)

Numerical experiments on linearly stable Taylor-Couette flows with initial vertical stratification [Marcus et al., 2013] revealed a finite-amplitude instability, the zombie vortex instability (ZVI). Although it requires some initial noise, a Kolmogorov spectrum of infinitesimally small amplitude would trigger the ZVI given the spatial resolution enough to discern the eddies with sufficiently high Rossby number ($\geqslant 0.2$). The ZVI is a subcritical instability under long thermal relaxation times [$\Omega t \gg 1$, Marcus et al., 2015]. Though the estimates of the angular momentum transport rate from the ZVI are not yet conclusive due to small domains considered in numerical studies, the ZVI can contribute to the coupling mechanism of the cold midplane gas to the surface magnetic fields [turbulent mixing, Turner et al., 2007].

The optically thick parts of the disc with slow thermal relaxation can host ZVI. For $\lambda/H = 2$ modes, the regions with $\Omega t \geq 10^2$ are shaded with grey in Fig. 4.1. The relaxation criterion alone permits ZVI in both the optically thick region within 2 AU (and $\pm 2$ H around the midplane) as well as in the low-density atmosphere or disc outskirts (beyond 500 AU). However, in the atmospheric layers, an account for non-equilibrium processes and photochemistry is required for a viable estimate of the relaxation time. In addition, the gas can be photoionised sufficiently for the MRI to set in.

### 4.1.2 Vortices: an instability growing from linear convective overstability (COV)

Centrifugally supported flows with global radial variations in pressure and entropy (baroclinic) can be unstable to non-axisymmetric perturbations. Klahr & Bodenheimer [2003] identified in the 2D numerical experiments on vertically integrated non-self-gravitating, non-magnetic discs an instability driven by a negative radial entropy gradient. Klahr [2004] have found, though, that the intrinsic shear makes Keplerian baroclinic discs linearly stable under infinite relaxation times. Further, Johnson & Gammie [2005]; Petersen et al. [2007]; Lesur & Papaloizou [2010]; Lyra & Klahr [2011] inferred that (likewise for ZVI) a finite-size initial perturbation is required even in presence of finite (fast) thermal relaxation. Hence, the instability was named subcritical (subcritical baroclinic instability, SBI). SBI eventually yields stable vortices, which can induce (via Rossby waves) Reynolds stresses rateable to $\alpha = 10^{-4} - 10^{-2}$. These anticyclonic vortices can be triggers for fast and efficient planetesimal formation [Klahr, 2003].

A linear regime of SBI was ultimately discovered in both analytic and numerical studies on radially stratified accretion discs by Klahr & Hubbard [2014], who suggested term "convective overstability" (COV). Lyra [2014] confirmed the phenomenon via compressible linear analysis and demonstrated in both 2D and 3D shearing box runs that the SBI is indeed the saturated state of the convective overstability.

The growth rate of the convective overstability is predicted to peak at $\Omega t \sim 0.7$ [for $z - \varphi$ modes Klahr & Hubbard, 2014], which defines two surfaces located approximately around the hashed region in Fig. 4.1. However, the COV can develop over almost the entire range of thermal relaxation times: the growth rate drops to 1% from the maximum within $10^{-2} \leqslant \Omega t \leqslant 10^{2}$. Such rates are gained by $\lambda_z = 2H$ modes in the midplane from $\sim 2$ AU all the way up to 300 AU, the largest radial separation considered here. Away from the midplane, the suitable relaxation zone bends towards the central object (the white area in Fig. 4.1).

### 4.1.3 Vertical shear instability (VSI)

Baroclinic rotationally supported flows have vertical shear: a variation in angular frequency along the rotation axis. This vertical shear can drive axisymmetric inertial waves linearly unstable under quasi isothermal (i.e. fast) relaxation [Urpin & Brandenburg, 1998; Urpin, 2003]. Vertically elongated disturbances ($k_r/k_z \gg 1$) can overcome the Coriolis stabilisation. This justified the framework of isothermal radially local analysis in early numerical [Arlt & Urpin, 2004] and analytical [McNally & Pessah, 2014] works on the VSI. The fast cooling is required to diminish the stabilizing vertical buoyancy [Lin & Youdin, 2015]. Reported angular momentum transfer rates resulting from the VSI are modest: $\alpha \approx 10^{-4}$ [Arlt & Urpin, 2004; Nelson et al., 2013; Stoll & Kley, 2014].
Nelson et al. [2013] performed detailed numerical study of the VSI for two classes of equilibrium disc structures (with either temperature or entropy being constant on cylinders) under different relaxation rates. The discs were resolved in both radial and vertical directions. The isentropic models (involving integration of the energy equation with an ideal gas equation of state) indeed demonstrated the requirement of very rapid thermal relaxation $\Omega t \leqslant 10^{-2}$ (as follows from the analysis of the perturbed kinetic energy evolution). In contrast, the locally polytropic models pushed the critical relaxation limit as far as to $\Omega t \approx 10$ for specific temperature and density profiles. In analytic investigation of the VSI including the radiative cooling Lin & Youdin [2015] confirm a generic utility of the critical cooling time scale

$$\Omega t_c = \frac{h|q|}{\gamma - 1} \tag{4.2}$$

with $h$ being the disc aspect ratio, $q$ the radial power-law temperature gradient, and $\gamma$ the adiabatic index. Lin & Youdin [2015] showed that time (4.2) is a robust critical relaxation criterion for modes $5 \leq k_r H \leq 10$. For low-frequency modes $k_r H = 1$, the threshold is at slightly longer times. For high-frequency modes $k_r H \geqslant 30$, the growth indeed carries on for cooling times considerably longer than (4.2), but the growth rate drops significantly [see Fig.13 in Lin & Youdin, 2015].
A zone of onset of VSI modes $\lambda_r/H = 0.628$ as predicted by $t < t_c = 6.25 \times 10^{-2}\Omega^{-1}$ is hashed with grey lines in Fig. 4.1.

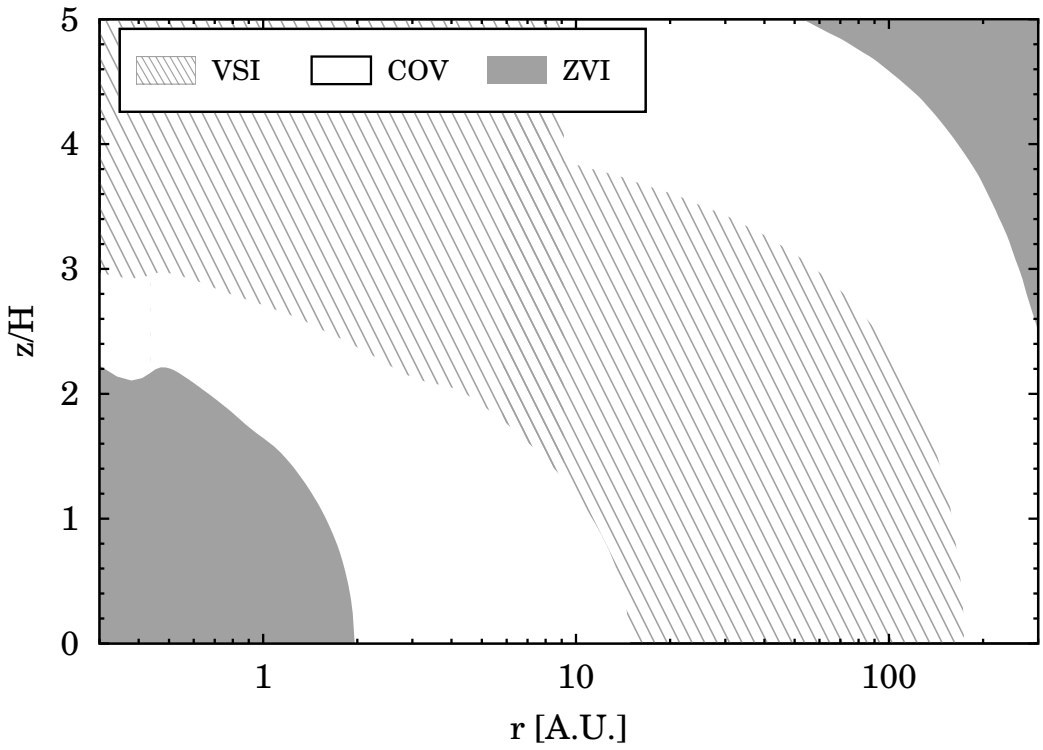


**Figure 4.1:** Onset locations of the transport inducing hydrodynamic instabilities as constrained by respective thermal relaxation criteria (see text).

## 4.2 Uniform $Q = 1$ disc

A dynamical equilibrium with $Q \sim 1$ was observed in many numerical experiments on turbulent self-gravitating discs, as analytic arguments predict [Paczynski, 1978; Bertin, 1997]. Such a state results from balancing the heating (from the turbulent cascade dissipation) and the (radiative) cooling rates. While the heating rate usually enters the modelling via numerical viscosity which mimics the Navier-Stokes kinematic viscosity, the cooling rate is often parametrised. Using the introduced recipe, we can calculate the radiative relaxation rate of linear temperature perturbations in a Toomre unstable disc. For this purpose, we deliberately construct a disc model with a uniform Toomre $Q$ of unity.

### 4.2.1 Setup

We start with a temperature profile of a passive irradiated disc with a given aspect ratio $H/r$

$$T(R) = \sqrt[4]{T_*^4 \left(\frac{r}{R_*}\right)^{-2} \frac{H}{r} + T_{\mathrm{min}}^4}, \tag{4.3}$$

where $T_*$ is the stellar effective temperature, $R_*$ the stellar radius, and $T_{\rm min}$ is set at 10 K. To get a Toomre $Q$ independent of radius, we set a surface density power-law index $p = 7/4$. The disc mass of $\sim 0.8\mathcal{M}_\odot$ assures $Q = 1$ for $H/r = 0.05$ disc around a solar-like star.

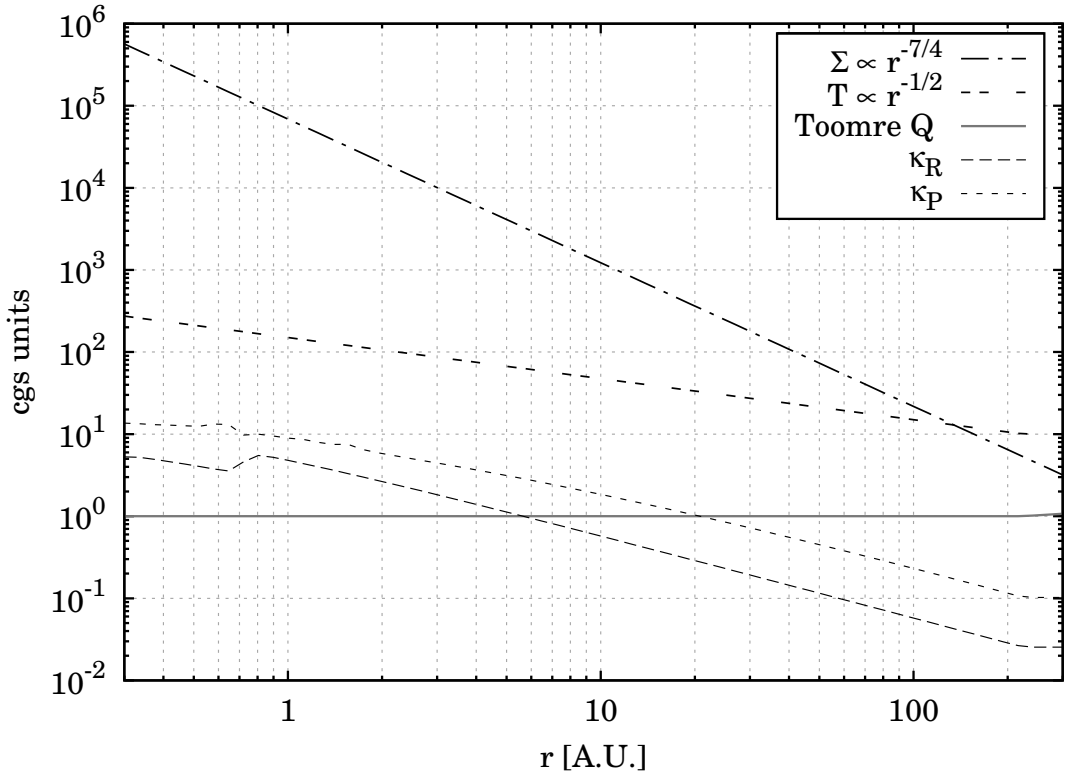


**Figure 4.2:** $Q$-flat disc set-up. Surface density (dot-dashed), temperature (double-dashed) and the corresponding Toomre $Q = 1$ (grey solid). The Rosseland (long-dashed) and the Planck (short-dashed) opacities as a function of radial distance through the midplane are shown.

Figure 4.2 displays the density-temperature set-up and the midplane opacities.

### 4.2.2 Thermal relaxation in a $Q = 1$ disc

In Fig. 4.3a, the relaxation time for the mid-plane perturbations of different wavelengths as a function of radius is drawn. The two regimes of relaxation are clearly distinguished: the optically thick regim with $\Omega t$ rapidly decreasing with $r$, and the optically thin regime with $\Omega t$ slowly increasing with $r$. The kink beyond 200 AU is due to the settle of the temperature profile at the minimum value of 10 K. In the optically thick inner regions, the radiative diffusion time even for $\lambda/\mathrm{H} \sim 0.1$ exceeds the viscous time $t_{\rm visc} \sim 10^6$ yr. A tipping point when the trend of a rapid decline $\Omega t \propto r^{-9/2}$ changes for a shallower increase $\propto r^{7/4}$ marks the transition from the optically thick to the optically thin relaxation regime. Figure 4.3b shows a power-law index $p = d\ln \Omega t/d\ln \Sigma$ in

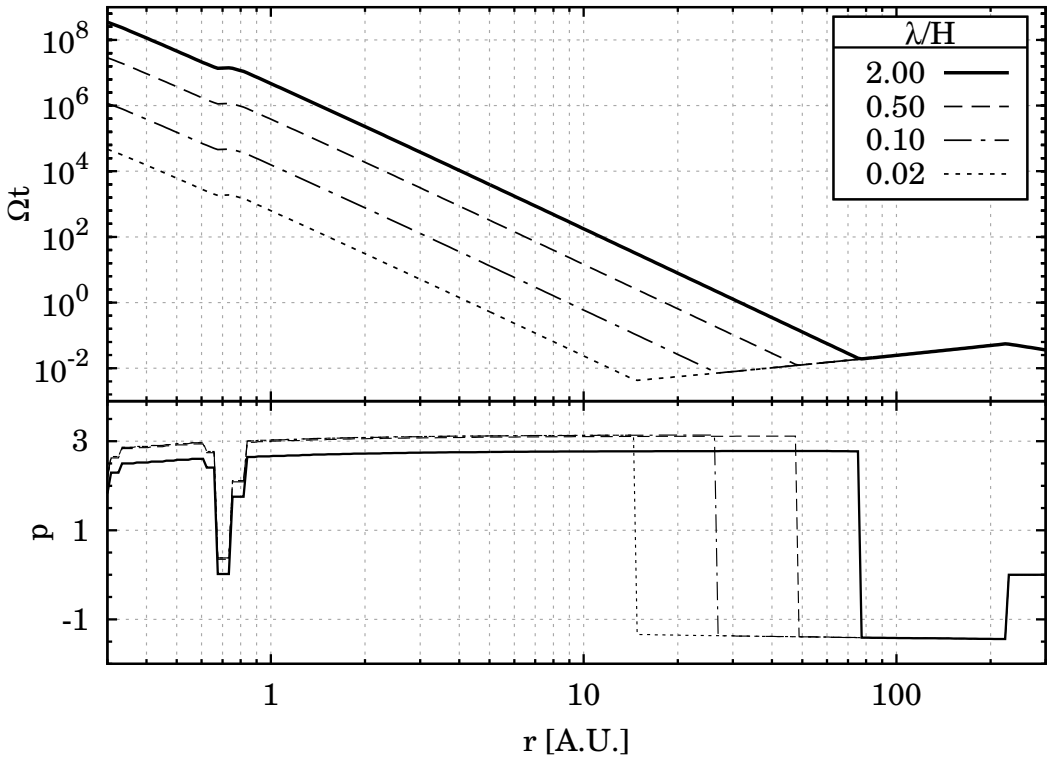


**Figure 4.3:** Radiative relaxation rates of midplane modes in a Toomre $Q = 1$ disc (*top*) and power-law index in relation $\Omega t \propto \Sigma^p$ (*bottom*).

relation

$$\Omega t = \beta \Sigma^{p}. \tag{4.4}$$

The optically thick regime yields $p \sim 2.7 \div 3.0$ (corresponding to $t \propto \Sigma^{1.7 \div 2}$). The water ice line forms a plateau in the relaxation time yielding a pronounced dip with $p \approx 0$ at around 0.7 AU. When the modes become optically thin, the relation reverts to $p \approx -1.4$ and then settles at $p = 0$ when the temperature profile turns flat at 10 K. Taking the critical time for classical stability to be $\Omega t \geqslant 50$ [Paardekooper, 2012; Hopkins & Christiansen, 2013], we find that the region within $\sim 10$ AU is stable against self-gravitation. The area beyond $\sim 30$ AU is a site of catastrophic, runaway fragmentation: $\Omega t < 1$. The zone in between is where one fragmentation within a lifetime can occur. However, if such an event happen, it can enhance the probability of fragmentation at closer radii by accumulating mass in the inner spiral arms [Meru, 2015].

### 4.2.3 Comparisons to other studies

Estimates of the radiative cooling times in PPDs as obtained from calculating vertically integrated azimuthally-averaged thermal energy balance were published in Johnson & Gammie [2003]; Boley et al. [2006] in the context of gravitational instabilities. Watanabe et al. [1990] calculated the cooling time in $1 + 1$D optically thick disc models. A value of the cooling time of a disc annulus approximates the vertical radiative relaxation time of long-wavelength modes (longer than the pressure scale height) at that radial location. Still, short-wavelength perturbations optically thin to thermal radiation are expected to decay faster [Nero & Bjorkman, 2009; Nero, 2010].

For a given temperature and density model, the maximum time criterion (3.2) draws a map of relaxation rate over the disc interiors. In the context of development of the vertical shear instability (VSI), such a map was published in Lin & Youdin [2015, Fig.2]. We note a good qualitative agreement with this result: dynamically long relaxation in the inner optically thick regions and an isothermal pattern (vertical contours) of the fast relaxation farther apart. The quantitative disagreement is due to different disc models, opacities, and computing techniques employed in the two studies. Both the dynamic range and the overall pattern is similar to the presented in Fig. 3.7. In low-density atmospheric layers and cold distant midplane regions, our relaxation time is longer than in Lin & Youdin [2015] due to the account for the collisional decoupling.

Another study containing a calculation of the radiative diffusion time with the flux limiter [Stoll & Kley, 2014, Eq.18] finds arbitrarily short relaxation times in the superficial layers because $t_{\mathrm{diff}} \propto \varrho^{2}$. We confirm that the diffusion time alone leads to such values in the optically thin regime (see Fig. 3.4). We argue, however, that the result is unphysical (see Sect. 3.6.2), and that the relaxation time in the low-density optically thin regions is limited by either the intrinsic radiation processes, or collisions. In particular, the thermal emission time puts a stringent bottom limit on the radiative

relaxation of $\Omega t \approx 10^{-4}$ in the explored domain of the parameter space. The limit is quantum in nature (quantifiable in terms of the Planck mean) and is robust because implies the maximum achievable, LTE emissivity of the given material.

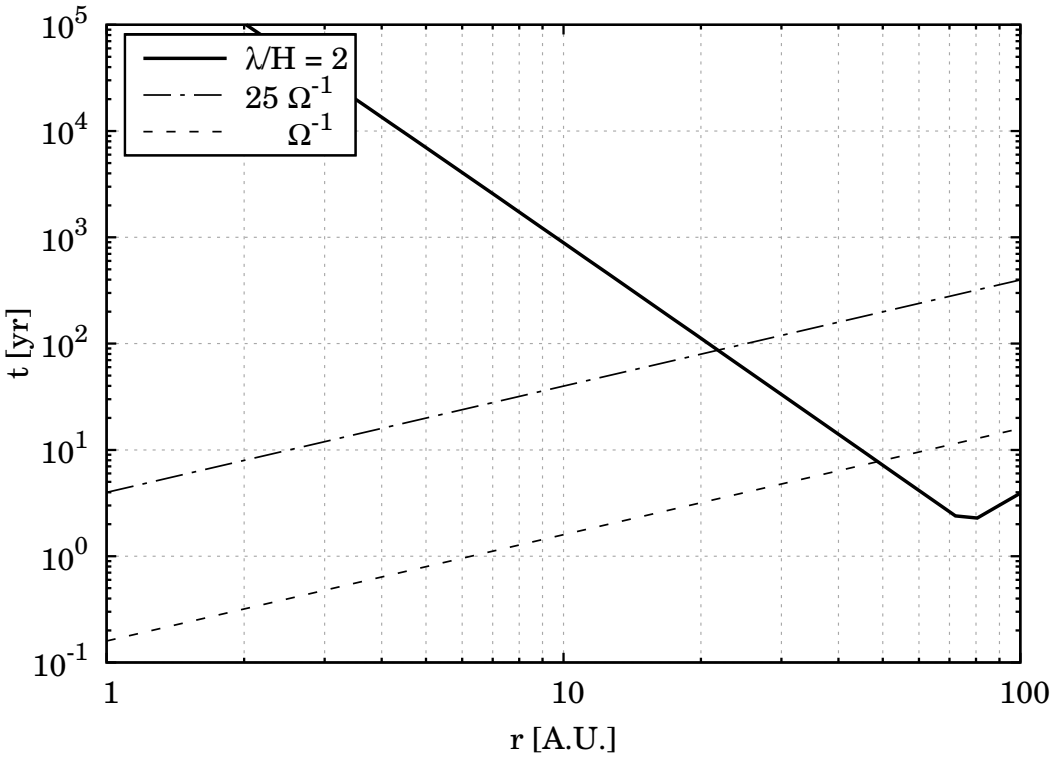


**Figure 4.4:** Relaxation time of 2H midplane modes (solid line) in a $Q = 1$ disc. The dot-dashed and the short-dashed lines show $t = 25\Omega^{-1}$ and $t = \Omega^{-1}$, respectively.

In numerical modelling [e.g. Mejía et al., 2005; Boley et al., 2006; Boley, 2009; Stamatellos & Whitworth, 2008], as well as in analytic studies [e.g. Rafikov, 2005; Durisen et al., 2007] on PPDs, the relaxation time was usually regarded that of a column-wise cooling. Figure 4.4 shows how far off a simple parametrisation (1) can be from radiative relaxation (3.2) of $\lambda/\mathrm{H} = 2$ modes.

*Sometimes no forest is visible behind the trees.*

Russian proverb

# 5 Frequency-binned Gas Opacity

## 5.1 Motivation & challenge

Line opacity varies with frequency way stronger than the continuum opacity. However, it is important in many astrophysical problems of which I pinpoint two: stellar atmospheres and circumstellar discs. From the point of view of structure calculations, the impact of line opacity has not yet been fully explored in the second field but it has been in the first one. Inclusion of the spectral lines in stellar atmosphere modelling results in increasing the temperature of photospheric layers below the level where most of the lines absorb and decreasing the temperature above. This effect is called the line blanketing effect [Milne, 1928; Chandrasekhar, 1935; Böhm, 1954] and manifests observationally as an enhancement of red or infrared parts of a stellar spectrum at the expense of the other regions. In stars cooler than M type, the welfare of molecular lines make the line opacity a principal component in determining the photospheric structure (as it apparently is in the emerging spectrum). The situation is different in circumstellar medium, where dust continuum opacity is generally thought to prevail over the molecular gas contribution. Yorke & Sonnhalter [2002]; Kuiper et al. [2010a] showed that the frequency-dependent irradiation of the dust sublimation front is important for the flashlight effect [Nakano, 1989]. Tanaka & Nakamoto [2011];

Kuiper & Yorke [2013] found that a presence of an optically thick inner gaseous (dust-free) disc can contribute significantly to the flashlight effect altering the accretion history of a massive star. Further, the CSM is inhomogeneous in terms of dust-to-gas density ratio on different spatial and time scales as star and planet formation going on (see Sect. 0.2). That being said, the gas line opacity has to be included in modern simulations for massive star and planet formation.

Inclusion of millions of absorption features poses a computational challenge for radiative transfer modelling, yet the atomic and molecular data are incomplete and uncertain [Kurucz, 2002]. This has conditioned only the harnessing of frequency averaged gas opacity in massive HD+RT modelling. Smoother monochromatic continuum dust opacity can either be parametrised analytically or tabulated with some finite resolution in frequency space (with, typically, $\sim$ 100 bins over $10^{-1}$ $\mu$m – $10^{3}$ $\mu$m). Stellar atmosphere modelling offers two major paths of including gas line opacity: the opacity probability distribution function (OPDF) and the opacity sampling (OS). Below I briefly describe the two arguing about their utility in modelling anisotropic environments like circumstellar discs.

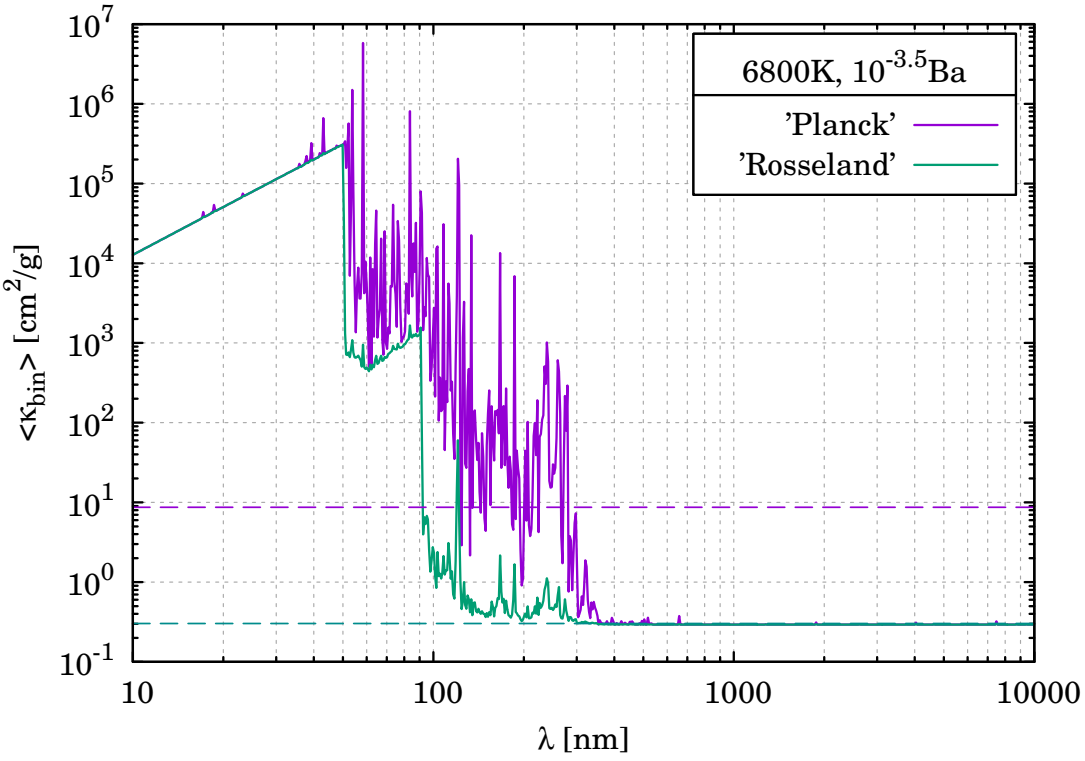


**Figure 5.1:** Direct ('Planck') and inverse ('Rosseland') opacity averages over frequency bins. $T = 6800$ K, $\varrho \approx 4.3 \times 10^{-16}$ g cm$^{-3}$, $N_{\text{bins}} = 10^3$. The dashed lines show the corresponding Planck and Rosseland means obtained by averaging over the entire $\lambda$ range.

## 5.2 Opacity probability distribution function

OPDF is a method for handling the line opacity in stellar atmospheres originally proposed by [Labs, 1951]. Strongly varying with frequency line opacity is converted into a continuum-like opacity by means of calculating the probability of a given opacity to occur in the chosen frequency interval [Kurucz et al., 1974]. This is done as follows: for a given thermodynamic ($T$, $P$) and microturbulent ($\xi_t$) parameters, the line absorption $l_\nu$ of a gas with defined atomic abundances is calculated on a fine-step frequency grid. Within a chosen frequency interval $[\nu_{-1/2}, \nu_{+1/2}]$ encompassing $\sim 10^3$ points of the fine grid, $l_\nu$ is rearranged as a non-decreasing function of $\nu$. This opacity distribution function is turned into a coarser step function by averaging within some (of order 10) number of subintervals. A specific implementation of OPDF contains as many as 1212 such frequency intervals over 8.97666 nm – $10^4$ nm wavelength range [Castelli, 2005]. Two major limitations of OPDF [Kurucz, 1970] are: (i) that the *relative* shape of the absorption-coefficient spectrum is independent of depth; (ii) the artificial shift of large opacities to the one side of the frequency interval, and the small opacities – to the other. Inaccuracies in a treatment of monochromatic (binned) absorption with frequency and depth yields errors in the respective monochromatic (integrated over the bin) flux in dependence on depth, which is essential for radiative feedback calculations.
OPDF was successfully applied in context of spherically symmetric (1D) radiative transport in blanketed atmospheres of hot dwarfs and giants [Strom & Kurucz, 1966; Kurucz et al., 1974; Kurucz, 1979]. Its feasibility is questioned for cooler stars [Querci et al., 1974; van Paradijs & Vardya, 1975], where the opacity sampling method came to the use instead.

## 5.3 Opacity sampling

The idea behind the method was to find a minimum set of frequency points which incorporation in radiative transfer calculations accurately reproduce the temperature structure of molecular gas (in particular, of photospheres of cool stars). Opacity sampling method, presented in Peytremann [1974a], have been used for atmosphere modelling [Peytremann, 1974b] and photometric studies [Peytremann, 1975]. Sneden et al. [1976] showed the virtues of OS for LTE departures as well as its flexibility to changing the absorption data input. Its incorporation in different variations into ATLAS-based branch of codes made possible extensive investigations on cool dwarves' atmospheres [Pavlenko, 1991d,b, 1997a,b], non-LTE giants atmospheres [Pavlenko, 1991a,c], and other studies [Pavlenko, 2003; Pavlenko & Yakovina, 2010; Malygin et al., 2012]. A particular realisation includes pseudo-random sampling of frequency intervals of finite width (say, $\Delta\nu/\nu = 0.3 \times 10^{-4}$), within which the high-resolution ($R \sim 5 \times 10^5$) opacity spectrum is accurately calculated. The sufficient number of such intervals determined from desirable convergence of temperature structure and

integrated fluxes in cool carbon-rich atmospheres is about $5 \times 10^2 - 10^3$ [Peytremann, 1974a; Sneden et al., 1976].
This method is computationally more expensive than OPDF, so I decided to first try a compromising solution – tabulated straight and reciprocal frequency-binned opacities.

## 5.4 Planck & Rosseland bin averaging

Grey gas opacities [like Bell & Lin, 1994] have already been in use in numerical modelling for circumstellar discs. Most of radiative transport schemes involve two types of frequency averages: the Rosseland (1.5) and the Planck (1.7) means. The first measures transparency of the gas in the optically thick limit, when radiation energy propagates diffusively. It is dominated by the line wings or continuum opacity (if there are no lines). The second measures opaqueness of the gas: it is dominated by the line cores and can be used in calculating optically thin absorption or LTE emission. The radiative schemes used in coupled HD + RT modelling are usually split into ray tracing and diffusive parts relying on tabulated opacities. This further justifies the choice to tabulate straight and reciprocal means in each frequency bin. An example of such means is shown in Fig. 5.1. This also shows how actual frequency-dependent opacity (solid lines in Fig. 5.1) can differ from the frequency-averaged values (dashed lines). Figure 5.2 expands this by plotting together with weighting Planck functions, also at different temperatures as it is in case of the two-temperature Planck means. Figures 5.3,5.4 show how the frequency averaged within the bins opacity recover the total Planck and Rosseland means. The number of bins is $10^3$.

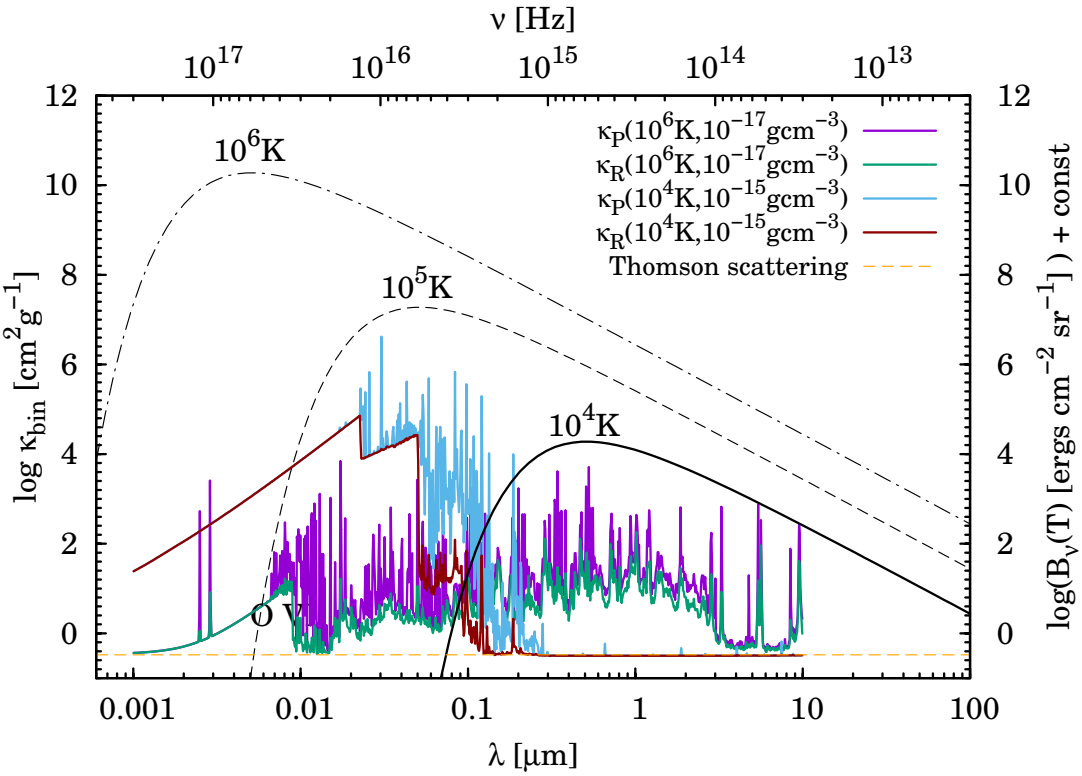


**Figure 5.2:** Same as Fig. 5.1 bue for $T = 6800$ K, $\varrho \approx 4.3 \times 10^{-16}$g cm$^{-3}$, $N_{\rm bins} = 10^3$. The black lines show the Planck functions (all shifred vertically by the same arbitrarial amount), the orangre dashed line - the Thomson scattering cross section.

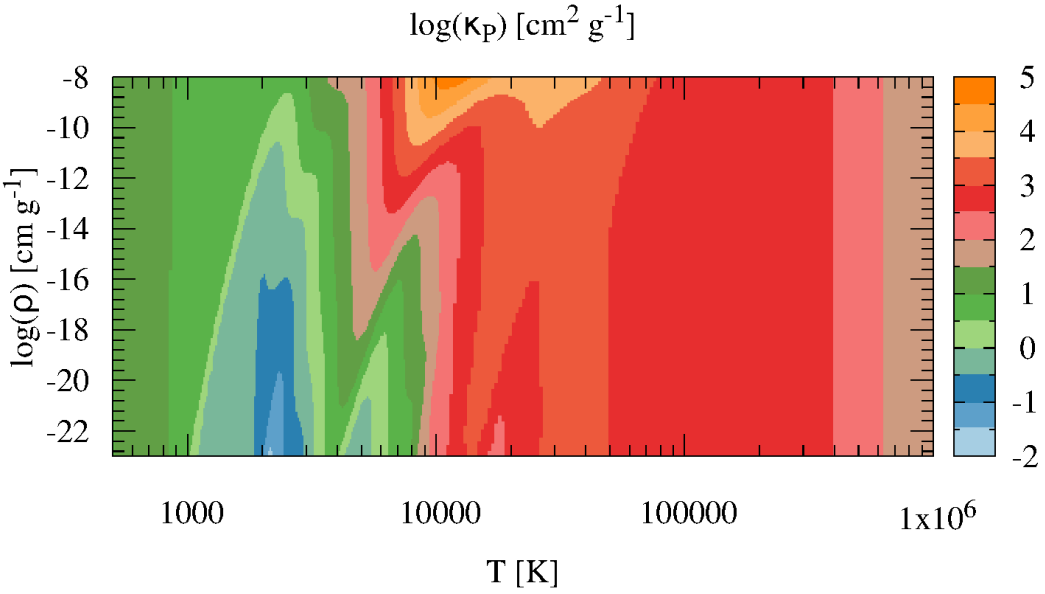


**Figure 5.3:** Planck mean opacity (colour coded) as recovered from the direct frequency averages.

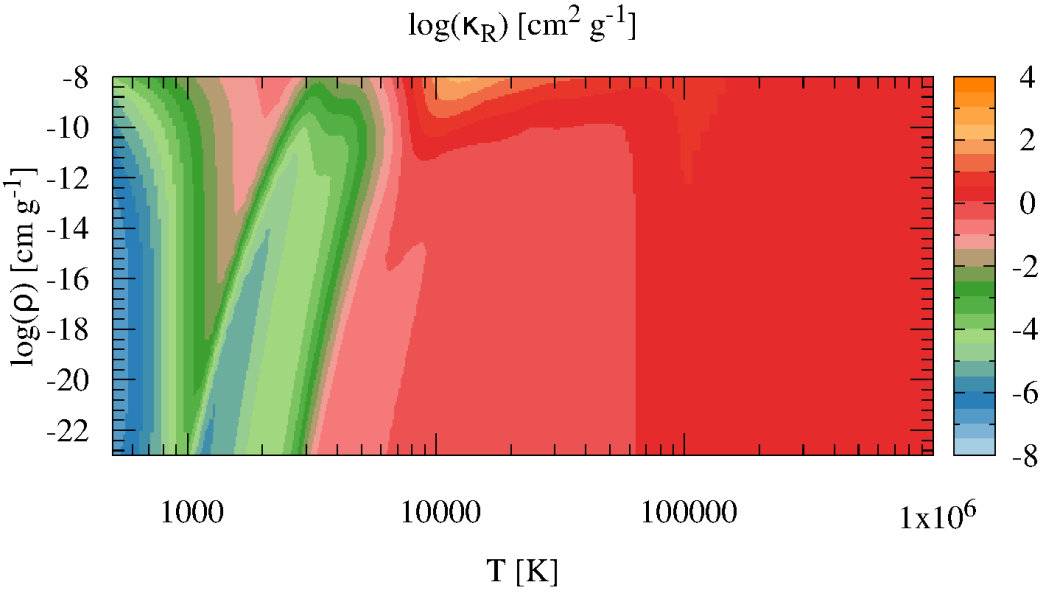


**Figure 5.4:** Planck mean opacity (colour coded) as recovered from the direct frequency averages.

*Never express yourself more clearly than you are able to think.*

Niels Bohr

# 6 Summary

Gas Opacity We calculated a new set of mean gas opacities assuming LTE and an ideal gas equation of state with a composition obtained from equilibrium chemistry for given atomic abundances. All the tables are freely available at the Strasbourg astronomical Data Center (the CDS, http://cdsweb.u-strasbg.fr/), as well as at http://www.mpia.de/~malygin. For the purpose of calculations we used the publicly available code DFSYNTHE [Castelli, 2005]. We covered the density and temperature ranges relevant for circumstellar environments. The means are tabulated in form of the Rosseland and the two-temperature Planck frequency averages on a grid of gas temperatures, gas densities (and radiation temperatures in the case of two-temperature Planck mean), and for three different metallicities: $[\mathrm{Me/H}] = -0.3, 0.0$, and $+0.3$. We argue that the two-temperature Planck mean is essential for proper treatment of radiative energy balance in optically thin circumstellar gaseous environments.

The part of the data that allows for comparison to other studies agrees with Ferguson et al. [2005]. We therefore conclude that our calculations are in line with the contemporary high-frequency resolution studies, which justifies that the convergence in gas opacity determinations has been achieved recently. The low-temperature - high-pressure part of our data provides a lower limit to the true opacity of a solar-composition dust-free gas, as inferred from the comparison to Freedman et al. [2008]. We claim the new opacities may be profitably utilised for gas temperature determination in

gaseous circumstellar environments. These would primarily correspond to the inner parts and atmospheres of accretion disks around forming stars as well as of passive disks around young stellar objects, circumstellar envelopes of pulsating stars, or upper irradiated parts of planetary atmospheres. In general, our data apply to any dust-depleted gaseous medium with a suitable range of thermodynamic parameters.

Solving radiative equilibrium in an optically thin gas may yield more than one equilibrium temperature solution. This occurs because of radiative instability owing to transitions between molecular and atomic phases in gas. From the perspective of temporal evolution, the radiative instability may lead to limit cycles in the equilibrium temperature profile. Hence, the embedded gaseous cocoons around forming stars may have coexisting different-temperature phases similar to the ISM large-scale structure. In addition, abrupt temporal variations in temperature of the falling gas are expected to occur during star formation. This can affect the accretion rate, similarly to how it happens in cataclysmic variables [Meyer, 1982]. The equilibrium temperature structure and its evolution will clearly affect the appearance of the dust-free interiors, although the question of how it alters the secular evolution of the host system (a massive proto-star) is yet to be addressed.

The degeneracy of the equilibrium temperature has at least one important numerical corollary: the radiative transfer modules relying on iterative temperature update schemes will not, in general, be able to provide convergence of the solution. The methods tracking the evolution of the temperature with time are therefore requisite for such modules.

The frequency-binned gas opacity well reproduce the mean opacities yet the use of the former will add to the flash-light effect in the frequency-resolved radiative transport in, e.g., a star formation numerical modelling. Such a simulation is currently being under preparation.

Our calculations of gas opacity reside within a simplified framework: equilibrium chemistry determines the relative abundances of the compounds, local thermodynamic equilibrium defines the level populations, we use simplified line damping treatment. The inclusion of non-equilibrium chemistry, non-LTE, and the effects of turbulence are the starting points for improvements.

Thermal Relaxation A simple recipe to compute the radiative relaxation time in protoplanetary discs is introduced. The relaxation time as a function of the perturbation wavelength, temperature and density is obtained by means of non-compressible linear analysis. There are two regimes of relaxation depending on the means the thermal energy evolves: the optically thick and the optically thin. First is determined by radiative diffusion, second – by thermal radiation. In comparison to previous studies, collisional decoupling is taken into account, both the Planck and the Rosseland tabulated opacities are used. The restriction of the flux limiter is discussed (Sect. 3.6.2). The optically thick regime can be both dynamically fast and slow ($\Omega t \lesseqgtr 1$), the optically thin one is dynamically fast if not limited by collisions. The fastest LTE relaxation is $\Omega t \sim 10^{-4}$ in a typical T

Tau disc. In numerical modelling, this recipe can be employed to evaluate the relaxation time of a grid cells (or SPH particle) based on its actual optical depth. This has applications for studying hydrodynamic and gravitational instabilities in the context of planet formation and transport in accretion discs, the core migration and planet-disc interaction modelling. Calculated maps of the relaxation time constrain the birthplaces of the hydrodynamic instabilities (Fig. 4.1). We find that the linear convective overstability (COV) can operate in a large volume of a T Tau disc possibly seeding initial noise for zombie vortices (ZVI). The vertical shear (Goldreich-Schubert-Fricke) instability incepts in a layer sandwiched between the sheets of the fastest growth of the COV. The ZVI can develop within $\pm 2$H inside 2 AU, where thermal ionization is yet inefficient to drive the MRI. Our Toomre $Q = 1$ disc model is unstable beyond $\approx 30$ AU. A one-in-lifetime fragmentation can occur as close as at 10 AU [Hopkins & Christiansen, 2013], but the issue requires dynamical modelling [Meru, 2015].

Conclusions Local variations in dust density in the CSM can make gas opacity important for the structure of this heterogeneous medium. This can influence the dynamics of the star and planet formation via accretion evolution. In case of massive stars, the frequency-dependent gas opacity is needed to accurately account for the radiative feedback. Further investigations of the impact of gas opacity on physics of accretion discs is certainly required.

# Acknowledgments

First thank goes to YHWH, then to his Song and beloved congregation and all the kind people on Earth (and, perhaps, beyond).

I thank to my family: my elvish princesses nuclear phycisist Lutienne Tinuvielle and our two pretty daughters – you give perspective to values of all the things; my father who taught me physics and whose qualities I am starting appreciating only now; my mother who taught me all the rest (but physics) and who may be soon diagnosed with cancer…; my grandfather whom I love at most…

This work started with the kindness of Thomas Henning, who invited me to MPIA after the official IMPRS deadline. It proceeded with a care of Hubert Klahr – not only the master of incompressible hydrodynamics but also a gifted teacher who can teach you Taylor columns, Eckman pumping, Couette flows, vortex generation, weather explanations, dust growth, side of the force, jedi plasma sword (oops, sorry) without you actually noticing you've been taught. Many more words to say call for brevity and silence: Hubert's contribution to this work (if not counting the typing) is key. Kees (aka Cornelius Petrus Dullemond) taught me a lot about radiative transfer, circumstellar discs, planet formation, hydrodynamics, teaching and interesting discussions.

O'k, I would like to thank all the student fellows. The list won't be complete. Special thank to Tristen Heyfield whose broad knowledge shared in discussions on simplectic methods, most-general forms of 4-tensors, k-trees, differential equations of special type (I still can't remember the name), carrots and fermentation during a chess game on the 30 bus continues to serve an inexhaustible source of inspiration for me. Tristen, you know you are in my heart. My gratitude to Rolf Kuiper can not be overestimated: you are by far the most fast-responding and ready-to-help person I have ever seen and will probably see in my short life. I suspect you are elvish too. Mario Flock, you not only helped me with my first PLUTO installation but has been always rewarding me with recognition of my opacity calculations ^_^ Your swift capturing of things that are not belonging to your subject (so far) both surprise and encouradge me. Kai-Martin Dittkrist and Gabriel-Dominique Marleau, so many discussions were held with you, which helped me to improve my habits (I am talking about keeping-windows-opened explained on a scientific ground) and my thesis. Kai-Martin,

we should gather for a pool tournament and memories. I will never forget your help with writing the German Abstract to this work in less then 5? minutes at 6 a.m. on 7$^{th}$ of January! Aiara, you helped me so many times that I owe you tons of chocolate (take at word!). Paul Mollière and Matheus Schulik, I am convenced you are the astrophycisists of the future, you will become the big shots, so keep pacing! BTW, I like your sense of humour. I thank you Michael Maseda for carefully and professionally proovereading my first paper. I am sorry for that stupid joke about the headphones. Anyways. Alex Golovin and Georgy Skorodumov, I am looking forward to meeting you in Coffee Nerd. I thank many-many other interesting people I met during my PhD and I want to beg pardon if I hearted someone (that's not including you, Hubert).

I thank the two referees for reading this not-easy-to-read peace of text and agreeing to be on my PhD brainstorming. I thank Christoph Mordasini and Luca Amendola for what I have learned from you and for your willingness to join those two on the known occasion. I would like to thank Neal Turner not only for keeping a vivid interest in my work but also for being a person of a rare humaneness on Earth.

Now, dear reader, if you have read all this, your brains have been well washed. And as always, thanks for washing.

*Logic will get you from A to B. Imagination will get you everywhere.*

Albert Einstein

# A

# Optically thick relaxation time

## A.1 Basic equations

To obtain a characteristic damping time of optically thick thermal perturbations, we start with the thermal energy evolution equation considering only radiative processes [see Kuiper et al., 2010b]

$$\partial_t \left( E_{\rm int} + E_{\rm R} \right) = -\nabla \vec{F}_{\rm R}. \tag{A.1}$$

Here $E_{\rm int}$ is the internal energy density of the gas, $E_{\rm R}$ the radiation energy density, $\vec{F}_{\rm R}$ the flux of the radiation energy density. In derivation of the optically thick time it is legitimate to assume that the temperature of the gas particles and the temperature of the photons of the ambient thermal field are always equal (see Sect. 3.6.4). This balance is provided through collisions between gas and dust particles, and entails quick collisional coupling: $t_{\rm coll} < t_{\rm diff}$, the condition furnished in the optically thick case by sufficiently high densities (see B). The internal energy density of the gas with mass density $\varrho$ and temperature $T$ is given by

$$E_{\rm int} = \varrho C_{\rm V} T \tag{A.2}$$

with $C_V$ being specific heat capacity at constant volume. The radiation energy density is defined by

$$E_R = aT^4, \tag{A.3}$$

where $a = 4\sigma/c$ is the radiation constant, and the radiation temperature $T$ has the same value as the thermodynamic gas temperature in the course of their mutual evolution. Use of Eq. (A.2) and Eq. (A.3) in the left-hand side of Eq. (A.1) yields

$$\partial_t \left(E_{int} + E_R\right) = 4aT^3 \left(1 + \frac{\varrho c_V}{4aT^3}\right) \partial_t T = 4aT^3 \left(\frac{3}{4} + \frac{1}{4}\eta^{-1}\right) \partial_t T \tag{A.4}$$

with $\eta = E_R/(E_R + E_{int})$. The flux of thermal radiation energy reads

$$\vec{F}_R = -D\nabla E_R. \tag{A.5}$$

In the framework of the flux-limited diffusion we write

$$D = \frac{\Lambda c}{\varkappa_R \varrho} \tag{A.6}$$

with $\varkappa_R$ being the Rosseland mean opacity, $c$ the speed of light, $\varrho$ the mass density, and $\Lambda$ the flux limiter [Levermore & Pomraning, 1981]. The gradient of the thermal radiation flux unveils

$$-\nabla\vec{F}_R = 4aT^3 D \times \left(\triangle T + \frac{3\left(\nabla T\right)^2}{T} + \vec{A}\cdot\nabla T\right) \tag{A.7}$$

with

$$\vec{A} = \frac{\nabla\varkappa_R}{\varkappa_R} + \frac{\nabla\varrho}{\varrho} = \nabla \ln \varkappa_R + \nabla \ln \varrho = \nabla \ln \varrho \left[1 + \varrho\partial \quad \ln \varkappa_R\right]. \tag{A.8}$$

Equilibrium temperature $T_0$ satisfies

$$4aT_0^3 D \times \left(\triangle T_0 + \frac{3\left(\nabla T_0\right)^2}{T_0} + \vec{A}\cdot\nabla T_0\right) = 0. \tag{A.9}$$

This equilibrium temperature is defined via irradiation and internal hydrodynamic processes. In our subsequent numerical example, we consider a hydrostatic equilibrium disc structure (Sect. 3.4). We substitute Eq. (A.4) and Eq. (A.7) into Eq. (A.1) to obtain the temperature evolution equation

$$4aT^3 f^{-1}\partial_t T = 4aT^3 D \times \left(\triangle T + \frac{3\left(\nabla T\right)^2}{T} + \vec{A}\cdot\nabla T\right), \tag{A.10}$$

where we designated

$$f = \partial_T E_R/\partial_T \left(E_{int} + E_R\right) = 4\eta/\left(1 + 3\eta\right) \tag{A.11}$$

following Kuiper et al. [2010b].

## A.2 Linear analysis

Substituting $T = T_0 + \delta T$ with equilibrium temperature $T_0$ satisfying (A.9), we linearise Eq. (A.10):

$$f^{-1}\delta\dot{T} = D\left(\triangle\delta T - \frac{3\left(\nabla T_0\right)^2}{T_0}\frac{\delta T}{T_0} + \left(\frac{6\nabla T_0}{T_0} + \vec{A}\right)\cdot\nabla\delta T\right). \tag{A.12}$$

Let

$$k = \frac{2\pi}{\lambda} \tag{A.13}$$

be a wavenumber of the Fourier mode with spatial alignment along direction $x$ of the fastest radiative heat transport (not necessarily the vertical direction, but most likely). A dissipation time of this mode is then found by employing the Fourier ansatz $\delta T_k = \delta T_k^0 \exp\left(-i\vec{k}\vec{x} + i\omega t\right) + c.c.$:

$$t_{\text{thick}} = \frac{(Df)^{-1}}{k^2 + 3\left(\nabla \ln T\right)^2 - \vec{A}'\nabla T}. \tag{A.14}$$

Here $\vec{A}' = \partial_T\left[\nabla \ln \varrho\left(1 + \varrho\partial \quad \ln \varkappa_{\text{R}}\right)\right]$ is a partial derivative of Eq. (A.8) with respect to temperature, and

$$\tilde{D} = Df \tag{A.15}$$

the effective diffusion coefficient. If the wavenumber is small (or the density fluctuations within it are significant), $|\nabla_z \varrho|\,\varrho^{-1} > k$, we shall perform averaging over $\lambda$

$$t_{\text{thick}} = \frac{\left\langle\left(\tilde{D}\right)^{-1}\right\rangle}{k^2 + 3\left\langle\left(\nabla \ln T\right)^2\right\rangle - \left\langle\vec{A}'\nabla T\right\rangle}. \tag{A.16}$$

This averaging makes the analysis essentially non-local, but we find the differences between $\langle t_{\text{thick}}\rangle$ and $t_{\text{thick}}$ significant in disc atmosphere. This is owing to the underlying (Gaussian) density profile. Because the Rosseland mean for dust is a moderately varying function of density $|\partial \quad \varkappa_{\text{R}}| \ll \varrho^{-1}\varkappa_{\text{R}}$, we approximate $\vec{A}' = \partial_T\nabla \ln \varrho$. For an adiabatic equation of state $\varrho \propto T$ one finds $\vec{A}'\nabla T = -\gamma\left(\nabla \ln T\right)^2 + \nabla\gamma\nabla \ln T$. It is, therefore, beneficiary to separate the terms proportional to the first and second power of $\nabla \ln T$ in the denominator. We will call

$$k_{\text{T}} = \left(3 + \gamma\right)^{1/2}\nabla \ln T \tag{A.17}$$

the equilibrium temperature wavenumber, and $k_A = (\nabla\gamma\nabla T)^{1/2}$ the adiabatic wavenumber. We rewrite

$$t_{\text{thick}} = \frac{\left(\tilde{D}\right)^{-1}}{k^2 + k_T^2 + k_A^2}. \tag{A.18}$$

The adiabatic index varies over the disc volume because of changes in relative abundances of gas-phase species, which in turn is dictated by a complicated network of chemical reactions, grains evolution and other dynamical processes [Henning & Semenov, 2013]. In a hydrostatic picture, we argue, the factor $\nabla\gamma$ makes $k_A$ negligible in favour of the thermal wavenumber $k_T$. Indeed, locally evaluated, the term is non-zero only for specific temperature and density values, i.e. in some narrow spatial regions (in the limit, on 2D surfaces) in the disc. The averaging over the wavelengths larger than those regions would smear out the non-trivial values. The equation reduces to

$$t_{\text{thick}} = \frac{\left(\tilde{D}\right)^{-1}}{k^2 + k_T^2}. \tag{A.19}$$

The thermal wavenumber $k_T$ is determined by the characteristic length scale of equilibrium temperature gradient. In a vertically isothermal radially stratified disc with $T \propto r^{-q}$ this term may be estimated as $\nabla T/T \sim -qh\mathrm{H}^{-1}$, with H being the local pressure scale height, and $h$ the local aspect ratio usually of the order of 0.05. Thus, we set

$$t_{\text{thick}} = \frac{\left\langle\tilde{D}\right\rangle^{-1}}{k^2} = t_{\text{diff}}. \tag{A.20}$$

For high-frequency modes, $\lambda \ll \mathrm{H}$, the equilibrium thermal wavenumber is negligible in favour of the wavenumber of the mode itself. For the low-frequency mode ($\lambda \geqslant \mathrm{H}$), Eq. A.20 holds true for giometrically thin discs (i.e., those with small aspect ratios). Hence, the optically thick relaxation time evaluates the diffusion time of the excess thermal photons over the mode wavelength. For the application cases of vertically isothermal disc, it is legitimate to permanently set

$$\nabla T = 0. \tag{A.21}$$

In this case, the relaxation time of a "thick" mode depends on its wavenumber $k$, the radiative diffusion coefficient $D$, and the ratio $f$, which is smaller than unity in this regime (see Sect. A.3).

## A.3 Energy or temperature evolution time?

Dividing Eq. (A.4) by the total thermal energy $E_{\text{tot}} = E_R + E_{\text{int}}$ gives a relation between the energy and temperature evolution times

$$t_E = (1 + 3\eta)^{-1} \times t_T. \tag{A.22}$$

If $\eta \ll 1$, the two times are equal up to $O(3\eta)$. The "critical" density $\varrho_{\rm cr} = aT^3/c_{\rm V}$ at which the radiation energy density equals the internal energy density is as low as

$$\varrho_{\rm cr} = 1.3 \times 10^{-16} \left( \frac{T}{100\ {\rm K}} \right)^3\ {\rm g\ cm^{-3}}. \tag{A.23}$$

For instance, $\varrho_{\rm cr} \approx 10^{-15}$ g cm$^{-3}$ at 300 K, that is several orders of magnitude below the typical midplane values for a PPD in T Tau phase. We find $\eta$ between $10^{-5}$ and $10^{-3}$ within the optically thick regions in the fiducial disc model.

# B

# Optically thin relaxation time

Optically thin relaxation includes two processes: deliver of the thermal excess to the emitters and radiation from those. We assume that the first one is due to collisions, the second one is the LTE emission. The net relaxation time is set by the slower process (Eq. 3.6). We take into account two type of emitters: dust and gas particles.

## B.1 Thermal emission time

Consider the following energy balance equation:

$$C_V \dot{T} = \mathcal{Q}^+ - \mathcal{Q}^-, \tag{B.1}$$

where the terms $\mathcal{Q}^{+/-}$ designate the specific (per unit mass) heating or cooling due to the perturbation on top of an equilibrium temperature field. The emission rate of matter at equilibrium temperature $T$ is proportional to the Planck mean opacity $\varkappa_P$ at that temperature (Kirchhoff's law). The perturbed internal energy evolves due to radiative heating and cooling

$$C_V \dot{\delta T} = -2\varkappa_P \sigma \left[ (T + \delta T)^4 - (T - \delta T)^4 \right], \tag{B.2}$$

where $\delta T$ is the amplitude of temperature perturbation. Substituting a Fourier mode $(T - T_\circ)_k = \delta T_k = \delta T_k^\circ \exp\left(-i\vec{k}\vec{x} - i\omega t\right)$, we linearise

$$C_V \delta\dot{T} = -16\varkappa_P \sigma T^4 \frac{\delta T}{T}. \tag{B.3}$$

This implies the evolutionary time

$$t_{\text{emit}} = \frac{C_V}{16\varkappa_P \sigma T^3}. \tag{B.4}$$

The time is independent of the perturbation wavenumber. This thermal emission time is the lower limit for radiative relaxation time: given material at given temperature can not radiatively relax faster because the relaxation process operates at maximum (LTE) emissivity.

## B.2 Collisional coupling

In PPDs, relative velocities in both dust-to-gas and gas-to-gas collisions are attributed to the thermal motions of the gas particles

$$v_{\text{coll}} = v_{\text{th}}^g = \sqrt{\frac{3k_B T}{\mu}}, \tag{B.5}$$

where $\mu$ is the mean molecular weight, $k_B$ the Boltzmann constant. The mean time between two subsequent collisions is

$$t_{\text{coll}} = \frac{1}{n\sigma_c v_{\text{coll}}}, \tag{B.6}$$

where $\sigma_c$ is the collisional cross section with the targets of number density $n$.

## B.3 Dust-to-gas collisions

Underlying size distribution in Semenov et al. [2003] opacity model is an MRN function with spectral slope of 3.5 [Mathis et al., 1977] modified by setting the maximum grain size to 5 $\mu$m [Pollack et al., 1985]:

$$n(a) \propto a^{-3.5},\ a_- = 0.005\,\mu\text{m},\ a_+ = 5\,\mu\text{m} \tag{B.7}$$

This gives the effective collisional cross section $\sigma \approx \pi a_+ a_- \approx 1.5 \times 10^{-9}$ cm$^2$.

## B.4 Gas-to-gas collisions at low temperatures

At different temperatures, the emissivity of the gas is supplied by different species. In LTE, the most efficiently radiating species can be found by comparing their relative contributions to the total

Planck mean

$$w^i = \frac{\varkappa_{\rm P}^i}{\varkappa_{\rm P}},\ \sum_i w^i = 1. \tag{B.8}$$

Here $i$ labels the species (e.g. CO, $H_2O$, TiO, $NH_3$, etc.), and

$$\varkappa_{\rm P}^i = \frac{\int \varkappa_\nu^i B_\nu\, d\nu}{\int B_\nu\, d\nu} \tag{B.9}$$

is a contribution to the Planck mean from specie $i$. The effective coupling time to radiative gas species can be estimated as

$$t_{\rm coll}^g = \frac{1}{\sum_i w^i t_i^{-1}}. \tag{B.10}$$

At the temperatures of interest, the most abundant species, $H_2$ and He, are not efficient emitters in terms of (B.9), but they store the bulk of thermal energy. The rest of the matter can be modelled as a sort of radiating particles satisfying

$$\varkappa_{\rm P}' = \varkappa_{\rm P}. \tag{B.11}$$

Coupling time (B.10) is then approximated as collision time

$$t_{\rm coll}^g = t_{\rm coll}' = \frac{1}{n'\sigma_{\rm nn} v_{\rm th}} \tag{B.12}$$

with the effective neutral-neutral collisional cross section $\sigma_{\rm nn}$. We estimate

$$\begin{aligned}\Omega t_{\rm coll}^g = 1.6\times 10^{-6} \left(\frac{f}{10^{-2}}\right)^{-1} \left(\frac{\sigma_{\rm nn}}{10^{-17}\ {\rm cm}^2}\right)^{-1} \times \\ \left(\frac{\varrho}{10^{-10}\ {\rm gcm}^{-3}}\right)^{-1} \left(\frac{T}{100\ {\rm K}}\right)^{-1/2} \left(\frac{r}{10\ {\rm AU}}\right)^{-3/2},\end{aligned} \tag{B.13}$$

where $f = n'/n_{\rm gas}$ is the number fraction of the radiating species. In our calculations, we put $f = 10^{-2}$ and $\sigma_{\rm nn} = 8.5\times 10^{-17}$ cm$^2$.

# Nomenclature

| | |
|---|---|
| ALMA | Atacama Large Milimiter Array |
| ATLAS | Kurucz' program for modelling stellar atmospheres (Fortran) |
| AU | Astronomical Unit |
| b-b | bound-bound |
| b-f | bound-free, e.g. ionisation |
| CA | Core Accretion |
| CDS | Strasbourg Data Centre |
| COV | COnvective Overstability |
| CSM | CircumStellar Medium |
| DFSYNTHE | a Fortran code for calculating OPDFs under unix |
| f-b | bound-bound, e.g. recombination |
| f-f | free-free, e.g. scattering |
| FARGO | FAst Rotating Gaseous Objects (a numerical algorithm) |
| FLD | Flux-Limited Diffusion |
| GI | Gravitational Instability |
| GSF | Goldreich-Shubert-Fricke Instability |
| HD | HydroDynamics |
| IR | Infra Red |

| | |
|---|---|
| ISM | InterStellar Medium |
| KAPPA | a modification of DFSYNTHE [Malygin et al., 2014] |
| LTE | Local Thermodynamic Equilibrium |
| MRI | Magneto-Rotational Instability |
| NIR | Near Infra Red |
| OPDF | Opacity Probability Distribution Function |
| OS | Opacity Sampling |
| PPD | ProtoPlanetary Disc |
| RT | Radiative Transfer |
| SAM | Stellar Atmosphere Models [a Fortran code, e.g. Pavlenko, 1997a] |
| SBI | Subcritical Baroclinic Instability |
| SPH | Smoothed Particle Hydrodynamics |
| UV | Ultra Violet |
| VLT | Very Large Telescope |
| VSI | Vertical Shear Instability (aka GSF) |
| ZVI | Zombie Vortex Instability |

# Listing of figures

*I do not mind if you think slowly, but I do object when you publish more quickly than you think."*

Wolfgang Pauli

# References


Adams, F. C. & Benz, W. (1992). Gravitational Instabilties in Circumstellar Disks and the Formation of Binary Companions. In H. A. McAlister & W. I. Hartkopf (Eds.), *IAU Colloq. 135: Complementary Approaches to Double and Multiple Star Research*, volume 32 of *Astronomical Society of the Pacific Conference Series* (pp. 185).

ALMA Partnership, Brogan, C. L., Pérez, L. M., & al., e. (2015). The 2014 ALMA Long Baseline Campaign: First Results from High Angular Resolution Observations toward the HL Tau Region. *ApJ*, 808, L3.

Andrews, S. M., Wilner, D. J., Hughes, A. M., Qi, C., & Dullemond, C. P. (2009). Protoplanetary Disk Structures in Ophiuchus. *ApJ*, 700, 1502–1523.

Arlt, R. & Urpin, V. (2004). Simulations of vertical shear instability in accretion discs. *A&A*, 426, 755–765.

Armitage, P. J., Livio, M., & Pringle, J. E. (2001). Episodic accretion in magnetically layered protoplanetary discs. *MNRAS*, 324, 705–711.

Baehr, H. & Klahr, H. (2015). The Role of the Cooling Prescription for Disk Fragmentation: Numerical Convergence & Critical Cooling Parameter in Self-Gravitating Disks. *ArXiv e-prints*.

Balbus, S. A. & Hawley, J. F. (1991). A powerful local shear instability in weakly magnetized disks. I - Linear analysis. II - Nonlinear evolution. *ApJ*, 376, 214–233.

Balbus, S. A. & Hawley, J. F. (1998). Instability, turbulence, and enhanced transport in accretion disks. *Reviews of Modern Physics*, 70, 1–53.

Balbus, S. A. & Papaloizou, J. C. B. (1999). On the Dynamical Foundations of $\alpha$ Disks. *ApJ*, 521, 650–658.

Balmer, J. J. (1885). Notiz über die Spectrallinien des Wasserstoffs. *Annalen der Physik*, 261, 80–87.

Barber, R. J., Tennyson, J., Harris, G. J., & Tolchenov, R. N. (2006). A high-accuracy computed water line list. *MNRAS*, 368, 1087–1094.

Barge, P. & Sommeria, J. (1995). Did planet formation begin inside persistent gaseous vortices? *A&A*, 295, L1–L4.

Barker, A. J. & Latter, H. N. (2015). On the vertical-shear instability in astrophysical discs. *MNRAS*, 450, 21–37.

Baruteau, C. & Masset, F. (2008). On the Corotation Torque in a Radiatively Inefficient Disk. *ApJ*, 672, 1054–1067.

Bate, M. R. (1998). Collapse of a Molecular Cloud Core to Stellar Densities: The First Three-dimensional Calculations. *ApJ*, 508, L95–L98.

Beckwith, S. V. W., Henning, T., & Nakagawa, Y. (2000). Dust Properties and Assembly of Large Particles in Protoplanetary Disks. *Protostars and Planets IV*, (pp. 533).

Bell, K. R. & Lin, D. N. C. (1994). Using FU Orionis outbursts to constrain self-regulated protostellar disk models. *ApJ*, 427, 987–1004.

Beltrán, M. T., Cesaroni, R., Neri, R., Codella, C., Furuya, R. S., Testi, L., & Olmi, L. (2004). Rotating Disks in High-Mass Young Stellar Objects. *ApJ*, 601, L187–L190.

Bergin, E. A., Cleeves, L. I., Gorti, U., Zhang, K., Blake, G. A., Green, J. D., Andrews, S. M., Evans, II, N. J., Henning, T., Öberg, K., Pontoppidan, K., Qi, C., Salyk, C., & van Dishoeck, E. F. (2013). An old disk still capable of forming a planetary system. *Nature*, 493, 644–646.

Bertin, G. (1997). Self-regulated Accretion Disks. *ApJ*, 478, L71–L74.

Beuther, H., Klessen, R. S., Dullemond, C. P., & Henning, T. (2014). Protostars and Planets VI. *Protostars and Planets VI*.

Birnstiel, T., Klahr, H., & Ercolano, B. (2012). A simple model for the evolution of the dust population in protoplanetary disks. *A&A*, 539, A148.

Blum, J. & Münch, M. (1993). Experimental investigations on aggregate-aggregate collisions in the early solar nebula. *Icarus*, 106, 151.

Böhm, K.-H. (1954). Die Temperaturschichtung der Sonnenatmosphäre im nichtgrauen Strahlungsgleichgewicht. Mit 8 Textabbildungen. *ZAp*, 34, 182.

Bohr, N. (1913a). On the constitution of atoms and molecules, Part I. The binding of electrons by positive nuclei. *Philosophical Magazine*, 26, 1–25.

Bohr, N. (1913b). On the constitution of atoms and molecules. Part II. Systems containing only a single nucleus. *Philosophical Magazine*, 26, 476–502.

Bohr, N. (1913c). On the constitution of atoms and molecules. Part III. Systems containing several nuclei. *Philosophical Magazine*, 26, 857–875.

Boley, A. C. (2009). The Two Modes of Gas Giant Planet Formation. *ApJ*, 695, L53–L57.

Boley, A. C., Mejía, A. C., Durisen, R. H., Cai, K., Pickett, M. K., & D'Alessio, P. (2006). The Thermal Regulation of Gravitational Instabilities in Protoplanetary Disks. III. Simulations with Radiative Cooling and Realistic Opacities. *ApJ*, 651, 517–534.

Boss, A. P. (1984). Angular momentum transfer by gravitational torques and the evolution of binary protostars. *MNRAS*, 209, 543–567.

Boss, A. P. (1997). Giant planet formation by gravitational instability. *Science*, 276, 1836–1839.

Boss, A. P. (1998). Evolution of the Solar Nebula. IV. Giant Gaseous Protoplanet Formation. *ApJ*, 503, 923–937.

Boss, A. P. (2000). Possible Rapid Gas Giant Planet Formation in the Solar Nebula and Other Protoplanetary Disks. *ApJ*, 536, L101–L104.

Boss, A. P. (2001). Gas Giant Protoplanet Formation: Disk Instability Models with Thermodynamics and Radiative Transfer. *ApJ*, 563, 367–373.

Boss, A. P. (2002). Evolution of the Solar Nebula. V. Disk Instabilities with Varied Thermodynamics. *ApJ*, 576, 462–472.

Boss, A. P. (2003). Rapid Formation of Outer Giant Planets by Disk Instability. *ApJ*, 599, 577–581.

Boss, A. P. (2004). Convective Cooling of Protoplanetary Disks and Rapid Giant Planet Formation. *ApJ*, 610, 456–463.

Brauer, F., Dullemond, C. P., & Henning, T. (2008). Coagulation, fragmentation and radial motion of solid particles in protoplanetary disks. *A&A*, 480, 859–877.

Brinch, C. & Jørgensen, J. K. (2013). Interplay between chemistry and dynamics in embedded protostellar disks. *A&A*, 559, A82.

Burrows, A., Marley, M. S., & Sharp, C. M. (2000). The Near-Infrared and Optical Spectra of Methane Dwarfs and Brown Dwarfs. *ApJ*, 531, 438–446.

Burrows, A. & Volobuyev, M. (2003). Calculations of the Far-Wing Line Profiles of Sodium and Potassium in the Atmospheres of Substellar-Mass Objects. *ApJ*, 583, 985–995.

Butler, R. P. & Marcy, G. W. (1996). A Planet Orbiting 47 Ursae Majoris. *ApJ*, 464, L153.

Butler, R. P., Marcy, G. W., Williams, E., Hauser, H., & Shirts, P. (1997). Three New "51 Pegasi-Type" Planets. *ApJ*, 474, L115–L118.

Cai, K., Durisen, R. H., Michael, S., Boley, A. C., Mejía, A. C., Pickett, M. K., & D'Alessio, P. (2006). The Effects of Metallicity and Grain Size on Gravitational Instabilities in Protoplanetary Disks. *ApJ*, 636, L149–L152.

Cai, K., Pickett, M. K., Durisen, R. H., & Milne, A. M. (2010). Giant Planet Formation by Disk Instability: A Comparison Simulation with an Improved Radiative Scheme. *ApJ*, 716, L176–L180.

Callanan, P. J. (1993). Accretion disks in low-mass X-ray binaries. *PASP*, 105, 961–965.

Cameron, A. G. W. (1978). Physics of the primitive solar accretion disk. *Moon and Planets*, 18, 5–40.

Cassen, P. & Woolum, D. S. (1996). Radiatively Damped Density Waves in Optically Thick Protostellar Disks. *ApJ*, 472, 789.

Castelli, F. (2005). DFSYNTHE: how to use it. *Memorie della Societa Astronomica Italiana Supplementi*, 8, 34.

Cesaroni, R. (2002). Disks and jets in high-mass young stellar objects. *Highlights of Astronomy*, 12, 156–158.

Chabrier, G., Johansen, A., Janson, M., & Rafikov, R. (2014). Giant Planet and Brown Dwarf Formation. *Protostars and Planets VI*, (pp. 619–642).

Chandrasekhar, S. (1935). The radiative equilibrium of the outer layers of a star, with special reference to the blanketing effect of the reversing layer. *MNRAS*, 96, 21.

Chini, R., Hoffmeister, V., Kimeswenger, S., Nielbock, M., Nürnberger, D., Schmidtobreick, L., & Sterzik, M. (2004). The formation of a massive protostar through the disk accretion of gas. *Nature*, 429, 155–157.

Cieza, L. A. (2015). The Structure and Evolution of Protoplanetary Disks: an infrared and submillimeter view. *ArXiv e-prints*.

Cochran, W. D., Hatzes, A. P., Butler, R. P., & Marcy, G. W. (1997). The Discovery of a Planetary Companion to 16 Cygni B. *ApJ*, 483, 457–463.

Cossins, P., Lodato, G., & Clarke, C. J. (2009). Characterizing the gravitational instability in cooling accretion discs. *MNRAS*, 393, 1157–1173.

Cuzzi, J. N., Dobrovolskis, A. R., & Champney, J. M. (1993). Particle-gas dynamics in the midplane of a protoplanetary nebula. *Icarus*, 106, 102.

Dessart, L., Hillier, D. J., Blondin, S., & Khokhlov, A. (2014). Critical ingredients of Type Ia supernova radiative-transfer modelling. *MNRAS*, 441, 3249–3270.

Dittkrist, K.-M., Mordasini, C., Klahr, H., Alibert, Y., & Henning, T. (2014). Impacts of planet migration models on planetary populations. Effects of saturation, cooling and stellar irradiation. *A&A*, 567, A121.

Dittrich, K., Klahr, H., & Johansen, A. (2013). Gravoturbulent Planetesimal Formation: The Positive Effect of Long-lived Zonal Flows. *ApJ*, 763, 117.

Durisen, R. H., Boss, A. P., Mayer, L., Nelson, A. F., Quinn, T., & Rice, W. K. M. (2007). Gravitational Instabilities in Gaseous Protoplanetary Disks and Implications for Giant Planet Formation. *Protostars and Planets V*, (pp. 607–622).

Durisen, R. H., Cai, K., Mejía, A. C., & Pickett, M. K. (2005). A hybrid scenario for gas giant planet formation in rings. *Icarus*, 173, 417–424.

Durisen, R. H., Gingold, R. A., Tohline, J. E., & Boss, A. P. (1986). Dynamic fission instabilities in rapidly rotating N = 3/2 polytropes - A comparison of results from finite-difference and smoothed particle hydrodynamics codes. *ApJ*, 305, 281–308.

Dutrey, A., Semenov, D., Chapillon, E., Gorti, U., Guilloteau, S., Hersant, F., Hogerheijde, M., Hughes, M., Meeus, G., Nomura, H., Piétu, V., Qi, C., & Wakelam, V. (2014). Physical and Chemical Structure of Planet-Forming Disks Probed by Millimeter Observations and Modeling. *Protostars and Planets VI*, (pp. 317–338).

Dzyurkevich, N., Turner, N. J., Henning, T., & Kley, W. (2013). Magnetized Accretion and Dead Zones in Protostellar Disks. *ApJ*, 765, 114.

Ferguson, J. W., Alexander, D. R., Allard, F., Barman, T., Bodnarik, J. G., Hauschildt, P. H., Heffner-Wong, A., & Tamanai, A. (2005). Low-Temperature Opacities. *ApJ*, 623, 585–596.

Forgan, D., Rice, K., Cossins, P., & Lodato, G. (2011). The nature of angular momentum transport in radiative self-gravitating protostellar discs. *MNRAS*, 410, 994–1006.

Fraunhofer, J. (1817). Bestimmung des Brechungs- und des Farbenzerstreungs-Vermögens verschiedener Glasarten, in Bezug auf die Vervollkommnung achromatischer Fernröhre. *Annalen der Physik*, 56, 264–313.

Freedman, R. S., Marley, M. S., & Lodders, K. (2008). Line and Mean Opacities for Ultracool Dwarfs and Extrasolar Planets. *ApJS*, 174, 504–513.

Gammie, C. F. (1996). Layered Accretion in T Tauri Disks. *ApJ*, 457, 355.

Gammie, C. F. (2001). Nonlinear Outcome of Gravitational Instability in Cooling, Gaseous Disks. *ApJ*, 553, 174–183.

Goldreich, P. & Lynden-Bell, D. (1965). II. Spiral arms as sheared gravitational instabilities. *MNRAS*, 130, 125.

Goodman, J. & Pindor, B. (2000). Secular Instability and Planetesimal Formation in the Dust Layer. *Icarus*, 148, 537–549.

Grevesse, N. & Sauval, A. J. (1998). Standard Solar Composition. *Space Sci. Rev.*, 85, 161–174.

Güttler, C., Blum, J., Zsom, A., Ormel, C. W., & Dullemond, C. P. (2010). The outcome of protoplanetary dust growth: pebbles, boulders, or planetesimals?. I. Mapping the zoo of laboratory collision experiments. *A&A*, 513, A56.

Haghighipour, N. & Boss, A. P. (2003a). On Gas Drag-Induced Rapid Migration of Solids in a Nonuniform Solar Nebula. *ApJ*, 598, 1301–1311.

Haghighipour, N. & Boss, A. P. (2003b). On Pressure Gradients and Rapid Migration of Solids in a Nonuniform Solar Nebula. *ApJ*, 583, 996–1003.

Hartmann, J. (1904). Investigations on the spectrum and orbit of delta Orionis. *ApJ*, 19, 268–286.

Helling, C. & Lucas, W. (2009). Gas-phase mean opacities for varying [M/H], N/O and C/O. *MNRAS*, 398, 985–994.

Helling, C., Winters, J. M., & Sedlmayr, E. (2000). Circumstellar dust shells around long-period variables. VII. The role of molecular opacities. *A&A*, 358, 651–664.

Henning, T. & Semenov, D. (2013). Chemistry in Protoplanetary Disks. *Chemical Reviews*, 113, 9016–9042.

Henning, T. & Stognienko, R. (1996). Dust opacities for protoplanetary accretion disks: influence of dust aggregates. *A&A*, 311, 291–303.

Hirose, S. (2015). Magnetic Turbulence and Thermodynamics in the Inner Region of Protoplanetary Discs. *ArXiv e-prints*.

Hopkins, P. F. & Christiansen, J. L. (2013). Turbulent Disks are Never Stable: Fragmentation and Turbulence-promoted Planet Formation. *ApJ*, 776, 48.

Inaba, S., Wetherill, G. W., & Ikoma, M. (2003). Formation of gas giant planets: core accretion models with fragmentation and planetary envelope. *Icarus*, 166, 46–62.

Isella, A., Pérez, L. M., Carpenter, J. M., Ricci, L., Andrews, S., & Rosenfeld, K. (2013). An Azimuthal Asymmetry in the LkH$\alpha$ 330 Disk. *ApJ*, 775, 30.

Isella, A., Testi, L., & Natta, A. (2006). Large dust grains in the inner region of circumstellar disks. *A&A*, 451, 951–959.

Joergens, V., Bonnefoy, M., Liu, Y., Bayo, A., Wolf, S., Chauvin, G., & Rojo, P. (2013). OTS 44: Disk and accretion at the planetary border. *A&A*, 558, L7.

Johansen, A., Andersen, A. C., & Brandenburg, A. (2004). Simulations of dust-trapping vortices in protoplanetary discs. *A&A*, 417, 361–374.

Johansen, A., Blum, J., Tanaka, H., Ormel, C., Bizzarro, M., & Rickman, H. (2014). The Multifaceted Planetesimal Formation Process. *Protostars and Planets VI*, (pp. 547–570).

Johansen, A., Brauer, F., Dullemond, C., Klahr, H., & Henning, T. (2008). A coagulation-fragmentation model for the turbulent growth and destruction of preplanetesimals. *A&A*, 486, 597–611.

Johansen, A., Klahr, H., & Henning, T. (2006). Gravoturbulent Formation of Planetesimals. *ApJ*, 636, 1121–1134.

Johansen, A., Klahr, H., & Henning, T. (2011). High-resolution simulations of planetesimal formation in turbulent protoplanetary discs. *A&A*, 529, A62.

Johansen, A., Youdin, A., & Klahr, H. (2009). Zonal Flows and Long-lived Axisymmetric Pressure Bumps in Magnetorotational Turbulence. *ApJ*, 697, 1269–1289.

Johnson, B. M. & Gammie, C. F. (2003). Nonlinear Outcome of Gravitational Instability in Disks with Realistic Cooling. *ApJ*, 597, 131–141.

Johnson, B. M. & Gammie, C. F. (2005). Vortices in Thin, Compressible, Unmagnetized Disks. *ApJ*, 635, 149–156.

Johnston, K. G., Robitaille, T. P., Beuther, H., Linz, H., Boley, P., Kuiper, R., Keto, E., Hoare, M. G., & van Boekel, R. (2015). A Keplerian-like disk around the forming O-type star AFGL 4176. *ArXiv e-prints*.

Kalas, P., Graham, J. R., Chiang, E., Fitzgerald, M. P., Clampin, M., Kite, E. S., Stapelfeldt, K., Marois, C., & Krist, J. (2008). Optical Images of an Exosolar Planet 25 Light-Years from Earth. *Science*, 322, 1345–.

Kamp, I. & van Zadelhoff, G.-J. (2001). On the gas temperature in circumstellar disks around A stars. *A&A*, 373, 641–656.

Kirchhoff, G. & Bunsen, R. (1860). Chemische Analyse durch Spectralbeobachtungen. *Annalen der Physik*, 186, 161–189.

Klahr, H. (2003). The Formation of a Planet in the Eye of a Hurricane - Vorticity Generation via the Global Baroclinic Instability in Accretion Disks. In D. Deming & S. Seager (Eds.), *Scientific Frontiers in Research on Extrasolar Planets*, volume 294 of *Astronomical Society of the Pacific Conference Series* (pp. 277–280).

Klahr, H. (2004). The Global Baroclinic Instability in Accretion Disks. II. Local Linear Analysis. *ApJ*, 606, 1070–1082.

Klahr, H. & Bodenheimer, P. (2006). Formation of Giant Planets by Concurrent Accretion of Solids and Gas inside an Anticyclonic Vortex. *ApJ*, 639, 432–440.

Klahr, H. & Brandner, W. (2006). *Planet Formation*.

Klahr, H. & Hubbard, A. (2014). Convective Overstability in Radially Stratified Accretion Disks under Thermal Relaxation. *ApJ*, 788, 21.

Klahr, H. H. & Bodenheimer, P. (2003). Turbulence in Accretion Disks: Vorticity Generation and Angular Momentum Transport via the Global Baroclinic Instability. *ApJ*, 582, 869–892.

Klahr, H. H. & Henning, T. (1997). Particle-Trapping Eddies in Protoplanetary Accretion Disks. *Icarus*, 128, 213–229.

Klahr, H. H. & Lin, D. (2015). The influence of opacity on the gas accretion of planetary embryos and their migration behaviour. *IAU General Assembly*, 22, 57733.

Kley, W., Bitsch, B., & Klahr, H. (2009). Planet migration in three-dimensional radiative discs. *A&A*, 506, 971–987.

Kley, W. & Crida, A. (2008). Migration of protoplanets in radiative discs. *A&A*, 487, L9–L12.

Kondratko, P. T., Greenhill, L. J., & Moran, J. M. (2005). Evidence for a Geometrically Thick Self-Gravitating Accretion Disk in NGC 3079. *ApJ*, 618, 618–634.

Korycansky, D. G. & Pollack, J. B. (1993). Numerical calculations of the linear response of a gaseous disk to a protoplanet. *Icarus*, 102, 150–165.

Krijt, S., Ormel, C. W., Dominik, C., & Tielens, A. G. G. M. (2015). Erosion and the limits to planetesimal growth. *A&A*, 574, A83.

Kuiper, G. P. (1951). On the Origin of the Solar System. *Proceedings of the National Academy of Science*, 37, 1–14.

Kuiper, R., Klahr, H., Beuther, H., & Henning, T. (2010a). Circumventing the Radiation Pressure Barrier in the Formation of Massive Stars via Disk Accretion. *ApJ*, 722, 1556–1576.

Kuiper, R., Klahr, H., Beuther, H., & Henning, T. (2011). Three-dimensional Simulation of Massive Star Formation in the Disk Accretion Scenario. *ApJ*, 732, 20.

Kuiper, R., Klahr, H., Dullemond, C., Kley, W., & Henning, T. (2010b). Fast and accurate frequency-dependent radiation transport for hydrodynamics simulations in massive star formation. *A&A*, 511, A81.

Kuiper, R. & Yorke, H. W. (2013). On the Effects of Optically Thick Gas (Disks) around Massive Stars. *ApJ*, 763, 104.

Kurucz, R. (1993a). Atomic data for opacity calculations. *Kurucz CD-ROM No. 1. Cambridge, Mass.: Smithsonian Astrophysical Observatory, 1993.*, 1.

Kurucz, R. (1993b). Diatomic Molecular Data for Opacity Calculations. *Kurucz CD-ROM No. 15. Cambridge, Mass.: Smithsonian Astrophysical Observatory, 1993.*, 15.

Kurucz, R. L. (1970). Atlas: a Computer Program for Calculating Model Stellar Atmospheres. *SAO Special Report*, 309.

Kurucz, R. L. (1979). Model atmospheres for G, F, A, B, and O stars. *ApJS*, 40, 1–340.

Kurucz, R. L. (2002). Atomic and Molecular Data Needs for Astrophysics. In D. R. Schultz, P. S. Krstic, & F. Ownby (Eds.), *Atomic and Molecular Data and Their Applications*, volume 636 of *American Institute of Physics Conference Series* (pp. 134–143).

Kurucz, R. L. & Avrett, E. H. (1981). Solar Spectrum Synthesis. I. A Sample Atlas from 224 to 300 nm. *SAO Special Report*, 391.

Kurucz, R. L., Peytremann, E., & Avrett, E. H. (1974). *Blanketed model atmospheres for early-type stars*.

Labs, D. (1951). Die Temperaturschichtung der Sonnenatmosphäre im Strahlungsgleichgewicht unter Berücksichtigung der Fraunhoferlinien. Mit 6 Textabbildungen. *ZAp*, 29, 199.

Lagrange, A.-M., Langlois, M., Gratton, R., Maire, A.-L., Milli, J., Olofsson, J., Vigan, A., Bailey, V., Mesa, D., Chauvin, G., Boccaletti, A., Galicher, R., Girard, J. M., Bonnefoy, M., Samland, M., Menard, F., Henning, T., Kenworthy, M., Thalmann, C., Beust, H., Beuzit, J.-L., Brandner, W., Buenzli, E., Cheetham, A., Janson, M., le Coroller, H., Lannier, J., Mouillet, D., Peretti, S., Perrot, C., Salter, G., Sissa, E., Wahhaj, Z., Abe, L., Desidera, S., Feldt, M., Madec, F., Perret, D., Petit, C., Rabou, P., Soenke, C., & Weber, L. (2015). A narrow, edge-on disk resolved around HD 106906 with SPHERE. *ArXiv e-prints*.

Larson, R. B. (1969). Numerical calculations of the dynamics of collapsing proto-star. *MNRAS*, 145, 271.

Larson, R. B. (1984). Gravitational torques and star formation. *MNRAS*, 206, 197–207.

Laughlin, G. & Bodenheimer, P. (1994). Nonaxisymmetric evolution in protostellar disks. *ApJ*, 436, 335–354.

Lesur, G. & Papaloizou, J. C. B. (2010). The subcritical baroclinic instability in local accretion disc models. *A&A*, 513, A60.

Levermore, C. D. & Pomraning, G. C. (1981). A flux-limited diffusion theory. *ApJ*, 248, 321–334.

Lin, D. N. C. & Pringle, J. E. (1987). A viscosity prescription for a self-gravitating accretion disc. *MNRAS*, 225, 607–613.

Lin, M.-K. & Youdin, A. (2015). Cooling Requirements for the Vertical Shear Instability in Protoplanetary Disks. *ArXiv e-prints*.

Lin, S.-Y., Ohashi, N., Lim, J., Ho, P. T. P., Fukagawa, M., & Tamura, M. (2006). Possible Molecular Spiral Arms in the Protoplanetary Disk of AB Aurigae. *ApJ*, 645, 1297–1304.

Lindberg, J. E., Jørgensen, J. K., Brinch, C., Haugbølle, T., Bergin, E. A., Harsono, D., Persson, M. V., Visser, R., & Yamamoto, S. (2014). ALMA observations of the kinematics and chemistry of disc formation. *A&A*, 566, A74.

Lissauer, J. J. (1993). Planet formation. *ARA&A*, 31, 129–174.

Lobo Gomes, A. & Klahr, H. (2013). Vortices being killed by planets in thermal relaxed disks. In *Protostars and Planets VI Posters* (pp.34).

Lobo Gomes, A., Klahr, H., Uribe, A. L., Pinilla, P., & Surville, C. (2015). Vortex Formation and Evolution in Planet Harboring Disks under Thermal Relaxation. *ArXiv e-prints*.

Lockyer, J. N. (1869). Spectroscopic Observations of the Sun. No. II. *Philosophical Transactions of the Royal Society of London Series I*, 159, 425–444.

Lodato, G. & Bertin, G. (2003). Non-Keplerian rotation in the nucleus of <ASTROBJ>NGC 1068</ASTROBJ>: Evidence for a massive accretion disk? *A&A*, 398, 517–524.

Lodato, G. & Rice, W. K. M. (2004). Testing the locality of transport in self-gravitating accretion discs. *MNRAS*, 351, 630–642.

Lodato, G. & Rice, W. K. M. (2005). Testing the locality of transport in self-gravitating accretion discs - II. The massive disc case. *MNRAS*, 358, 1489–1500.

Luhman, K. L., Adame, L., D'Alessio, P., Calvet, N., Hartmann, L., Megeath, S. T., & Fazio, G. G. (2005). Discovery of a Planetary-Mass Brown Dwarf with a Circumstellar Disk. *ApJ*, 635, L93–L96.

Lynden-Bell, D. & Kalnajs, A. J. (1972). On the generating mechanism of spiral structure. *MNRAS*, 157, 1.

Lyra, W. (2014). Convective Overstability in Accretion Disks: Three-dimensional Linear Analysis and Nonlinear Saturation. *ApJ*, 789, 77.

Lyra, W., Johansen, A., Klahr, H., & Piskunov, N. (2008). Embryos grown in the dead zone. Assembling the first protoplanetary cores in low mass self-gravitating circumstellar disks of gas and solids. *A&A*, 491, L41–L44.

Lyra, W., Johansen, A., Zsom, A., Klahr, H., & Piskunov, N. (2009). Planet formation bursts at the borders of the dead zone in 2D numerical simulations of circumstellar disks. *A&A*, 497, 869–888.

Lyra, W. & Klahr, H. (2011). The baroclinic instability in the context of layered accretion. Self-sustained vortices and their magnetic stability in local compressible unstratified models of protoplanetary disks. *A&A*, 527, A138.

Lyra, W., Paardekooper, S.-J., & Mac Low, M.-M. (2010). Orbital Migration of Low-mass Planets in Evolutionary Radiative Models: Avoiding Catastrophic Infall. *ApJ*, 715, L68–L73.

Malygin, M. G., Kuiper, R., Klahr, H., Dullemond, C. P., & Henning, T. (2014). Mean gas opacity for circumstellar environments and equilibrium temperature degeneracy. *A&A*, 568, A91.

Malygin, M. G., Pavlenko, Y. V., Jenkins, J. S., Jones, H. R. A., Ivanyuk, O. M., & Pinfield, D. J. (2012). Determination of atomic abundances of solar-type stars. *Advances in Astronomy and Space Physics*, 2, 20–22.

Marcus, P. S., Pei, S., Jiang, C.-H., Barranco, J. A., Hassanzadeh, P., & Lecoanet, D. (2015). Zombie Vortex Instability. I. A Purely Hydrodynamic Instability to Resurrect the Dead Zones of Protoplanetary Disks. *ApJ*, 808, 87.

Marcus, P. S., Pei, S., Jiang, C.-H., & Hassanzadeh, P. (2013). Three-Dimensional Vortices Generated by Self-Replication in Stably Stratified Rotating Shear Flows. *Physical Review Letters*, 111(8), 084501.

Marcy, G. W. & Butler, R. P. (1996). A Planetary Companion to 70 Virginis. *ApJ*, 464, L147.

Marois, C., Macintosh, B., Barman, T., Zuckerman, B., Song, I., Patience, J., Lafrenière, D., & Doyon, R. (2008). Direct Imaging of Multiple Planets Orbiting the Star HR 8799. *Science*, 322, 1348–.

Mathis, J. S., Rumpl, W., & Nordsieck, K. H. (1977). The size distribution of interstellar grains. *ApJ*, 217, 425–433.

Mayer, L., Quinn, T., Wadsley, J., & Stadel, J. (2002). Formation of Giant Planets by Fragmentation of Protoplanetary Disks. *Science*, 298, 1756–1759.

Mayer, L., Quinn, T., Wadsley, J., & Stadel, J. (2004). The Evolution of Gravitationally Unstable Protoplanetary Disks: Fragmentation and Possible Giant Planet Formation. *ApJ*, 609, 1045–1064.

Mayor, M. & Queloz, D. (1995). A Jupiter-mass companion to a solar-type star. *Nature*, 378, 355–359.

McNally, C. P. & Pessah, M. E. (2014). On Vertically Global, Horizontally Local Models for Astrophysical Disks. *ArXiv e-prints*.

Mejía, A. C., Durisen, R. H., & Pickett, B. K. (2003). Gravitational Instabilities in Disks with Radiative Cooling. In D. Deming & S. Seager (Eds.), *Scientific Frontiers in Research on Extrasolar Planets*, volume 294 of *Astronomical Society of the Pacific Conference Series* (pp. 287–290).

Mejía, A. C., Durisen, R. H., Pickett, M. K., & Cai, K. (2005). The Thermal Regulation of Gravitational Instabilities in Protoplanetary Disks. II. Extended Simulations with Varied Cooling Rates. *ApJ*, 619, 1098–1113.

Meru, F. (2015). Triggered fragmentation in self-gravitating discs: forming fragments at small radii. *MNRAS*, 454, 2529–2538.

Meru, F. & Bate, M. R. (2011a). Non-convergence of the critical cooling time-scale for fragmentation of self-gravitating discs. *MNRAS*, 411, L1–L5.

Meru, F. & Bate, M. R. (2011b). On the fragmentation criteria of self-gravitating protoplanetary discs. *MNRAS*, 410, 559–572.

Meru, F. & Bate, M. R. (2012). On the convergence of the critical cooling time-scale for the fragmentation of self-gravitating discs. *MNRAS*, 427, 2022–2046.

Meru, F., Geretshauser, R. J., Schäfer, C., Speith, R., & Kley, W. (2013). Growth and fragmentation of centimetre-sized dust aggregates: the dependence on aggregate size and porosity. *MNRAS*, 435, 2371–2390.

Meyer, F. (1982). Limit cycle instabilities in accretion disks. In W. Brinkmann & J. Truemper (Eds.), *Accreting Neutron Stars* (pp. 333–337).

Milne, E. A. (1928). The total absorption in the Sun's reversing layer. *The Observatory*, 51, 88–96.

Mizuno, H. (1980). Formation of the Giant Planets. *Progress of Theoretical Physics*, 64, 544–557.

Mizuno, H., Nakazawa, K., & Hayashi, C. (1978). Instability of a gaseous envelope surrounding a planetary core and formation of giant planets. *Progress of Theoretical Physics*, 60, 699–710.

Mordasini, C., Mollière, P., Dittkrist, K.-M., Jin, S., & Alibert, Y. (2015). Global models of planet formation and evolution. *International Journal of Astrobiology*, 14, 201–232.

Muzerolle, J., D'Alessio, P., Calvet, N., & Hartmann, L. (2004). Magnetospheres and Disk Accretion in Herbig Ae/Be Stars. *ApJ*, 617, 406–417.

Nakamoto, T. & Nakagawa, Y. (1994). Formation, early evolution, and gravitational stability of protoplanetary disks. *ApJ*, 421, 640–650.

Nakano, T. (1989). Conditions for the formation of massive stars through nonspherical accretion. *ApJ*, 345, 464–471.

Nelson, A. F., Benz, W., & Ruzmaikina, T. V. (2000). Dynamics of Circumstellar Disks. II. Heating and Cooling. *ApJ*, 529, 357–390.

Nelson, R. P., Gressel, O., & Umurhan, O. M. (2013). Linear and non-linear evolution of the vertical shear instability in accretion discs. *MNRAS*, 435, 2610–2632.

Nelson, R. P. & Papaloizou, J. C. B. (2004). The interaction of giant planets with a disc with MHD turbulence - IV. Migration rates of embedded protoplanets. *MNRAS*, 350, 849–864.

Nero, D. & Bjorkman, J. E. (2009). Did Fomalhaut, HR 8799, and HL Tauri Form Planets Via the Gravitational Instability? Placing Limits on the Required Disk Masses. *ApJ*, 702, L163–L167.

Nero, D. J. (2010). *Radiative cooling in disks and its effects on the formation of giant planets via the gravitational instability*. PhD thesis, The University of Toledo.

Olofsson, H., Bergman, P., Lucas, R., Eriksson, K., Gustafsson, B., & Bieging, J. H. (2000). A high-resolution study of episodic mass loss from the carbon star TT Cygni. *A&A*, 353, 583–597.

Paardekooper, S.-J. (2012). Numerical convergence in self-gravitating shearing sheet simulations and the stochastic nature of disc fragmentation. *MNRAS*, 421, 3286–3299.

Paardekooper, S.-J., Baruteau, C., & Meru, F. (2011). Numerical convergence in self-gravitating disc simulations: initial conditions and edge effects. *MNRAS*, 416, L65–L69.

Paardekooper, S.-J. & Mellema, G. (2006). Halting type I planet migration in non-isothermal disks. *A&A*, 459, L17–L20.

Paczynski, B. (1978). A model of selfgravitating accretion disk. *Acta Astron.*, 28, 91–109.

Papaloizou, J. C. & Savonije, G. J. (1991). Instabilities in self-gravitating gaseous discs. *MNRAS*, 248, 353–369.

Papaloizou, J. C. B. & Terquem, C. (2006). Planet formation and migration. *Reports on Progress in Physics*, 69, 119–180.

Pavlenko, Y. B. (1991a). The statistical equilibrium and the 670, 776 and 670, 791 NM absorption lines of Li I in the spectra of red-giant - Results. *AZh*, 68, 1240–1246.

Pavlenko, Y. V. (1991b). Determination of C N and O Abundances in the Atmospheres of Late Type Stars - Extreme Value Problem. *Soviet Ast.*, 35, 212.

Pavlenko, Y. V. (1991c). Statistical Equilibrium and the Lii 670.766-NM and 670.791-NM Absorption Lines in the Spectrum of Red Giants - Results. *Soviet Ast.*, 35, 623.

Pavlenko, Y. V. (1991d). The determination of C, N, and O abundances in late-type star atmospheres - Extremum problem. *AZh*, 68, 431–434.

Pavlenko, Y. V. (1997a). A lithium test and modeling of lithium lines in late-type M dwarfs - Teide1. *AZh*, 74, 608.

Pavlenko, Y. V. (1997b). Depletion of TiO and spectra of the coolest brown dwarfs. *Odessa Astronomical Publications*, 10, 76.

Pavlenko, Y. V. (2003). Model Atmospheres of Red Giants. *A Rep.*, 47, 59–67.

Pavlenko, Y. V. & Yakovina, L. A. (2010). Model atmospheres of carbon giants with high carbon abundance. *Kinematics and Physics of Celestial Bodies*, 25, 302–308.

Pelupessy, F. I. & Papadopoulos, P. P. (2009). Molecular Gas, CO, and Star Formation in Galaxies: Emergent Empirical Relations, Feedback, and the Evolution of Very Gas-Rich Systems. *ApJ*, 707, 954–970.

Perets, H. B. & Kenyon, S. J. (2013). Wind-accretion Disks in Wide Binaries, Second-generation Protoplanetary Disks, and Accretion onto White Dwarfs. *ApJ*, 764, 169.

Pérez, L. M., Isella, A., Carpenter, J. M., & Chandler, C. J. (2014). Large-scale Asymmetries in the Transitional Disks of SAO 206462 and SR 21. *ApJ*, 783, L13.

Perri, F. & Cameron, A. G. W. (1974). Hydrodynamic instability of the solar nebula in the presence of a planetary core. *Icarus*, 22, 416–425.

Petersen, M. R., Julien, K., & Stewart, G. R. (2007). Baroclinic Vorticity Production in Protoplanetary Disks. I. Vortex Formation. *ApJ*, 658, 1236–1251.

Peytremann, E. (1972). Theoretical Effect of Various Broadening Parameters on Ultraviolet Line Profiles. *A&A*, 17, 76.

Peytremann, E. (1974a). Line-blanketing and Model Stellar Atmospheres. I. Statistical Method and Calculation of a Grid of Models. *A&A*, 33, 203.

Peytremann, E. (1974b). Line blanketing and model stellar atmospheres III. Tables of models and broad-band colours. *A&AS*, 18, 81.

Peytremann, E. (1975). Line blanketing and model stellar atmospheres. II - Interpretation of broad-band photometric observations. *A&A*, 38, 417–434.

Pickering, E. C. (1901a). On the Spectroscopic Binary $\iota$ Pegasi. *Astronomische Nachrichten*, 155, 247.

Pickering, E. C. (1901b). Spectrum of Lightning. *ApJ*, 14, 367.

Pickering, E. C. (1901c). Spectrum of Nova Persei no. 2. *ApJ*, 14, 79–82.

Pickering, E. C. (1901d). The Spectrum of $\eta$ Carinae. *Harvard College Observatory Circular*, 59, 4–4.

Pickering, E. C., Cannon, A. J., Cushman, F., & King, E. S. (1901). The spectrum of zeta Puppis. *ApJ*, 13, 230–232.

Pickett, B. K., Cassen, P., Durisen, R. H., & Link, R. (1998). The Effects of Thermal Energetics on Three-dimensional Hydrodynamic Instabilities in Massive Protostellar Disks. *ApJ*, 504, 468–491.

Pickett, B. K., Cassen, P., Durisen, R. H., & Link, R. (2000). The Effects of Thermal Energetics on Three-dimensional Hydrodynamic Instabilities in Massive Protostellar Disks. II. High-Resolution and Adiabatic Evolutions. *ApJ*, 529, 1034–1053.

Pickett, B. K., Durisen, R. H., & Davis, G. A. (1996). The Dynamic Stability of Rotating Protostars and Protostellar Disks. I. The Effects of the Angular Momentum Distribution. *ApJ*, 458, 714.

Pickett, B. K., Mejía, A. C., Durisen, R. H., Cassen, P. M., Berry, D. K., & Link, R. P. (2003). The Thermal Regulation of Gravitational Instabilities in Protoplanetary Disks. *ApJ*, 590, 1060–1080.

Pickett, M. K. & Lim, A. J. (2004). Planet formation: The race is not to the swift. *Astronomy and Geophysics*, 45(1), 12–1.

Pohl, A., Pinilla, P., Benisty, M., Ataiee, S., Juhász, A., Dullemond, C. P., Van Boekel, R., & Henning, T. (2015). Scattered light images of spiral arms in marginally gravitationally unstable discs with an embedded planet. *MNRAS*, 453, 1768–1778.

Pollack, J. B., Hollenbach, D., Beckwith, S., Simonelli, D. P., Roush, T., & Fong, W. (1994). Composition and radiative properties of grains in molecular clouds and accretion disks. *ApJ*, 421, 615–639.

Pollack, J. B., Hubickyj, O., Bodenheimer, P., Lissauer, J. J., Podolak, M., & Greenzweig, Y. (1996). Formation of the Giant Planets by Concurrent Accretion of Solids and Gas. *Icarus*, 124, 62–85.

Pollack, J. B., McKay, C. P., & Christofferson, B. M. (1985). A calculation of the Rosseland mean opacity of dust grains in primordial solar system nebulae. *Icarus*, 64, 471–492.

Pringle, J. E. (1981). Accretion discs in astrophysics. *ARA&A*, 19, 137–162.

Querci, F., Querci, M., & Tsuji, T. (1974). Model Atmospheres for C Type Stars. *A&A*, 31, 265.

Raettig, N., Klahr, H., & Lyra, W. (2015). Particle Trapping and Streaming Instability in Vortices in Protoplanetary Disks. *ApJ*, 804, 35.

Raettig, N., Lyra, W., & Klahr, H. (2013). A Parameter Study for Baroclinic Vortex Amplification. *ApJ*, 765, 115.

Rafikov, R. R. (2005). Can Giant Planets Form by Direct Gravitational Instability? *ApJ*, 621, L69–L72.

Rafikov, R. R. (2009). Properties of Gravitoturbulent Accretion Disks. *ApJ*, 704, 281–291.

Rafikov, R. R. (2015). Viscosity Prescription for Gravitationally Unstable Accretion Disks. *ApJ*, 804, 62.

Rameau, J., Chauvin, G., Lagrange, A.-M., Boccaletti, A., Quanz, S. P., Bonnefoy, M., Girard, J. H., Delorme, P., Desidera, S., Klahr, H., Mordasini, C., Dumas, C., & Bonavita, M. (2013). Discovery of a Probable 4-5 Jupiter-mass Exoplanet to HD 95086 by Direct Imaging. *ApJ*, 772, L15.

Raymond, S. N., Kokubo, E., Morbidelli, A., Morishima, R., & Walsh, K. J. (2014). Terrestrial Planet Formation at Home and Abroad. *Protostars and Planets VI*, (pp. 595–618).

Rice, W. K. M., Armitage, P. J., Bate, M. R., & Bonnell, I. A. (2003). The effect of cooling on the global stability of self-gravitating protoplanetary discs. *MNRAS*, 339, 1025–1030.

Rice, W. K. M., Lodato, G., & Armitage, P. J. (2005). Investigating fragmentation conditions in self-gravitating accretion discs. *MNRAS*, 364, L56–L60.

Rice, W. K. M., Lodato, G., Pringle, J. E., Armitage, P. J., & Bonnell, I. A. (2004). Accelerated planetesimal growth in self-gravitating protoplanetary discs. *MNRAS*, 355, 543–552.

Rohrmann, R. D., Althaus, L. G., García-Berro, E., Córsico, A. H., & Miller Bertolami, M. M. (2012). Outer boundary conditions for evolving cool white dwarfs. *A&A*, 546, A119.

Ruden, S. P. & Pollack, J. B. (1991). The dynamical evolution of the protosolar nebula. *ApJ*, 375, 740–760.

Safronov, V. S. (1969). *Evoliutsiia doplanetnogo oblaka.*

Sallum, S., Follette, K. B., Eisner, J. A., Close, L. M., Hinz, P., Kratter, K., Males, J., Skemer, A., Macintosh, B., Tuthill, P., Bailey, V., Defrère, D., Morzinski, K., Rodigas, T., Spalding, E., Vaz, A., & Weinberger, A. J. (2015). Accreting protoplanets in the LkCa 15 transition disk. *Nature*, 527, 342–344.

Schirrmacher, V., Woitke, P., & Sedlmayr, E. (2003). On the gas temperature in the shocked circumstellar envelopes of pulsating stars. III. Dynamical models for AGB star winds including time-dependent dust formation and non-LTE cooling. *A&A*, 404, 267–282.

Schmidt, M. (1963). 3C 273 : A Star-Like Object with Large Red-Shift. *Nature*, 197, 1040.

Seaton, M. J., Yan, Y., Mihalas, D., & Pradhan, A. K. (1994). Opacities for Stellar Envelopes. *MNRAS*, 266, 805.

Seizinger, A. & Kley, W. (2013). Bouncing behavior of microscopic dust aggregates. *A&A*, 551, A65.

Semenov, D., Henning, T., Helling, C., Ilgner, M., & Sedlmayr, E. (2003). Rosseland and Planck mean opacities for protoplanetary discs. *A&A*, 410, 611–621.

Shakura, N. I. & Sunyaev, R. A. (1973). Black holes in binary systems. Observational appearance. *A&A*, 24, 337–355.

Shapiro, S. L. & Teukolsky, S. A. (1983). *Black holes, white dwarfs, and neutron stars: The physics of compact objects*.

Simon, M., Dutrey, A., & Guilloteau, S. (2000). Dynamical Masses of T Tauri Stars and Calibration of Pre-Main-Sequence Evolution. *ApJ*, 545, 1034–1043.

Sneden, C., Johnson, H. R., & Krupp, B. M. (1976). A statistical method for treating molecular line opacities. *ApJ*, 204, 281–289.

Stamatellos, D. & Whitworth, A. P. (2008). Can giant planets form by gravitational fragmentation of discs?. *A&A*, 480, 879–887.

Stoll, M. H. R. & Kley, W. (2014). Vertical shear instability in accretion disc models with radiation transport. *A&A*, 572, A77.

Strom, S. E. & Kurucz, R. (1966). Statistical Procedure for Computing Line-Blanketed Model Stellar Atmospheres. *AJ*, 71, 181.

Tanaka, K. E. I. & Nakamoto, T. (2011). Direct Stellar Radiation Pressure at the Dust Sublimation Front in Massive Star Formation: Effects of a Dust-free Disk. *ApJ*, 739, L50.

Tobin, J. J., Hartmann, L., Bergin, E., Chiang, H.-F., Looney, L. W., Chandler, C. J., Maret, S., & Heitsch, F. (2012). Complex Structure in Class 0 Protostellar Envelopes. III. Velocity Gradients in Non-axisymmetric Envelopes, Infall, or Rotation? *ApJ*, 748, 16.

Tobin, J. J., Hartmann, L., Chiang, H.-F., Looney, L. W., Bergin, E. A., Chandler, C. J., Masqué, J. M., Maret, S., & Heitsch, F. (2011). Complex Structure in Class 0 Protostellar Envelopes. II. Kinematic Structure from Single-dish and Interferometric Molecular Line Mapping. *ApJ*, 740, 45.

Tohline, J. E., Durisen, R. H., & McCollough, M. (1985). The linear and nonlinear dynamic stability of rotating N = 3/2 polytropes. *ApJ*, 298, 220–234.

Tomley, L., Cassen, P., & Steiman-Cameron, T. (1991). On the evolution of gravitationally unstable protostellar disks. *ApJ*, 382, 530–543.

Tomley, L., Steiman-Cameron, T. Y., & Cassen, P. (1994). Further studies of gravitationally unstable protostellar disks. *ApJ*, 422, 850–861.

Toomre, A. (1964). On the gravitational stability of a disk of stars. *ApJ*, 139, 1217–1238.

Turner, N. J., Fromang, S., Gammie, C., Klahr, H., Lesur, G., Wardle, M., & Bai, X.-N. (2014). Transport and Accretion in Planet-Forming Disks. *Protostars and Planets VI*, (pp. 411–432).

Turner, N. J., Sano, T., & Dziourkevitch, N. (2007). Turbulent Mixing and the Dead Zone in Protostellar Disks. *ApJ*, 659, 729–737.

Urey, H. C. (1966). Chemical evidence relative to the origin of the solar system. *MNRAS*, 131, 199.

Urpin, V. (2003). A comparison study of the vertical and magnetic shear instabilities in accretion discs. *A&A*, 404, 397–403.

Urpin, V. & Brandenburg, A. (1998). Magnetic and vertical shear instabilities in accretion discs. *MNRAS*, 294, 399.

Vaidya, B., Fendt, C., & Beuther, H. (2009). Accretion Disks Around Massive Stars: Hydrodynamic Structure, Stability, and Dust Sublimation. *ApJ*, 702, 567–579.

van der Marel, N., van Dishoeck, E. F., Bruderer, S., Birnstiel, T., Pinilla, P., Dullemond, C. P., van Kempen, T. A., Schmalzl, M., Brown, J. M., Herczeg, G. J., Mathews, G. S., & Geers, V. (2013). A Major Asymmetric Dust Trap in a Transition Disk. *Science*, 340, 1199–1202.

van Paradijs, J. & Vardya, M. S. (1975). Line Blanketing and Opacity Probability Distribution Function. *Ap&SS*, 33, L9.

Vidler, M. & Tennyson, J. (2000). Accurate partition function and thermodynamic data for water. *J. Chem. Phys.*, 113, 9766–9771.

Wada, K., Tanaka, H., Suyama, T., Kimura, H., & Yamamoto, T. (2008). Numerical Simulation of Dust Aggregate Collisions. II. Compression and Disruption of Three-Dimensional Aggregates in Head-on Collisions. *ApJ*, 677, 1296–1308.

Wada, K., Tanaka, H., Suyama, T., Kimura, H., & Yamamoto, T. (2009). Collisional Growth Conditions for Dust Aggregates. *ApJ*, 702, 1490–1501.

Watanabe, S.-I., Nakagawa, Y., & Nakazawa, K. (1990). Cooling and quasi-static contraction of the primitive solar nebula after gas accretion. *ApJ*, 358, 282–292.

Weidenschilling, S. J. (1977). Aerodynamics of solid bodies in the solar nebula. *MNRAS*, 180, 57–70.

Weymann, R. (1960). Heating of Stellar Chromospheres by Shock Waves. *ApJ*, 132, 452.

Williams, R. E. (1967). The Ionization and Thermal Equilibrium of a Gas Excited by Ultraviolet Synchrotron Radiation. *ApJ*, 147, 556.

Wollaston, W. H. (1802). A method of examining refractive and dispersive powers, by prismatic reflection. *Philosophical Transactions of Royal Society of London*, 92, 365–380.

Wurm, G., Paraskov, G., & Krauss, O. (2005). Growth of planetesimals by impacts at 25 m/s. *Icarus*, 178, 253–263.

Yorke, H. W. & Sonnhalter, C. (2002). On the Formation of Massive Stars. *ApJ*, 569, 846–862.

Youdin, A. N. & Goodman, J. (2005). Streaming Instabilities in Protoplanetary Disks. *ApJ*, 620, 459–469.

Zhang, Y. & Tan, J. C. (2011). Radiation Transfer of Models of Massive Star Formation. I. Dependence on Basic Core Properties. *ApJ*, 733, 55.

Zsom, A., Ormel, C. W., Güttler, C., Blum, J., & Dullemond, C. P. (2010). The outcome of protoplanetary dust growth: pebbles, boulders, or planetesimals? II. Introducing the bouncing barrier. *A&A*, 513, A57.

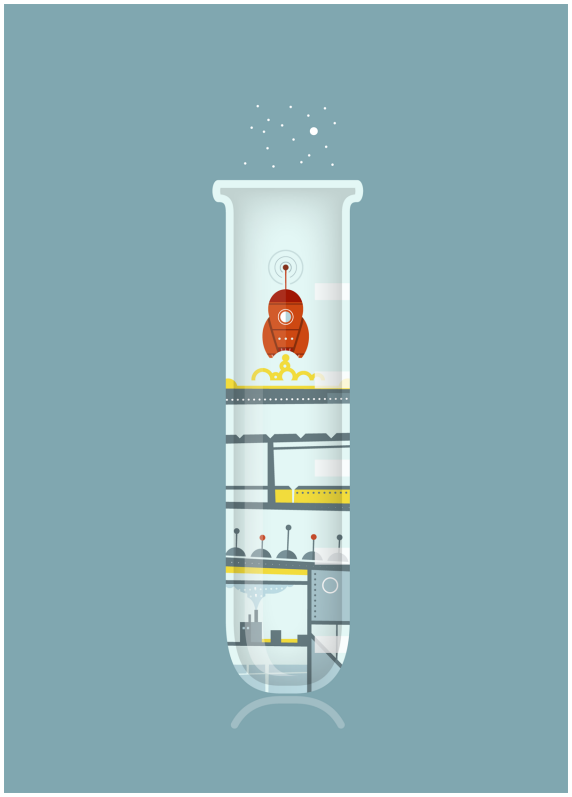

This thesis was typeset using LaTeX, originally developed by Leslie Lamport and based on Donald Knuth's TeX. The body text is set in 12 point Egenolff-Berner Garamond, a revival of Claude Garamont's humanist typeface. The above illustration, "Science Experiment 02", was created by Ben Schlitter and released under CC BY-NC-ND 3.0. A template that can be used to format a PhD thesis with this look and feel has been released under the permissive MIT (XII) license, and can be found online at github.com/suchow/Dissertate or from its author, Jordan Suchow, at suchow@post.harvard.edu.